Technical University of Denmark

DTU

Possible magnetism in vortex cores of superconducting TmNi2B2C studied by small angle neutron scattering

Abrahamsen, Asger Bech

Publication date:
2003

Document Version
Publisher's PDF, also known as Version of record

Link back to DTU Orbit

DTU Library
Technical Information Center of Denmark

Possible magnetism in vortex cores of superconducting $TmNi_2B_2C$ studied by small angle neutron scattering

Asger Bech Abrahamsen

Abstract   The borocarbide intermetallics RNi_2B_2C (R = Y, Ce-Lu) were discovered in 1994 and attracted a large attention because superconductivity and magnetic ordering are coexisting in R = Dy, Ho, Er and Tm. Early reports concluded that these compounds should be considered as anisotropic BCS superconductors with a phonon-mediated moderately strong coupling between the conduction electrons causing the creation of Cooper pairs. The magnetism is of the indirect Ruderman-Kittel-Kasuya-Yosida(RKKY) type where the conduction electrons are polarized by the local magnetic moment of the rare-earth ions and thereby mediates a coupling between the ions, which orders into a spin density wave at sufficiently low temperatures. Thus an intricate interplay between the magnetism and the superconducting state is expected and has indeed been observed.

The compound $TmNi_2B_2C$ has previously been studied by Small Angle Neutron Scattering(SANS) with the applied field along the crystalline *c*-axis and a very rich phase diagram in terms of flux line lattices(FLL) with different symmetries have been found. One of the FLL transitions is coincident with a magnetic phase transition between two spin density waves.

In this thesis additional SANS studies of the FLL phases in $TmNi_2B_2C$ are reported and an interpretation of the phase diagram in the paramagnetic region is presented. It is suggested that the observed square FLL is stable in between two transition lines determined by two different length scales. The lower transition field is reached when the distance between the flux lines becomes comparable to the non-locality radius resulting from non-local electrodynamics, whereas the upper transition field is determined from the crossover from intermediate to high flux line density where the vortex cores start to overlap and the superconducting order parameter is suppressed in between the flux lines.

A detailed examination of the intensity of the neutron diffraction spots caused by scattering on the flux line lattice in $TmNi_2B_2C$ is presented and analyzed on the basis of the form factor of an isolated flux line. This analysis can not provide a good explanation for the observed scattering and it is suggested that the scattering from the Tm ions must be considered. One can argue that the moments of the Tm ions are modulated by the flux line lattice, because the RKKY interaction between the Tm ions might be different inside the vortex cores than outside in the superconducting phase. A calculation of the neutron scattering cross section of such a magnetic flux line lattice has been performed and compared to the SANS data. This offers a qualitative explanation of some of the observations, but future work is needed to make a more quantitative comparison.

Resumé De intermetalliske borcarbider RNi_2B_2C (R = Y, Ce-Lu) blev opdaget i 1994 og tiltrak stor opmærksomhed, fordi superledning og magnetisk orden eksisterer samtidigt i R = Dy, Ho, Er og Tm. Det blev fra tidlige studier konkluderet, at disse forbindelser skulle opfattes som anisotrope BCS superledere med en fonon medieret moderat stærk kopling mellem ledningsbånd elektronerne, som giver anledning til dannelsen af Cooper par. Magnetismen er af den indirekte Ruderman-Kittel-Kasuya-Yosida(RKKY) type, hvor ledningsbånds elektronerne bliver polariseret af det lokale magnetiske moment af de sjældne jordarts ioner og dermed medierer en kopling mellem de lokale momenter, som ordner i en spintæthedsbølge ved tilstrækkeligt lave temperaturer. Det vil sige, at en kompliceret vekselvirkning mellem superledning og magnetism forventes og er i højeste grad også observeret.

Forbindelsen $TmNi_2B_2C$ er tidligere blevet undersøgt med små vinkel neutron spredning(SANS) med det pålagte felt langs den krystallografiske c-akse og et meget rigt fasediagram af fluksliniegitre med forskellige symmetrier er blevet observeret. En af fluksliniegitter faseovergangene er sammenfaldende med en magnetisk faseovergang mellem to spintæthedsbølger.

I denne afhandling fremlægges yderligere SANS undersøgelser af fluksliniegitter faserne i $TmNi_2B_2C$ og en fortolkning af fasediagrammet i den paramagnetiske del præsenteres. Det foreslås at det observerede kvadratiske gitter er stabilt imellem to overgangslinier, som er bestemt af to forskellige længdeskalaer. Det nedre overgangsfelt opnås, når afstanden mellem fluslinierne bliver sammenlignelig med den ikke-lokale radius foresaget af ikke-lokal elektrodynamik, mens det øvre overgangsfelt er bestemt af overgangen fra middel til høj fluslinie tæthed, hvor fluslinie kernerne begynder at overlappe og den superledende ordensparameter imellem fluslinierne bliver undertrykt.

En detaljeret undersøgelse af intensiteten af neutron diffraktions pletterne foresaget af spredning på fluksliniegitteret i $TmNi_2B_2C$ bliver præsenteret og analyseret på basis af formfaktoren for en isoleret fluslinie. Denne analyse giver ikke en god forklaring på den observerede spredning og det foreslås at spredningen fra Tm ionerne skal overvejes. Man kan argumentere for at momenterne af Tm ionerne bliver moduleret at fluksliniegitteret, fordi RKKY vekselvirkningen mellem Tm ionerne måske er forskellig inde i fluslinie kernen i forhold til ude i den superledende fase. En beregning af neutron spredningstværsnittet fra et sådan magnetisk fluksliniegitter er blevet foretaget og sammenlignet med SANS dataen. Denne idé giver en kvalitativ forklaring af nogle af observationerne, men fremtidigt arbejde er nødvendigt for en mere kvantitativ sammenligning.

Contents

1 Introduction

The borocarbides RNi_2B_2C have been called the solid state physicist toy box [1], because all the rare-earth elements R = Ce-Lu can be placed in the body centered tetragonal I4/mmm crystal structure whereby magnetic ordering in the form of spin density waves, superconductivity, co-existence between the two and heavy Fermion behavior can be obtained. The system was identified in 1994 [2, 3] and offers the possibility to study the interaction between superconductivity and magnetism in a crystal structure which is simple compared to the Chevrel phases and Rare earth Rhodium Boride magnetic superconductors studied in the 70'ties [4].

Superconductivity and magnetism co-exist in the case of R = Dy, Ho, Er and Tm with critical temperatures in the range $T_c = 6 - 11\,K$ and magnetic ordering temperatures between $T_N = 10.3 - 1.5\,K$. Many methods have been used to obtain information about the two phases, but neutron scattering is superior, because the charge neutrality of the neutron makes it capable of penetrating large samples and the magnetic moment of the neutron can interact directly with the modulated magnetic field structure of either the spin density waves or the flux line lattices in the borocarbides. Triple axis neutron scattering on large single crystals has provided information about the structure of the spin density waves and the moment direction in the different borocarbides [5]. All the superconducting borocarbides are found to be Type-II and the first flux line lattice was observed in R = Er using Small Angle Neutron Scattering in 1995 [6]. A lattice of square symmetry was revealed contradicting the prediction of a hexagonal lattice in introductory textbooks on superconductivity. In the following years numerous SANS experiments were performed on both the magnetic and non-magnetic superconductors, but the flux line lattice has only been observed in the R = Er and Tm members of the magnetic superconductors despite numerous attempts on the others. A very rich phase diagram of R = Tm has been observed by M.R. Eskildsen *et. al.* [7, 8] indicating a strong interaction between superconductivity and magnetism.

This Ph.D. thesis work was initiated on February 1999 at the Condensed Matter physics department at Risø National Laboratory as a continuation of the SANS studies of M.R. Eskildsen. The working environment has however changed dramatically during the thesis, because the Danish research reactor DR3 situated at Risø was leaking heavy water in December 1999 and was permanently shut down in April 2000. Thus a reformulation of the initial project was considered, but the opportunity for a collaboration with the Paul Scherrer Institute(PSI) in Switzerland was founded and the SANS studies of the borocarbides was decided to be continued at PSI. However technical difficulties resulted in a delay of these experiments and the first was carried out in the summer 2001. Several experiments were performed, but the focus of this report is additional work on the interaction between superconductivity and magnetism in R = Tm.

The report is organized in the following sections : 1) An introduction to superconductivity in general and to the physics of flux lines in Type-II superconductors. 2) A detailed derivation of the neutron scattering cross section of a flux line lattice. The motivation for this is that textbooks on magnetic neutron scattering is chopping up the world into small dipoles, but a flux line causes a magnetic field distribution which is continuous in nature. 3) A description of a Small Angle Neutron Scattering camera. 4) A description of how the SANS diffraction pattern of a flux line lattice is analyzed. 5+6) A general outline of the properties of the Borocarbides and of the physics causing the square flux line lattice. 7) A presentation of the properties of $TmNi_2B_2C$ and additional studies and discussions of the flux line phases observed with SANS. 8) A conclusion of the work is given.

In retrospect this thesis contains a large fraction of introductory sections to different theoretical considerations about superconductivity and magnetism, and it reflects the process of putting together the puzzle of how to understand the small angle neutron scattering from the R = Tm compound. This puzzle is in no way complete and the discussion suffers from the 'experimentalists' view of the author on these aspects.

Asger Bech Abrahamsen
Materials Research Department, Risø National Laboratory
August 2002.

2 Superconductivity

Superconductivity was discovered in 1911 by Kammeling Onnes and ever since it has been a challenging field within solid state physics. For many years the phenomena was unexplained but several break troughs were achieved in the 1950's where the russian physicists Ginzburg and Landau came up with a phenomenological theory [9] and some years later Bardeen, Cooper and Schriefer(BCS) were able to formulate a microscopic theory for superconductivity in metals [10, 11]. This work removed most of the mystery of the field, but in 1986 it all came back with Bednorz and Müller's discovery of the High temperature superconductors [12], which are ceramic materials that remain superconducting at temperatures far above what is expected from the BCS theory.

A discussion of the superconducting ground state will be given here and the phenomenal Ginzburg-Landau theory is then introduced in order to discuss the properties of an object called a flux line existing in certain types of superconductors. Flux lines are tube shaped regions in which the magnetic flux in confined and quantized. They repel each other and therefore order in a lattice called the flux line lattice, which will be discussed in details in terms of structure and density.

2.1 Superconducting ground state

Superconductivity is caused by a many body interaction between the electrons in the conduction band of solids resulting in the creation of electron or hole pairs. Frölich was the first to suggest that electrons could be paired together through an indirect interaction with phonons [13]. The idea is that one conduction electron interacts with the lattice of the solid and creates an excitation in the form of a phonon. This phonon propagates through the lattice and causes a local change of the charge density which will attract another electron whereby an indirect interaction is established. Cooper later showed that one interacting electron pair at the Fermi surface would have lower energy than two non interacting electrons and the great success of the BCS theory was to prove that conduction electrons collectively coupled in Cooper pairs at the Fermi surface did have a lower energy that the non-coupled electrons. Thus the superconducting ground state of the BCS theory consist of Cooper pairs 'glued' together by the indirect phonon interaction. It should be mentioned that the two electrons in the Cooper pair are moving in opposite directions ($\mathbf{k} \uparrow, -\mathbf{k} \downarrow$) and are therefore constantly changing partners. The spins of the electrons in the Cooper pair are also opposite and the Cooper pairs therefore behave like a boson quasi-particle since $S = 0$. In this picture one can imagine the superconducting state as the condensation of Cooper pairs into a ground state, where all Cooper pairs are described by the same quantum mechanical wavefunction.

The energy of the Cooper pairs in the condensate is separated from the energies of non-paired electrons by an energy gap Δ_{BCS}, which is the energy needed to break up a Cooper pair into two electrons. From BCS calculation[1] it can be shown that at T = 0

$$\Delta_{BCS}(0) = 2\hbar\omega_D e^{-\frac{1}{N(0)V}} \tag{1}$$

where $\hbar\omega_D$ is the energy scale of phonons in solids set by the Debye frequency ω_D, N(0) is the density of states of the conduction electrons at the Fermi level and V is the BCS coupling constant describing the attraction between electrons which have energies within $\pm\hbar\omega_D$ of the Fermi level.

---

[1]Schrieffer [14] p.41

With increasing temperature the gap is closing smoothly because Cooper pairs are broken by thermal fluctuations and the presence of these excitations lower the binding energy of the Cooper pairs remaining in the condensate. Figure (1) shows the temperature dependence of the gap and how it appear in the density of state of the normal conduction electrons. The critical temperature T_c of superconductivity is defined by the temperature where the gap vanishes, which gives[2]

$$k_B T_c = 1.14 \hbar \omega_D e^{-\frac{1}{N(0)V}} \tag{2}$$

k_B is the Boltzmann constant. By comparing (1) and (2) it is seen that the gap at $T = 0$ is closely related to the critical temperature by

$$\Delta_{BCS}(0) = 1.76 k_B T_c \tag{3}$$
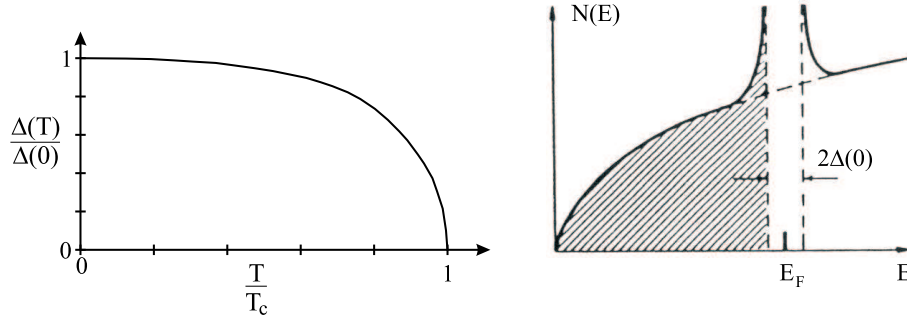
Figure 1. Left: Temperature dependence of the energy gap Δ_{BCS} for a superconductor described by the BCS theory. Right: A consequence of the gap is that the density of state of the non-paired electrons are pushed away from a region $\pm \Delta_{BCS}$ around the Fermi level and piled up just below and above the gap region.

From figure 1 it is seen that the electrons in the condensate have an energy spread of $\delta E = 2\Delta_{BCS}$ which is equivalent to a spread in the momentum of $\delta p = \frac{\delta E}{v_F}$ where v_F is the Fermi velocity. Now if the correlated electron pairs in the condensate are imagined as wave packages of a momentum spread δp then the correlation distance between the electrons can be estimated from the Heisenberg uncertainty relation $\delta x \delta p \sim \hbar$. This distance is called the BCS coherence length at T = 0

$$\xi_0 \sim \frac{\hbar v_f}{\Delta_{BCS}(0)} \tag{4}$$

Returning to the picture of the condensate as pairs of electrons moving in opposite direction it is only when the two electrons are separated by less than the coherence length that they should be considered as paired together. When the separation becomes lager they change partners in the condensate.

Two final remarks should be given about the superconducting ground state. First of all the above description is based on the BCS theory where the phonon mediated coupling is the 'glue' between the electrons in the Cooper pairs. One could however image other indirect coupling mechanisms between electrons and the puzzle of HTc superconductivity is exactly to figure out the right alternative to the phonon coupling. The ground state of the HTc materials still consist of coupled Cooper pairs and the macroscopic physics is quite similar to the conventional

---

[2]Schrieffer [14] p.55

superconductors although many characteristic properties such as T_c and ξ_0 are different.

The second remark is connected to the demand of theories capable of determining the properties of superconductors with a spatial varying gab and excitation spectrum. This can be done by reformulating the BCS theory and the main conclusion is that the condensate can be described by a macroscopic wave function with the magnitude proportional to the energy gab $|\Delta|$ and a common phase Φ for all the pairs

$$\Delta(\mathbf{r}) = |\Delta(\mathbf{r})|e^{i\Phi(\mathbf{r})} \tag{5}$$

In the following sections this wave function is used as an order parameter in the introduction of the Ginzburg-Landau theory, which can handle spatial variations of the condensate if these variation are taking place on length scales larger than the size of the Cooper pairs given by the coherence length ξ_0. The advantage of the Ginburg-landau theory is its simplicity compared to the microscopic models.

2.2   Ginzburg-Landau theory

The Ginzburg-Landau theory for superconductivity is based on the general ideas of Landau on second order phase transitions in which an order parameter grows up continuously below a transition temperature T_c [3]. This order parameter will be small close to the transition and the free energy density of the superconductor can approximately be given as an series expansion

$$F = F_n + A(T)|\Delta(\mathbf{r})|^2 + \frac{B(T)}{2}|\Delta(\mathbf{r})|^4 + ... \tag{6}$$

F_n is the free energy density of the normal phase. All terms of odd power of the order parameter are omitted since the free energy density must be invariant with respect to a phase change of the complex order parameter. Results from microscopic theory [15] gives the temperature dependence of the coefficients in the expansion near T_c

$$A(T) = N(0)\frac{T-T_c}{T_c} \quad B(T) = 0.3302\frac{N(0)}{\Delta_{BCS}(0)^2} \tag{7}$$

where $N(0)$ is the electronic density of states at the Fermi level and $\Delta_{BCS}(0)$ is the BCS gab at $T = 0$ from the previous section. By minimizing the free energy it is seen that the sign change of $A(T)$ causes an order parameter of finite size below T_c.

$$\Delta_0(T)^2 = \begin{cases} 0 & T > T_c \\ -\frac{A}{B} = 3.028\Delta_{BCS}(0)^2\frac{T_c-T}{T_c} & T < T_c \end{cases} \tag{8}$$

Thus the temperature dependence of the order parameter gab $\Delta_0(T)$ follows the BCS gab on figure 1 as $\sqrt{T_c - T}$, which is a good approximation close to T_c, but not in the T = 0 limit where $\frac{\Delta_0(0)}{\Delta_{BCS}(0)} = 1.74$.

Figure 2 illustrate the free energy density as function of the complex order parameter and the symmetry break at the phase transition is seen in the change of the position of the minimum from $|\Delta_0| = 0$ to a circle of finite value and in a negative energy

---

[3]See deGennes [15] for details

$$
\begin{aligned}
F - F_n &= -\frac{A^2}{2B} \\
&= -\frac{N(0)}{2}\frac{T_c - T}{T_c}\Delta_0(T)^2 \\
&= -\frac{3.028}{2}N(0)\Delta_{BCS}(0)^2\left(\frac{T_c - T}{T_c}\right)^2 \quad (9)
\end{aligned}
$$

This energy difference is often denoted the condensation energy of the super-conducting state. A simple hand-waving argument for the equation is that the number of electrons δN coming from the gab region is given by the product of the density of states at the fermi level $N(0)$ and the temperature dependent gab, $\delta N = N(0)\Delta_0(T)$. However only a fraction of these electrons will enter the condensate at high temperatures due to pair breaking by thermal fluctuations. If this fraction is assumed linear in temperature $f = \frac{T_c - T}{T_c}$ then the number of electrons entering the condensate is $\delta N_S = N(0)\Delta_0(T)f$. The energy of the system is lowered by $\delta E = -\Delta_0(T)$ per electron in the condensate whereby the total energy change is $\delta F = \delta N_S \delta E = -N(0)\Delta_0(T)^2 f$.
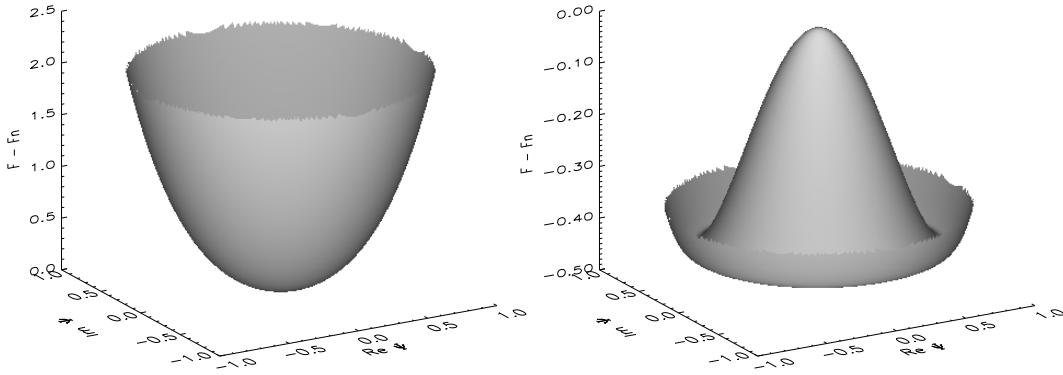
Figure 2. Ginzburg-Landau free energy surface $F - F_n = A|\Delta|^2 + \frac{B}{2}|\Delta|^4$ for a complex order parameter $\Delta = |\Delta|e^{i\Phi}$ at $T > T_c$ (left) and $T < T_c$ (right). Above T_c the order parameter at the energy minimum is zero and therefore invariant with respect to a rotation of the phase Φ, but this rotational symmetry is broken below T_c resulting in a finite size of the order parameter at $\Delta_0^2 = -\frac{A}{B}$ and a lower free energy minimum at $F - F_n = -\frac{A^2}{2B}$. The phase Φ is forced to take a specific value, which reflect that all the Cooper pairs in the condensate are described by the same wave function and thereby have the same phase. $A = \pm 1.3$ and $B = 2$ has been used to construct the figure.

The free energy given by (6) does not take into account any spatial changes in the magnitude of the order parameter, but this can be included by adding gradient terms to the free energy if the spatial changes are sufficiently slowly compared to the size of the Cooper pairs. For a cubic crystal symmetry the free energy can be written

$$
F = F_n + A|\Delta(\mathbf{r})|^2 + \frac{B}{2}|\Delta(\mathbf{r})|^4 + C\left\{\left|\frac{\partial\Delta}{\partial x}\right|^2 + \left|\frac{\partial\Delta}{\partial y}\right|^2 + \left|\frac{\partial\Delta}{\partial z}\right|^2\right\} \quad (10)
$$

where the expansion coefficient C is found from BCS calculations [15]

$$C \sim N(0)\xi_0^2 \tag{11}$$

A similarity to the momentum operator $p = -i\hbar\nabla$ is seen from the gradient term and in order to include the interaction with a magnetic field one must replace $\mathbf{p} \to \mathbf{p} - \frac{e^*}{c}\mathbf{A}$, where $e^* = 2e$ because a Cooper pair consist of two electrons [4] and $\mathbf{A}$ is the vector potential related to the magnetic field $\mathbf{h} = \nabla \times \mathbf{A}$. Thus the free energy takes the form

$$F = F_n + A|\Delta(\mathbf{r})|^2 + \frac{B}{2}|\Delta(\mathbf{r})|^4 + C \left|\left(-i\nabla - \frac{2e\mathbf{A}}{\hbar c}\right)\Delta(r)\right|^2 + \frac{h^2}{8\pi} \tag{12}$$

where the vacuum energy of the magnetic field has been included as the last term. The gradient term can now be rewritten into a form looking like the kinetic energy operator $\frac{p^2}{2m^*}$ of a particle of mass m^* by introducing a scaled order parameter

$$\psi(r) = G\Delta(r) = \frac{\sqrt{2m^*C}}{\hbar}\Delta(r) \tag{13}$$

A fundamental question in this scaling is what the particle mass m^* is and the first obvious answer is the mass of the Cooper pair, $m^* = 2m_e$, but the mass of the conduction electrons depends strongly on the electronic band structure dictated by the crystalline lattice. Thus m^* represent the effective mass of the Cooper pair and is not necessarily isotropic whereby an effective mass tensor must be introduced.

The coefficients A and B in the free energy expansion (6) must also be scaled according to (13)

$$\alpha(T) = \frac{A(T)}{G^2} \qquad \beta(T) = \frac{B(T)}{G^4} \tag{14}$$

and the free energy of the scaled order parameter becomes

$$F = F_n + \alpha|\psi|^2 + \frac{\beta}{2}|\psi|^4 + \frac{1}{2m^*}\left|\left(-i\hbar\nabla - \frac{2e\mathbf{A}}{c}\right)\psi\right|^2 + \frac{h^2}{8\pi} \tag{15}$$

which is the usual form of the Ginzburg-Landau free energy of a superconductor. The analysis of the minimum in the free energy for a homogeneous order parameter is equivalent to the previous and by using the scaling relation of (13) and (14) one gets

$$|\psi_0|^2 = -\frac{\alpha}{\beta} = G^2\Delta_0(T)^2 \tag{16}$$

$$F - F_n = -\frac{\alpha^2}{2\beta} = -\frac{A^2}{2B} \tag{17}$$

The meaning of the scaled order parameter ψ can be investigated by expressing it in microscopic variables using (13),(11), (4) and (8)

$$\begin{aligned}
|\psi_0|^2 &= \frac{2m^*C}{\hbar^2}\Delta_0(T)^2 \\
&\sim N(0)m^*v_F^2\frac{\Delta_0(T)^2}{\Delta_{BCS}(0)^2} \\
&\sim N(0)\epsilon_F\frac{T_c - T}{T_c}
\end{aligned} \tag{18}$$

[4]The sign of the electron charge is included in the definition $e^* = 2e = -2|e|$, whereby a current density in the Maxwell equations becomes $\boldsymbol{J} = ne^*\boldsymbol{v}$ with n being the particle density and $\boldsymbol{v}$ the velocity.

In the last step the Fermi energy ϵ_F of the electrons was introduced and it is now clear that the scaled order parameter is a particle density, since $N(0)\epsilon_F$ is approximately the density of all the conduction electrons in the metal. Again we find a factor of the form $f = \frac{T_c - T}{T_c}$, which could be interpreted as the fraction of the conduction electrons going into the condensate just as stated earlier and $|\psi_0|^2$ is then the density of Cooper pairs in the condensate. Ginzburg and Landau considered the scaled order parameter as a macroscopic wavefunction describing the condensate and a natural result of this picture is that the square of the wavefunction reflects the particle density n_s in the condensate, $|\psi|^2 = \frac{1}{2}n_s$. However they did not understand the microscopic origin of ψ when the theory was first formulated.

Ginzburg-Landau equations

By minimizing the free energy density integrated over the sample volume $\tilde{F} = \int_v F d\mathbf{r}$ with respect to the order parameter ψ and the vector potential $\mathbf{A}$ one obtain a set of coupled differential equations describing the equilibrium distribution of the order parameter, vector potential and flow of the condensate.

$$\alpha\psi + \beta|\psi|^2\psi + \frac{1}{2m^*}\left(-i\,\hbar\nabla - \frac{2e}{c}\mathbf{A}\right)^2\psi = 0 \tag{19}$$

$$\mathbf{j} = -\frac{ie\hbar}{m^*}(\psi^*\nabla\psi - \psi\nabla\psi^*) - \frac{4e^2}{m^*c}\psi^*\psi\mathbf{A} \tag{20}$$

The first equation describes the order parameter and the second the current due to gradients in the order parameter and to the presence of a vector potential. In addition to these equations the Maxwell equations must be fulfilled.

Penetration depth λ

There are two characteristic length scales connected to the Ginzburg-Landau(GL) equations and the first describing the response to an applied magnetic field is called the penetration depth λ. It is found in the limit where the magnitude of the order parameter $\psi = |\psi|e^{i\phi}$ is assumed constant in space whereby (20) gives

$$\mathbf{j} = \frac{1}{\Lambda^2}\left(\frac{\hbar c}{2e}\nabla\phi - \mathbf{A}\right) \tag{21}$$

with

$$\Lambda^2 = \frac{m^*c}{4e^2|\psi|^2} \tag{22}$$

Inside a superconductor the macroscopic wave function describing the condensate must be single valued and the phase gradient $\nabla\phi$ will therefore be zero. By taking the curl on both sides, applying Maxwell's equation $\frac{4\pi}{c}\mathbf{j} = \nabla \times \mathbf{h}$ and using the vector relation $\nabla \times \nabla \times \mathbf{h} = \nabla(\nabla \cdot \mathbf{h}) - \nabla^2\mathbf{h}$ a differential equation for the magnetic field $\mathbf{h}$ is obtained and this is called the London equation

$$\nabla^2\mathbf{h} - \frac{1}{\lambda^2}\mathbf{h} = 0 \tag{23}$$

A one dimensional solution to the London equation near the surface of a superconductor extending in $x > 0$ and with an applied field $h_z(0)$ along the surface is

$$\frac{\partial^2 h_z(x)}{\partial x^2} \quad - \quad \frac{1}{\lambda^2} h_z(x) = 0 \Rightarrow \tag{24}$$

$$h_z(x) \quad = \quad h_z(0) \exp\left(-\frac{x}{\lambda}\right) \tag{25}$$

which shows that the applied magnetic field is decaying exponentially inside the superconductor as shown on figure 3 and the characteristic length scale is the penetration depth λ

$$\lambda^2 = \frac{c}{4\pi}\Lambda^2 = \frac{m^* c^2}{16\pi e^2 |\psi_0|^2} \tag{26}$$

The current flow near the surface is found from the Maxwell equation

$$\mathbf{j} = \frac{c}{4\pi}\nabla \times \mathbf{h} = \frac{c}{4\pi}\begin{vmatrix} \hat{\mathbf{x}} & \hat{\mathbf{y}} & \hat{\mathbf{z}} \\ \frac{\partial}{\partial x} & \frac{\partial}{\partial y} & \frac{\partial}{\partial z} \\ 0 & 0 & h_z \end{vmatrix} = -\frac{c}{4\pi}\frac{h_z(0)}{\lambda}\exp\left(-\frac{x}{\lambda}\right)\hat{\mathbf{y}} \tag{27}$$

From the above it is seen that a superconductor screens out an applied magnetic field from the interior of the sample by creating supercurrents at the edge in a region given by the penetration depth. This effect is called the Meissner effect and the state with $\mathbf{B} \equiv 0$ caused by surface current is called the Meissner state.

Coherence length ξ

In the analysis above one can question the assumption that the order parameter $|\psi_0|^2$ is constant all the way to the surface and the second length scale of the GL equations is connected to spatial changes in the order parameter, which is expected at the surface. It is hidden in the first GL equation and is identified by introducing a reduced order parameter $\psi = \psi_0 f$, neglecting the magnetic field and using $|\psi_0|^2 = -\frac{\alpha}{\beta}$. In one dimension (19) becomes

$$\frac{\hbar^2}{2m^*|\alpha|}\frac{\partial^2 f}{\partial x^2} + f - f^3 = 0 \tag{28}$$

from which the temperature dependent coherence length $\xi(T)$ is obtained

$$\xi(T)^2 = \frac{\hbar^2}{2m^*|\alpha|} \tag{29}$$

A solution to (28) describing the order parameter close to the surface in zero magnetic field can be found by imposing the following boundary conditions to f

$$\begin{matrix} f = 0 & x = 0 \\ f \to 1 & x \to \infty \end{matrix} \tag{30}$$

By multiplying (28) with $\frac{df}{dx}$, integrating with respect to x and using the relation $\frac{d^2 f}{dx^2}\frac{df}{dx} = \frac{1}{2}\frac{d}{dx}\left(\left(\frac{df}{dx}\right)^2\right)$ the differential equation can be rewritten into

$$\xi^2(T)\left(\frac{df}{dx}\right)^2 + f^2 - \frac{1}{2}f^4 = C_{int} \tag{31}$$

The integration constant C_{int} is fixed by the boundary condition $f \to 1$ for $x \to \infty$ giving $C_{int} = \frac{1}{2}$ and

$$\xi^2(T)\left(\frac{df}{dx}\right)^2 = \frac{1}{2}\left(1-f^2\right)^2 \tag{32}$$

with the solution

$$f = \tanh\left(\frac{x}{\sqrt{2}\xi(T)}\right) \tag{33}$$

Thus the order parameter has reached 61 % of its maximum value in a distance ξ from the surface as shown on figure 3, which demonstrates that the coherence length sets the length scale for changes in the order parameter.
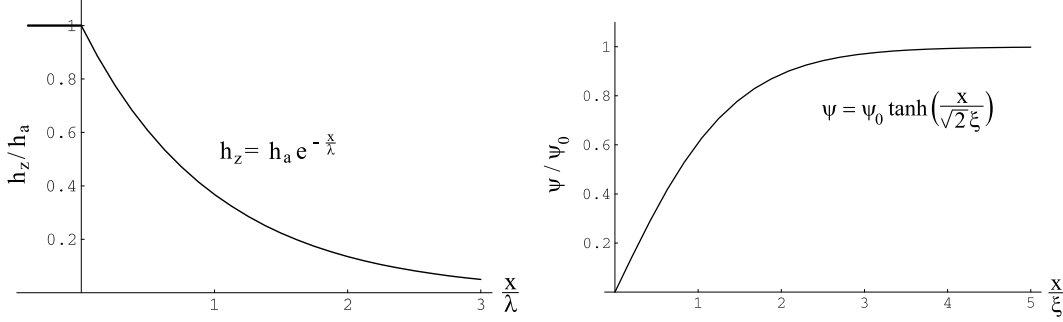
Figure 3. Left: The length scale for penetration of an applied field into a superconductor is given by the penetration depth λ and the field profile shown is obtained if the order parameter is assumed constant all the way to the surface at $x = 0$. Right : The length scale for changes in the order parameter is given by the coherence length ξ and the figure shows how the order parameter will grow up near the surface in zero applied field as found by solving the GL equations.

Relation to microscopic parameters

The relation of $\xi(T)$ to the microscopic theory is found from the scaling $\alpha(T) = \frac{A(T)}{G^2}$ given by (14) and inserted into (29)

$$\xi(T)^2 = -\frac{C}{A} \Rightarrow$$

$$\xi(T) \sim \xi_0\left(\frac{T_c}{T_c-T}\right)^{\frac{1}{2}}$$

$$\sim \frac{\hbar v_F}{\Delta_{BCS}(0)}\left(\frac{T_c}{T_c-T}\right)^{\frac{1}{2}} \tag{34}$$

Thus $\xi(T)$ is diverging at the transition temperature T_c and the condition that changes in the order parameter is taking place on length scales much larger that the size of the Cooper pairs is fulfilled when T is sufficiently close to T_c.

Also the penetration depth can be related to the microscopic theory using the scaling in (16)

$$\lambda(T)^{-2} = \frac{16\pi e^2}{m^* c^2}|\psi_0|^2$$

$$= \frac{32\pi e^2}{\hbar^2 c^2}C\Delta_0(T)^2 \Rightarrow$$

$$\lambda(T) \sim \frac{c}{e}\frac{1}{\sqrt{N(0)}v_F}\left(\frac{T_c}{T_c - T}\right)^{\frac{1}{2}} \tag{35}$$

and it is seen that it diverges in the same manner as the coherence length at T_c. Thus the ratio between the two is temperature independent and defines the Ginzburg-Landau parameter

$$\kappa = \frac{\lambda(T)}{\xi(T)} \tag{36}$$

$$\sim \frac{c}{\hbar e}\frac{\Delta_{BCS}(0)}{\sqrt{N(0)}v_F^2} \tag{37}$$

which can be considered as a material parameter characterizing superconductivity from the microscopic energy gab $\Delta_{BCS}(0)$ and the electronic properties of the host metal in terms of the density of state at the Fermi level $N(0)$ and the Fermi velocity v_F.

2.3 Type-II superconductors

Superconductors can be divided into two types depending on the Ginzburg-Landau κ characterizing superconductivity by the ration between the penetration depth and the coherence length. In the previous section the order parameter change and the field decay was treated separately, but in this section the interface between a superconducting region and a normal region caused by a magnetic field will be analyzed. It is shown that the energy associated with the interface can change from positive to negative when going from small to large κ and this sign change separates Type-I and Type-II superconductors.

A thermodynamic critical magnetic field H_C can be defined from the GL free energy density in (15) by setting $F - F_n = 0$

$$\frac{H_c^2}{8\pi} = \alpha|\psi|^2 + \frac{\beta}{2}|\psi|^4 = \frac{\alpha^2}{2\beta} \tag{38}$$

which shows that superconductivity is suppressed when the magnetic energy density is equal to the condensation energy density.

Surface energy of NS interface

An interface between a normal region and a superconducting region is illustrated on figure 4 where a magnetic field h equal to H_C has suppressed the order parameter to zero on the left hand side and gradually moving to the right it increases over the coherence length while the magnetic field is screened to zero over the penetration depth. The free energy density as formulated in (15) is not well suited for calculation where the magnetic field h is changing and the Gibbs free energy density G is a better choice
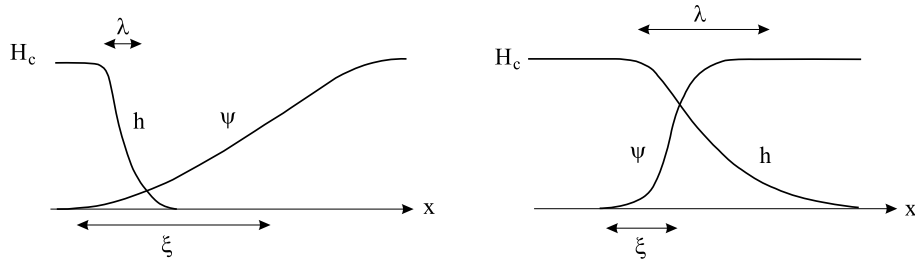
$$G = F - \frac{hH}{4\pi} \tag{39}$$

Figure 4. Interface between a normal and a superconducting region caused by an applied field equal to the thermodynamic field H_C for a superconductor with $\kappa << 1$ (left) and $\kappa >> 1$ (right).

giving

$$
\begin{aligned}
G &\to F_n + \frac{H_c^2}{8\pi} - \frac{H_c^2}{4\pi} = F_n - \frac{H_c^2}{8\pi} \qquad x \to -\infty \\
G &\to F_n + \alpha|\psi|^2 + \frac{\beta}{2}|\psi|^4 = F_n - \frac{H_c^2}{8\pi} \qquad x \to \infty
\end{aligned} \tag{40}
$$

Since the Gibbs energy density is identical in the normal and the superconducting phase one can determine the surface energy γ of the interface from the integral of the difference between G and G_n of the normal phase

$$
\begin{aligned}
\gamma &= \int_{-\infty}^{\infty} (G - G_n) dx \\
&= \int_{-\infty}^{\infty} \left(\alpha|\psi|^2 + \frac{\beta}{2}|\psi|^4 + \frac{1}{2m^*} \left| \left(-i\hbar\nabla - \frac{2e\mathbf{A}}{c} \right) \psi \right|^2 + \frac{(h - H_c)^2}{8\pi} \right) dx
\end{aligned} \tag{41}
$$

By multiplying equation (19) with ψ^* and integrating by parts it can be shown [5] that

$$
\int_{-\infty}^{\infty} \left(\alpha|\psi|^2 + \beta|\psi|^4 + \frac{1}{2m^*} \left| \left(-i\hbar\nabla - \frac{2e\mathbf{A}}{c} \right) \psi \right|^2 \right) dx = 0 \tag{42}
$$

whereby the surface energy can be rewritten

$$
\gamma = \int_{-\infty}^{\infty} \left(\frac{(h - H_c)^2}{8\pi} - \frac{\beta}{2}|\psi|^4 \right) dx \tag{43}
$$

$$
= \frac{H_c^2}{8\pi} \int_{-\infty}^{\infty} \left((1 - \frac{h}{H_c})^2 - \left(\frac{\psi}{\psi_0} \right)^4 \right) dx \tag{44}
$$

Only the interface region contributes to the integral since the two terms in the integrant are equal in the superconducting and in the normal region. The first term will dominate the integral resulting in a positive surface energy when the penetration depth is short compared to the coherence length, since $h \to 0$ when $\psi << \psi_0$. In the opposite limit where the penetration depth is large compared to the coherence length the second term in the integral will dominate and result in a negative surface energy. A more detailed calculation [1] shows that the crossover is equivalent to a $\kappa = \frac{1}{\sqrt{2}}$ giving the two types of superconductors

---

[5]Tinkham [16] p. 122
[1]Ex. Landau and Lifshitz [17] p. 188

$$\begin{aligned} \text{Type} - \text{I}: & \quad \kappa < \tfrac{1}{\sqrt{2}} \quad \gamma > 0 \\ \text{Type} - \text{II}: & \quad \kappa > \tfrac{1}{\sqrt{2}} \quad \gamma < 0 \end{aligned} \tag{45}$$

The consequence of the positive surface energy for type-I superconductors is that magnetic field is penetrating in large regions in order to minimize the Normal-Superconductor(N-S) interface volume and superconductivity breaks down when the applied field reaches the critical field H_C. In Type-II superconductors it is energetically favorable to create the N-S interface and a magnetic field will therefore penetrate in a lot of small normal regions.

Flux quantization

Now one could ask the question if there is a lower limit to the amount of magnetic flux in a normal region caused by a penetrating magnetic field. The answer is that the demand for for the macroscopic wavefunction to be single valued will cause the magnetic flux in a normal region inside a superconductor to the quantized. This is easily shown by evaluating the circulation of the supercurrent (21) around the normal region. If the contour of circulation C_N is chosen a distance much longer than the penetration depth away from the normal region then the supercurrent will be zero.

$$\oint_{C_N} \mathbf{j} \cdot d\mathbf{l} = 0 \Rightarrow \tag{46}$$

$$\Phi = \frac{\hbar c}{2e} \oint \nabla \phi \cdot d\mathbf{l} = \frac{\hbar c}{2e} 2\pi n = \Phi_0 n \tag{47}$$

Here it has been used that the circulation of the vector potential is equivalent to the magnetic flux Φ inside the contour due to the Stoke's relation, $\oint \mathbf{A} \cdot d\mathbf{l} = \int \mathbf{h} d\mathbf{S} = \Phi$. The circulation of the phase gradient will be an integer number times 2π since the wavefunction is single valued and the flux quantum Φ_0 is

$$\Phi_0 = \frac{hc}{2|e|} = 2.07 \cdot 10^{-7} \quad \text{Gcm}^2 \tag{48}$$

Thus the smallest amount of magnetic flux in a normal region in a Type-II superconductor is limited by the flux quantization condition.

2.4 Phase diagram

In a small applied fields a Type-II superconductor will be in the Miessner state where surface currents are preventing the magnetic field from penetrating into the bulk, but at a certain applied field denoted the lower critical field H_{c1} it is energetically favorable to create a normal region carrying one flux quantum in the bulk. Such a normal region is called a flux line or a vortex. The criteria for the first penetration of a flux line is that the Gibbs free energy density integrated over the sample volume is identical with and without the flux line sitting in the sample. By introducing the free energy per unit length ε of the flux line the Gibbs free energy $\tilde{G}$ can be written

$$\tilde{G} = \int G dV = \tilde{F} + L\varepsilon - \int \frac{hH}{4\pi} dV = \tilde{F} + L \left(\varepsilon - \frac{H\Phi_0}{4\pi} \right) \tag{49}$$

where the integral of the magnetic field over the sample volume has been set equal to the flux quantum Φ_0 multiplied with the length L of the flux line, $\int h dV = L\Phi_0$. The last term in the Gibbs energy vanish when the applied field is equal to

$$H_{c1} = \frac{4\pi\varepsilon}{\Phi_0} \tag{50}$$

In order to calculate the line energy ε of the flux line one must first determine the order parameter and the magnetic field distribution of a single flux line.

Isolated flux line solution

The variation of the order parameter at the center of the flux line can be found by a suitable choice of the vector potential and then solving the Ginzburg-Landau equations. One could try to insert an order parameter of the form $\psi = \psi_0 f(r)e^{i\theta}$ and solve for f as was done in section 2.2. Tinkham[1] has followed this approach and got the approximate result that

$$f \approx \tanh\left(\frac{\nu r}{\xi}\right) \qquad \nu \approx 1 \tag{51}$$

Thus the functional form of the order parameter at the flux line center has a close similarity to the reduction of the order parameter at the sample surface given by (33). The order parameter is suppressed in a region at the center of the flux line and increases to its full magnitude when the radial distance is approximately 2ξ. This region is often called the normal core of the flux line.

A considerable simplification in determining the field distribution of a flux line can be obtained if $\kappa \gg 1$, because the core of the flux line can be considered as a singularity $\psi = \psi_0(1 - \delta(\mathbf{r}))$ compared to the length scale of the magnetic field decay given by the penetration depth. This means that the supercurrent around the singularity can be described by equation (21) and a modified London equation is derived similar to the normal London equation (23), but now the circulation around the singularity gives a phase change of 2π resulting in a right hand side equal to a delta function times the flux quantum.

$$-\lambda^2 \nabla^2 \mathbf{h} + \mathbf{h} = +\Phi_0 \delta(\mathbf{r})\hat{\mathbf{e}}_z \tag{52}$$

The solution in polar coordinates $(\hat{\mathbf{e}}_r, \hat{\mathbf{e}}_\theta, \hat{\mathbf{e}}_z)$ valid for distances far from the singularity is

$$\mathbf{h}(r) = \frac{\Phi_0}{2\pi\lambda^2} K_0\left(\frac{r}{\lambda}\right)\hat{\mathbf{e}}_z \qquad r \gg \xi \tag{53}$$

where K_n is the n'th order modified Bessel function of the second kind and here n = 0. The current distribution around the flux line is found from the Maxwell equation

$$\frac{4\pi}{c}\mathbf{j} = \nabla \times \mathbf{h} = \frac{1}{r}\begin{vmatrix} \hat{\mathbf{e}}_r & r\hat{\mathbf{e}}_\theta & \hat{\mathbf{e}}_z \\ \frac{\partial}{\partial r} & \frac{\partial}{\partial \theta} & \frac{\partial}{\partial z} \\ 0 & 0 & h_z(r) \end{vmatrix} = -\frac{\partial h_z(r)}{\partial r}\hat{\mathbf{e}}_\theta \quad \Rightarrow$$

$$\mathbf{j}(r) = \frac{c}{4\pi\lambda}\frac{\Phi_0}{2\pi\lambda^2}K_1\left(\frac{r}{\lambda}\right)\hat{\mathbf{e}}_\theta \qquad r \gg \xi \tag{54}$$

Far from the core the approximation $K_n(x) \sim \frac{e^{-x}}{\sqrt{2\pi x}}, x \gg 1$ show that the field and current is basically decaying exponentially. Close to the core the two functions are approximately[6] $K_0(x) \sim ln x^{-1} + c \quad c = 0.12$ and $K_1(x) \sim x^{-1}$ for $x \ll 1$, which shows that both the field and current is diverging when the core is

---

[1]Tinkham [16] p. 150
[6]M.R. Spiegel [18] section 24

approached. This divergence is non-physical and enters because the core is treated as a singularity. The current will go to zero as the order parameter is suppressed near the vortex center and the field also saturate at a finite value. Figure 5 show the field and order parameter distribution around the flux line.
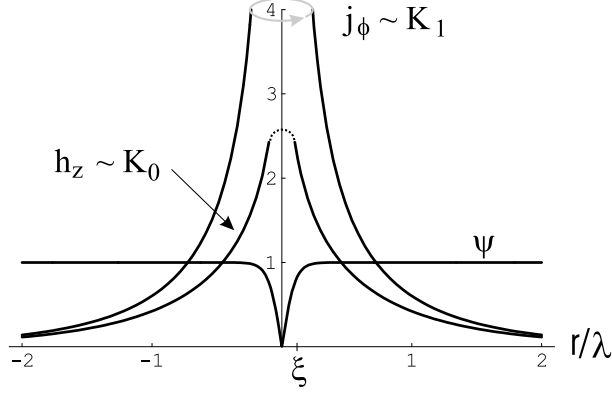

Figure 5. An isolated flux line has a normal core extending a coherence length ξ from the center and a supercurrent j_ϕ is circulating around the core on a length scale given by the penetration depth λ causing a confinement of the magnetic field h_z such that the total flux is equal to a flux quantum Φ_0. The modified Bessel functions K_0 and K_1 plotted in the figure are diverging close to the core, but this is an artifact of the incomplete description of the core in the London model. As the order parameter is suppressed at the core j_ϕ will decrease towards zero and the magnetic field will saturate as marked by the dashed curve.

Line energy

Only the magnetic and the kinetic energy density will contribute to the free energy in the $\kappa \gg 1$ limit, because the core can be neglected

$$\tilde{F} = \int F_{mag} dV + \int F_{kin} dV \tag{55}$$

$$= \int \frac{h^2}{8\pi} dV + \int \frac{1}{2} m^* v_s^2 |\psi_0|^2 dV \tag{56}$$

By relating the velocity $\boldsymbol{v}_s$ of the condensate consisting of particles of mass m^*, charge $e^* = 2e$ and particle density $|\psi_0|^2$ to the current by $\mathbf{j_s} = |\psi_0|^2 2e\mathbf{v_s}$ the kinetic energy term can be rewritten

$$\tilde{F} = \int \frac{h^2}{8\pi} dV + \int \frac{m^*}{8e^2 |\psi_0|^2} j_s^2 dV \tag{57}$$

$$= L \left(\frac{\Phi_0}{4\pi\lambda^2} \right)^2 \int_\xi^\infty \left\{ K_0^2 \left(\frac{r}{\lambda} \right) + K_1^2 \left(\frac{r}{\lambda} \right) \right\} r dr \tag{58}$$

Here the length of the flux line L and the distribution of field and current from (53) and (54) has been introduced. In the usual calculation of the line energy several approximations are made when evaluating the integral above. First of all it is seen from figure 5 that the contribution from the magnetic energy density given by first integral will be small and can be neglected. Secondly only a small

contribution is coming from the region $r > \lambda$, since the current is decaying exponentially, whereby the upper integration limit can be changed to λ. Using the approximation $K_1(x) = x^{-1}$ for $x << 1$ one gets

$$
\begin{aligned}
\tilde{F} &= L \left(\frac{\Phi_0}{4\pi\lambda^2} \right)^2 \int_\xi^\lambda K_1^2 \left(\frac{r}{\lambda} \right) r \, dr \\
&= L \left(\frac{\Phi_0}{4\pi\lambda^2} \right)^2 \int_\xi^\lambda \left(\frac{r}{\lambda} \right)^{-2} r \, dr \\
&= L \left(\frac{\Phi_0}{4\pi\lambda} \right)^2 \ln \left(\frac{\lambda}{\xi} \right)
\end{aligned}
\tag{59}
$$

and the line energy is easily identified

$$
\varepsilon = \left(\frac{\Phi_0}{4\pi\lambda} \right)^2 \ln \left(\frac{\lambda}{\xi} \right)
\tag{60}
$$

Now the critical field for the first flux line entrance into a Type-II superconductor can be found from (50)

$$
\begin{aligned}
H_{c1} &= \frac{\Phi_0}{4\pi\lambda^2} \ln \left(\frac{\lambda}{\xi} \right) \\
&= \frac{H_c}{\sqrt{2}\kappa} \ln \kappa \qquad \kappa >> 1
\end{aligned}
\tag{61}
$$

Thus the fact that the surface energy is negative lead to a new critical field H_{c1}, which is lower that the thermodynamic critical field H_c defined from the condensation energy $\frac{H_c^2}{8\pi} = \frac{\alpha^2}{2\beta} = \frac{1}{8\pi} \left(\frac{\Phi_0}{4\pi} \frac{\sqrt{2}}{\lambda\xi} \right)^2$. If the applied field is increased above the lower critical field H_{c1} more and more flux lines will enter the superconductor and this state is called the mixed state due to the co-existence of superconducting and normal regions.

Upper critical field

The mixed state is suppressed at a field H_{c2} when the density of flux lines becomes so high that the normal cores are overlapping. An infinitely small order parameter is expected at the transition, which can be found by solving a linearized version of the GL equations. Furthermore the GL equations are decoupled, because the magnetic field is basically uniform at the transition. The linearized GL equation is obtained by omitting the 3. order term of (19)

$$
\frac{1}{2m^*} \left(-i\,\hbar\nabla - \frac{2e}{c}\mathbf{A} \right)^2 \psi = |\alpha|\psi
\tag{62}
$$

and this equation has the same functional form as the Scrödinger equation for a particle of mass m^* and charge $e^* = 2e$ in a uniform magnetic field and $|\alpha|$ is equivalent to the energy of the particle. The solution to the Scrödinger equation result in quantized Landau-levels with the lowest energy $E_0 = \frac{1}{2}\hbar\omega_H$ where $\omega_H = \frac{2eH}{m^*c}$. By analogy it is seen that the solution to the GL equation only exist if

$$
|\alpha| > E_0 = \frac{\hbar}{2}\frac{2eH}{m^*c} \Rightarrow
$$

$$
H < \frac{\Phi_0}{2\pi\xi^2}
\tag{63}
$$

The transition field is called the upper critical field H_{c2} and can be related to the thermodynamic field

$$H_{c2} = \frac{\Phi_0}{2\pi\xi^2} = \sqrt{2}\kappa H_c \qquad (64)$$

Thus the upper critical field is increased above the thermodynamic critical field for $\kappa \gg 1$ and it should be noted that $H_{c2} = H_c$ is equivalent to $\kappa = \frac{1}{\sqrt{2}}$ which is the cross over to Type-I superconductivity with positive surface energy.

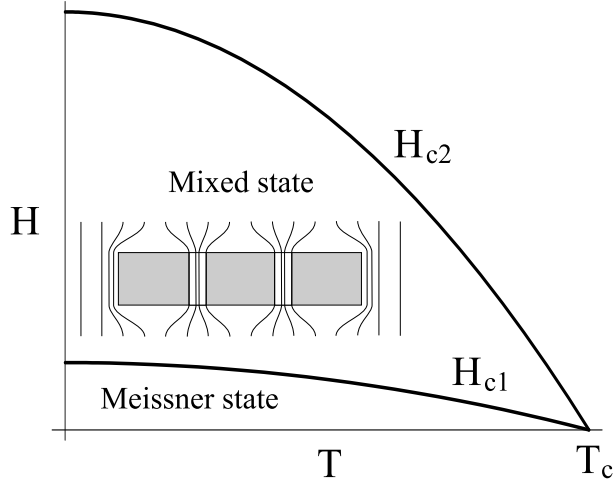Figure 6 shows the (H,T) phase diagram of a Type-II superconductor.

Figure 6. A Type-II superconductor is in the Meissner state with $\mathbf{B} = 0$ below the lower critical field H_{c1} and the applied field is expelled by screening currents flowing at the surface in a region of a thickness given by the penetration depth λ. The applied field penetrates the bulk when it is increased above H_{c1} and the insert shows how the magnetic field is confined in flux lines each carrying one flux quantum Φ_0 in the mixed state. The mixed state is suppressed at the upper critical field H_{c2}, when the normal cores of the flux lines overlap completely.

2.5 Flux line interaction

There will be an overlap between the field and current distributions when two flux lines are present in a superconductor as shown on figure 7 and the interaction energy can be found by evaluating the integral of magnetic and kinetic energy in the $\kappa \gg 1$ limit. It is convenient to insert $\frac{4\pi}{c}\mathbf{j_s} = \nabla \times \mathbf{h}$ into (57) whereby the free energy becomes

$$\tilde{F} = \frac{1}{8\pi} \int h^2 + \lambda^2 (\nabla \times h)^2 dV \qquad (65)$$

This volume integral can be rewritten into a surface integral using the vector relation $\mathbf{D} \cdot (\nabla \times \mathbf{C}) = \mathbf{C} \cdot (\nabla \times \mathbf{D}) + \nabla \cdot (\mathbf{C} \times \mathbf{D})$

$$
\begin{aligned}
\tilde{F} &= \frac{1}{8\pi} \left[\int \mathbf{h} \cdot (\mathbf{h} + \lambda^2 \nabla \times \nabla \times \mathbf{h}) dV + \lambda^2 \int \nabla \cdot (\mathbf{h} \times \nabla \times \mathbf{h}) dV \right] \\
&= \frac{1}{8\pi} \left[\int \mathbf{h} \cdot (\Phi_0 \sum_i \delta(\mathbf{r}_i)\hat{\mathbf{e}}_z) dV + \lambda^2 \int \mathbf{h} \times \nabla \times \mathbf{h} d\mathbf{S} \right] \qquad (66)
\end{aligned}
$$

The modified London equation (52) has been inserted into the first term and since the singularity must be omitted from the integral this term is vanishing. Figure 7 show the surface over which the remaining integral must be calculated and $d\mathbf{S}$ denoted the surface element. The outer boundary can be extended to infinity and will not contribute, since both field and current are decaying exponentially. Also the integral over the top and bottom surface will not contribute, because the integrant $\mathbf{h} \times \nabla \times \mathbf{h} \sim \mathbf{h} \times \mathbf{j}$ is perpendicular to $d\mathbf{S}$. Thus what is left in the integral is the contribution from the surface S_ξ of the core

$$\tilde{F} = \frac{\lambda^2}{8\pi} \left[\int_{S_\xi} \mathbf{h} \times \nabla \times \mathbf{h} d\mathbf{S} \right] \tag{67}$$
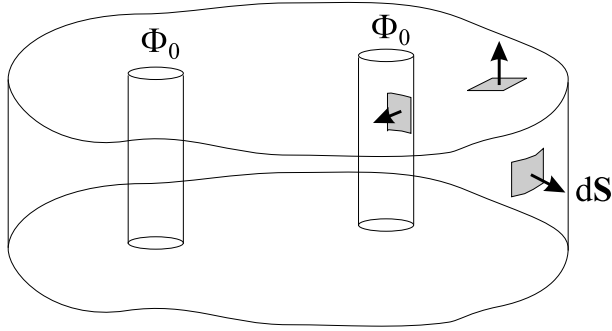

Figure 7. Integration volume when evaluating the free energy of two flux lines Φ_0 in a superconductor. The area element $d\mathbf{S}$ of the surface is pointing outwards and is therefore directed towards the vortex core in the tube of size ξ where the core is omitted from the integral.

In the limit where the flux line cores do not overlap the superconductor can be considered as a linear media with the magnetic field given as a vector sum of the field distribution of each flux line $h = h_1 + h_2$. Inserting this gives

$$\tilde{F} = \frac{\lambda^2}{8\pi} \left[\int_{S_\xi} (\mathbf{h_1} + \mathbf{h_2}) \times \nabla \times (\mathbf{h_1} + \mathbf{h_2})(d\mathbf{S_1} + d\mathbf{S_2}) \right] \tag{68}$$

Four of the terms vanish since $d\mathbf{S}$ is changing direction around the core tube resulting in a cancellation when the integrant has the same direction all over the core tube. Two of the terms only involve the field from the flux line of integration and this just gives the line energy ε of the flux line of length L , whereas the last two terms gives the interaction energy $\tilde{F}_{ij}$ between the flux lines

$$\tilde{F} = 2\tilde{F}_i + \tilde{F}_{ij} = 2\varepsilon L + \tilde{F}_{ij} \tag{69}$$

The two terms in F_{12} only depend on the relative position of the flux lines at $\mathbf{r}_1$ and $\mathbf{r}_2$ making them identical

$$\begin{aligned}
\tilde{F}_{12} &= \frac{\lambda^2}{8\pi} 2 \int_{S_1} \mathbf{h_2} \times \nabla \times \mathbf{h_1} d\mathbf{S_1} \\
&= \frac{\lambda^2}{c} \int_{S_1} \mathbf{h_2} \times \mathbf{j_1} d\mathbf{S_1} \\
&= L \frac{\Phi_0}{4\pi} \mathbf{h_2}(r_2 - r_1) = L \frac{\Phi_0^2}{8\pi^2 \lambda^2} K_0 \left(\frac{r_2 - r_1}{\lambda} \right) \tag{70}
\end{aligned}$$

Here the field and current distribution of an isolated flux line has been inserted and the result is therefore only valid for large separations. The force between the two flux lines is repulsive, since F_{12} decays exponentially with the separation, and by taking the derivative of F_{12} it can be shown that the force $\mathbf{f}$ per unit length on one flux line caused by the current $\mathbf{j}$ of the other flux line is

$$\mathbf{f} = \mathbf{J} \times \frac{\hat{\Phi}_0}{c} \tag{71}$$

where $\hat{\Phi}_0$ has a direction given by the field in the flux core.

2.6 Flux line lattice at low densities

An obvious result of the repulsive interaction between the flux lines is that they tend to order in a regular lattice called the flux line lattice. The structure of the this lattice is however not obvious and will be the issue of this section.

First of all the Gibbs free energy of many flux lines in a sample can be written as

$$
\begin{aligned}
\tilde{G} &= \tilde{F} - \frac{\bar{B}H}{4\pi}LA \\
&= L\left(N\varepsilon - \frac{\bar{B}HA}{4\pi}\right) + \sum_{ij}\tilde{F}_{ij} \\
&= LA\varepsilon n_L\left(1 - \frac{H}{H_{c1}}\right) + \sum_{ij}\tilde{F}_{ij}
\end{aligned}
\tag{72}
$$

where N is the number of flux lines in a sample of thickness L and area A, ε is the line energy of a single flux line, $n_L = \frac{N}{A}$ is the flux line density, $\bar{B} = \frac{\int_A \mathbf{h}dA}{\int_A dA}$ is the average flux density and the interaction term is a sum over all flux lines in the sample. H_{c1} has been introduced in the last line, because $H = \frac{4\pi\varepsilon}{\bar{B}A}$ gives zero Gibbs free energy when there is only one flux line in the sample $N = 1$ and $F_{ij} = 0$. Thus for $H < H_{c1}$ the first term of the Gibbs free energy will be positive and adding a positive interaction energy will result in a minimum of the energy corresponding to a flux line density $n_L = \frac{N}{A} = 0$. This means that the superconductor is in the Meissner state. However for $H > H_{c1}$ the first term becomes negative and adding a positive interacting energy will result in a flux line density $n_L > 0$ corresponding to the mixed state.

In order to determine the equilibrium flux line configuration one can define a general 2D lattice as shown on figure 8 and look for the lattice that gives the lowest minimum of the Gibbs free energy.

It was shown in the previous section that the interaction energy is decaying exponentially for flux lines separated by $d >> \lambda$ and in this limit it is sufficient to include only the nearest neighbor interactions in the free energy. Instead of summing the interaction over the entire sample it is then enough to sum it over the unit cell of the lattice. From the pre-factor of (72) it is clear how to define a Gibbs free energy per unit cell volume $V_u = LA_u$ and normalized by the line energy ε of a single flux line

$$\tilde{g} = \frac{\tilde{G}}{LA_u\varepsilon} = n_L\left(1 - \frac{H}{H_{c1}} + \sum_{ij\in A_u}f_{ij}\right) \tag{73}$$

Above the flux line density n_L has been defined as one flux line per unit cell, which is related to the average flux density $\bar{B}$ in the unit cell
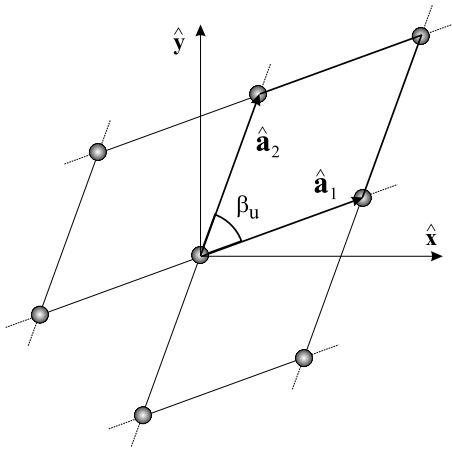
Figure 8. The flux line lattice consist of flux lines directed along the $\hat{z}$-axis and placed at all points $\mathbf{r}_{mn} = m\hat{\mathbf{a}}_1 + n\hat{\mathbf{a}}_2$ in the $\hat{x}\hat{y}$-plane. The unit vectors span a unit cell with an opening angle β_u and an area $A_u = \mathbf{a}_1 \times \mathbf{a}_2 = a^2 \sin(\beta_u)$. Generally the lattice will have a 2-fold symmetry, but the hexagonal and square lattice with $\beta_u = 60^o$ or $\beta_u = 90^o$ are exceptions resulting in 6- and 4-fold symmetry. Each unit cell contains one flux quantum Φ_0 and the average flux density $\bar{B}$ is therefore related to the unit cell area by $\Phi_0 = \bar{B}A_u$. The density of flux lines is $n_L = A_u^{-1} = \frac{\Phi_0}{\bar{B}}$ giving 0.02, 4.8 and 483 μm^{-2} for $\bar{B}$ equal to the earth field (0.5 G), 100 G and 10 kG. The corresponding lattice spacing $a = \sqrt{\frac{1}{n_L \sin(\beta_u)}}$ for the hexagonal lattice is 7.6 μm, 0.5 μm and 49 nm.

$$n_L = \frac{1}{A_u} = \frac{\bar{B}}{\Phi_0} \tag{74}$$

In the scaled Gibbs energy the normalized interaction term becomes

$$f_{ij}(r) = \frac{\tilde{F}_{ij}}{L\varepsilon} = \frac{2}{\ln(\kappa)} K_0\left(\frac{r}{\lambda}\right) \tag{75}$$

with $r = |\mathbf{r}_i - \mathbf{r}_j|$ being the separation between the flux lines.

The interaction energy g_u within the unit cell g_u can now be written down explicitly as the two identical contributions along the unit cell vectors and the two contributions along the diagonals of the unit cell shown in figure 8

$$g_u = \sum_{ij \in A_u} f_{ij} = 2f_{ij}(a) + f_{ij}\left(2a\sin\left(\frac{\beta_u}{2}\right)\right) + f_{ij}\left(2a\cos\left(\frac{\beta_u}{2}\right)\right) \tag{76}$$

where the length of the unit vector a is connected to the flux line density n_L in the unit cell by

$$a = \sqrt{\frac{A_u}{\sin(\beta_u)}} = \sqrt{\frac{1}{n_L \sin(\beta_u)}} \tag{77}$$

Figure 9 shows a plot of the normalized Gibbs free energy given by (73) as function of the flux line density for a flux line lattice of rhombic $\beta_u = 30^o$, hexagonal $\beta_u = 60^o$ and square $\beta_u = 90^o$ symmetry. A slightly lower minimum is obtained for the hexagonal lattice, which will be the equilibrium configuration.

The conditions used for constructing the plot is $\kappa = 10$, $\lambda = 0.08\,\mu m$ and that the applied field is 2 % above the lower critical field giving $\frac{H}{H_{c1}} = 1.02$ in (73).
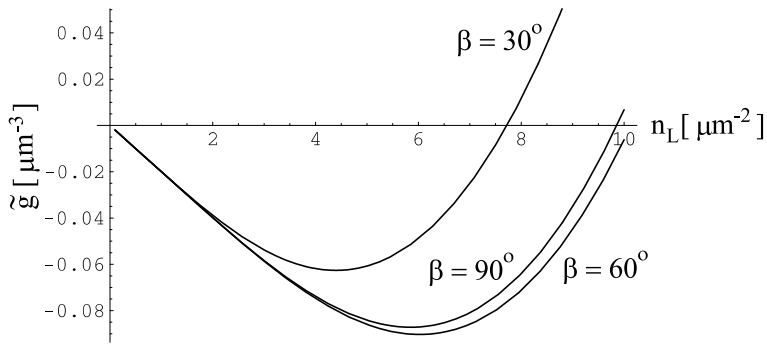
Figure 9. Normalized Gibbs free energy $\tilde{g}$ of a flux line lattice of rhombic, hexagonal and square symmetry as function of the flux line density n_L, when the applied field is 2% higher than the lower critical field H_{c1} (equivalent to $n_L = 28.7 \mu m^{-2}$). The hexagonal lattice result in the lowest minimum and will be the equilibrium configuration of the flux lines. $\kappa = 10$ and $\lambda = 0.08\,\mu m$ has been used to construct the plot.

From the figure it is seen that the minimum energy correspond to a flux line density $n_L \approx 6\,\mu m^{-2}$ and it is interesting to compare this with the flux density equivalent to the lower critical field

$$n_L = \frac{H_{c1}}{\Phi_0} = \frac{\ln \kappa}{4\pi\lambda^2} = 28.7\,\mu m^{-2} \tag{78}$$

Thus the average flux density $\bar{B}$ is smaller than the applied field H, which just reflect a diamagnetic magnetization for $H > H_{c1}$ since $\bar{\mathbf{B}} = \mathbf{H} + 4\pi\mathbf{M}$.

The above analysis was only carried out for one applied field and the stability of the hexagonal lattice will now be shown for all fields in the limit $a >> \lambda$. From the form of (73) it is seen that the deepest minimum in $\tilde{g}$ is found for the smallest interaction term of a given flux line density. Figure (10) shows the relative energy difference between the square and the hexagonal lattice as function of flux line density. At low densities it diverges, but this is just because the interaction is infinitely small, and at higher densities it decreases with the interaction energy of the square lattice being about 5 % higher than the hexagonal lattice at a flux line density equivalent to H_{c1}. Thus the equilibrium lattice at low fields is hexagonal.

A qualitative argument for the stability of the hexagonal lattice is that we seek a packing of circular objects making the separation between the objects as large as possible since they interact repulsively. This is obtained by the hexagonal structure, because the lattice spacing is about 7.5 % larger than for the square lattice at the same flux line density, since $\frac{a_\triangle}{a_\square} = (\sin{(60^o)})^{-\frac{1}{2}} = 1.075$.

2.7   Flux line lattice at intermediate densities

When the separation between the flux lines becomes comparable with the penetration depth one has to consider more than just the nearest neighbor interaction when calculating the Gibbs free energy of the flux line lattice. This can be done in an elegant way by realizing that the field distribution will be identical in every unit cell and it can therefore be represented by a Fourier series. Thus a Fourier method can be constructed for intermediate flux line densities $\xi << a << \lambda$ and it will be outlined in this chapter.
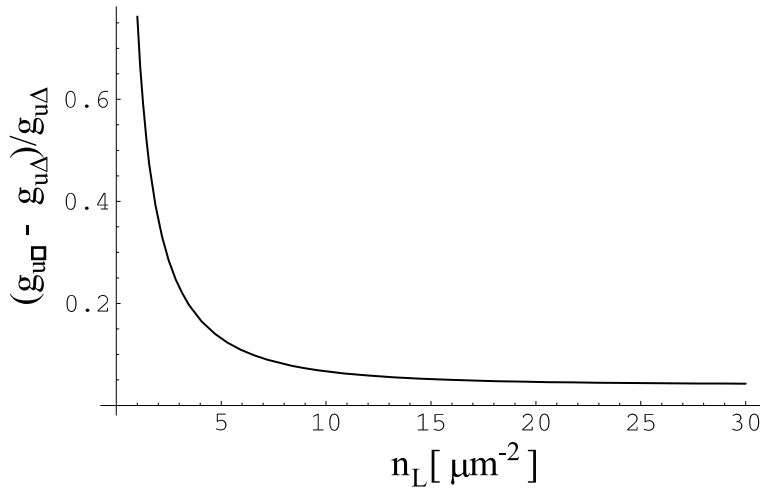
Figure 10. Relative difference between the interaction energy g_u of a square and hexagonal lattice as function of flux line density n_L for a superconductor with $\kappa = 10$ and $\lambda = 0.08\,\mu m$. The equilibrium lattice is hexagonal for all applied fields, since the ratio in the figure is positive for all densities.

Fourier representation of field distribution

The flux line lattice was defined in figure 8 and the field distribution $h(\mathbf{r})$ in every unit cell must be the same in order to full fill the periodicity of the lattice. A consequence of this is that $h(\mathbf{r})$ can be written as a Fourier series

$$h(\mathbf{r}) = \sum_{\mathbf{q}} h_q(\mathbf{q}) e^{i\mathbf{q}\cdot\mathbf{r}} \tag{79}$$

where $\mathbf{q} = h\hat{\mathbf{b}}_1 + k\hat{\mathbf{b}}_2 + l\hat{\mathbf{b}}_3$ are reciprocal lattice vectors with the unit vectors defined from the real space unit vectors $\hat{\mathbf{a}}_1, \hat{\mathbf{a}}_2, \hat{\mathbf{a}}_3$

$$\hat{\mathbf{b}}_1 = 2\pi \frac{\hat{\mathbf{a}}_2 \times \hat{\mathbf{a}}_3}{\hat{\mathbf{a}}_1 \cdot (\hat{\mathbf{a}}_2 \times \hat{\mathbf{a}}_3)} \tag{80}$$

$$\hat{\mathbf{b}}_2 = 2\pi \frac{\hat{\mathbf{a}}_3 \times \hat{\mathbf{a}}_1}{\hat{\mathbf{a}}_2 \cdot (\hat{\mathbf{a}}_3 \times \hat{\mathbf{a}}_1)} \tag{81}$$

$$\hat{\mathbf{b}}_3 = 2\pi \frac{\hat{\mathbf{a}}_1 \times \hat{\mathbf{a}}_2}{\hat{\mathbf{a}}_3 \cdot (\hat{\mathbf{a}}_1 \times \hat{\mathbf{a}}_2)} \tag{82}$$

Figure 11 show the connection between the unit cell of the flux line lattice in real space and the corresponding lattice in reciprocal space. The fourier components $h_q(\mathbf{q})$ of the field are given by

$$h_q(\mathbf{q}) = \frac{1}{v_0} \int_{cell} h(\mathbf{r}) e^{-i\mathbf{q}\cdot\mathbf{r}} d\mathbf{r} \tag{83}$$

and reflects the weight of component with different periodicity. v_0 is the volume of the unit cell, $v_0 = \hat{\mathbf{a}}_1 \cdot (\hat{\mathbf{a}}_2 \times \hat{\mathbf{a}}_3)$.

Free energy based on Fourier representation

The free energy will be the same for every unit cell due to the periodicity of the lattice and in the high-κ limit it can calculated as the sum of the magnetic and kinetic energy density
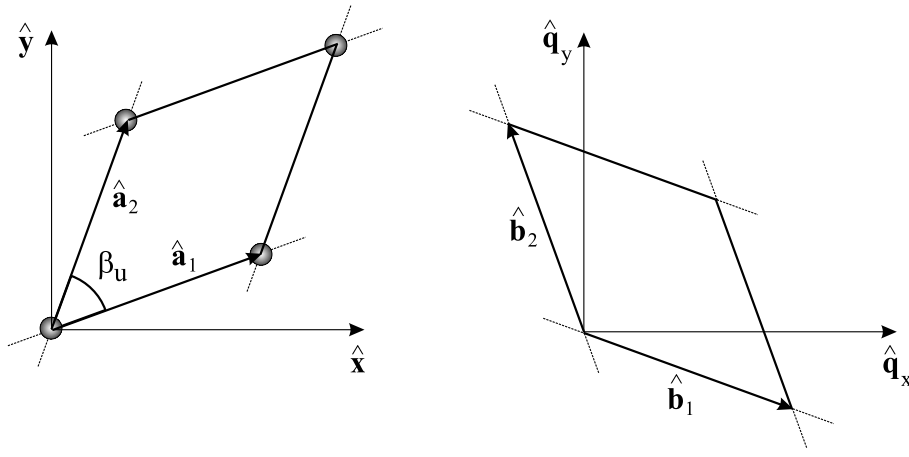
Figure 11. The real space(left) and reciprocal space(right) unit cell have the same symmetry but are rotated by 90 degrees. Here the z axis has been chosen as third unit vector $\hat{\mathbf{a}}_3 = \hat{\mathbf{z}}$ and $\hat{\mathbf{b}}_3 = \hat{\mathbf{q}}_z$. The area of the two unit cells are connected by $A_q = q^2 \sin(\beta_u) = \hat{\mathbf{b}}_1 \times \hat{\mathbf{b}}_2 = \frac{(2\pi)^2}{A_u}$ and the lattice spacing q in reciprocal space is related to the average flux density $\bar{B}$ by $q = 2\pi \sqrt{\frac{1}{\sin(\beta_u)} \frac{\bar{B}}{\Phi_0}}$ giving $9.5 \cdot 10^{-5}$, $1.5 \cdot 10^{-3}$ and $1.5 \cdot 10^{-2}$ $\mathring{A}^{-1}$ for $\bar{B}$ equal to the earth field (0.5 G), 100 G and 10 kG.

$$\tilde{F} = \frac{1}{8\pi} \int_{cell} \left\{ \mathbf{h}^2 + \lambda^2 |\nabla \times \mathbf{h}|^2 \right\} d\mathbf{r} \tag{84}$$

By inserting the Fourier series (79) one gets

$$\tilde{F} = \frac{1}{8\pi} \sum_{\mathbf{q}\mathbf{q}'} \left\{ 1 + \lambda^2 (q_x q_x' + q_y q_y') \right\} h_q(\mathbf{q}) h_q(\mathbf{q}')^* \int_{cell} e^{i(\mathbf{q}-\mathbf{q}')\cdot\mathbf{r}} d\mathbf{r} \tag{85}$$

$$= \frac{v_0}{8\pi} \sum_{\mathbf{q}} h_q^2(\mathbf{q}) \left\{ 1 + \lambda^2 q^2 \right\} \tag{86}$$

The double sum is reduced to a single sum since $\int_{cell} e^{i(\mathbf{q}-\mathbf{q}')\cdot\mathbf{r}} d\mathbf{r} = v_0 \delta(\mathbf{q}\mathbf{q}')$, and the free energy per unit cell simply is

$$\tilde{f} = \frac{\tilde{F}}{v_0} = \frac{1}{8\pi} \sum_{\mathbf{q}} h_q^2(\mathbf{q}) \left\{ 1 + \lambda^2 q^2 \right\} \tag{87}$$

This equation represents the working horse of a calculation scheme for determining the equilibrium flux line lattice at intermediate flux densities, because it shows how to determine the free energy from the fourier components of the field distribution by summing over all reciprocal lattice vectors. Once the free energy is know one can calculate the Gibbs free energy by $\tilde{g} = \tilde{f} - \frac{\bar{B}H}{4\pi}$ and look for the lattice giving the lowest energy minimum. One problem however remains and that is to determine the fourier components of the field distribution. A model is needed for this task and several are available such as the modified London model, the Ginzburg-Landau model or a microscopic model with increasing complexity of the calculations.

Fourier solution to London equation

The simplest model of the flux line lattice is the modified London equation of (52) including the flux lines as a sum of δ functions peaking at the points of the lattice

$$-\lambda^2 \nabla^2 \mathbf{h} + \mathbf{h} = +\Phi_0 \sum_i \delta(\mathbf{r}_i)\hat{\mathbf{e}}_z \tag{88}$$

This can be solved within the unit cell by inserting the fourier series from (79)

$$\sum_\mathbf{q} (1 + \lambda^2 q^2) h_q(\mathbf{q}) e^{i\mathbf{q}\cdot\mathbf{r}} = \frac{\Phi_0}{A_u} \sum_\mathbf{q} e^{i\mathbf{q}\cdot\mathbf{r}} \quad \Rightarrow$$

$$h_q(\mathbf{q}) = \frac{\Phi_0}{A_u(1 + \lambda^2 q^2)} = \frac{\bar{B}}{(1 + \lambda^2 q^2)} \tag{89}$$

where A_u is the unit cell area connected to the average flux density by $\Phi_0 = \bar{B}A_u$.

The Fourier solution still suffer from the insufficient description of the core of size ξ, which is seen by evaluating the field at the core center

$$
\begin{aligned}
h(0) \;&=\; \bar{B} \sum_\mathbf{q} \frac{e^{i\mathbf{q}\cdot\mathbf{0}}}{1 + \lambda^2 q^2} \\
&\approx\; \bar{B}\left(1 + \frac{1}{\lambda^2} \sum_{\mathbf{q}\neq\mathbf{0}} \frac{1}{q^2}\right) \quad \text{for} \quad (\lambda q)^2 \gg 1 \\
&\approx\; \bar{B}\left(1 + \frac{1}{\lambda^2 (2\pi)^2 n_L} \int_{q_{min}}^\infty \frac{1}{q^2} 2\pi q\, dq\right) \\
&\approx\; \bar{B}\left(1 + \frac{1}{\lambda^2 2\pi n_L} \left[\ln(q)\right]_{q_{min}}^\infty\right)
\end{aligned}
\tag{90}
$$

A divergence is found as the reciprocal lattice vector goes to infinity, which corresponds to small structures in real space and a cut-off at $q_{max} = \frac{2\pi}{\xi}$ must be introduced in the summation, because the core is represented as an singularity in the London model. The approximation $(\lambda q)^2 \gg 1$ is valid for $\kappa \gg 1$ and fields $H \gg H_{c1}$. Also the summation has been replaced by an integration to simplify the evaluation and the density of q-vectors is $n_q = \frac{1}{(2\pi)^2 n_L}$. The lower q limit is set by the lattice spacing a giving $q_{min} = \frac{2\pi}{a}$ and by inserting the flux line density $n_L = \frac{\bar{B}}{\Phi_0}$ one gets

$$
\begin{aligned}
h(0) \;&\approx\; \bar{B} + \frac{\Phi_0}{2\pi\lambda^2} \left[\ln(q)\right]_{\frac{2\pi}{a}}^{\frac{2\pi}{\xi}} \\
&\approx\; \bar{B} + \frac{2H_{c1}}{\ln\kappa} \ln\frac{a}{\xi}
\end{aligned}
\tag{91}
$$

Thus at low flux line densities where $a \approx \lambda$ the field is about two times H_{c1} higher at the center of the flux line than the average flux density $\bar{B}$ in the unit cell. This modulation of the field in the unit cell is decreasing at higher flux line densities, because the lattice spacing will approach ξ, where the modulation vanish

$$h(0) \;\approx\; \bar{B} + \frac{2H_{c1}}{\ln\kappa} \ln\left(\frac{1}{\xi}\sqrt{\frac{\Phi_0}{\sin(\beta_u)\bar{B}}}\right) \tag{92}$$

Following this approach the flux density distribution can be found in the entire unit cell and also the average flux density $\bar{B}$ minimizing the Gibbs free energy at different applied fields H can be determined giving the magnetization curve of type-II superconductors as shown in figure 12.

Fourier solution from the Ginzburg-Landau equation

An approximate solution to the Ginzburg-Landua equations has been obtained by Clem *et. al.* [19] and in the high-κ limit the fourier components are given by [20]

$$h_z(q) = \frac{\Phi_0}{A_u}\frac{gK_1(g)}{1+\lambda^2 q^2} \quad g = \sqrt{2}\xi(q^2 + \lambda^{-2})^{\frac{1}{2}} \tag{93}$$

$$\approx \frac{\Phi_0}{A_u}\frac{1}{1+\lambda^2 q^2}\exp\left(-\sqrt{2}\xi q\right) \tag{94}$$

where Φ_0 is the flux quantum, A_u is the area of the unit cell, λ the penetration depth, ξ the coherence length and $K_1(x)$ is the first order modified Bessel function of the second kind. This equation have a strong similarity to the London solution, but the additional exponential factor introduces a suppression of the fourier components at high q values corresponding to length scales of the size of the core ξ. The exponential factor has a similar effect as the artificial cut-off at q_{max} introduced in the London calculation (90) above.

The Fourier method will be treated later when explaining the observation of a flux line lattice with square symmetry in the borocarbide superconductors.
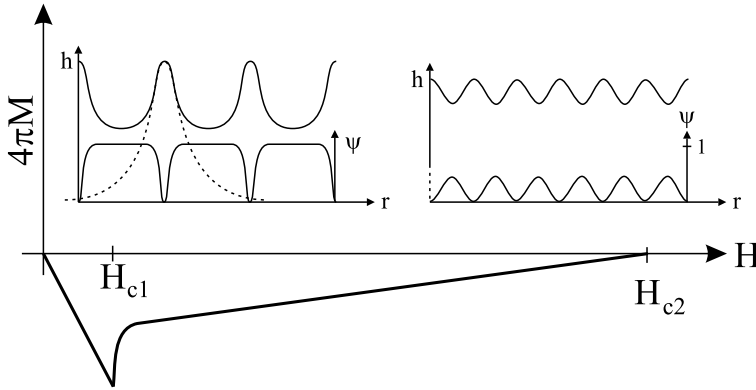

Figure 12. Magnetization curve of a type-II superconductor showing the difference $4\pi M = \bar{B} - H$ between the average flux density $\bar{B}$ and the applied field H. The Meissner screening is seen as a diamagnetic response below H_{c1} and the gradual increase of the density of flux lines above H_{c1} causes an decrease of the diamagnetic response as H_{c2} is approached. The inserts illustrates the field $h(\mathbf{r})$ and order parameter $\psi(\mathbf{r})$ distribution of the flux line lattice at intermediate(left) and high(right) flux line densities n_L. At intermediate flux line densities the order parameter reaches its saturation value ($\psi(\mathbf{r}) \to 1$) in between the flux lines and the modulation of the field $h(\mathbf{r})$ is highly peaked at the position of the flux lines. The dashed curve shows the field distribution of an isolated flux line and the resulting field distribution is simply a superposition of these sitting at all lattice positions. A reduction of the order parameter ($\psi(\mathbf{r}) < 1$) is seen at high flux line densities when the flux line separation becomes comparable to the coherence length ξ as found by solving the GL equations. This result in a reduced modulation of the magnetic field and the superposition of field distributions of an isolated flux line is not valid.

2.8 Flux line lattice at high densities

Historically the stability of the hexagonal flux line lattice was first proved by A.Abrikosov, who used the linearized GL equation to show that the free energy

at the upper critical field H_{c2} can be given by [7]

$$F_A = \frac{1}{8\pi}\left(B^2 - \frac{(H_{c2}-B)^2}{1+(2\kappa^2-1)\beta_A}\right) \tag{95}$$

where the parameter $\beta_A = \frac{<\psi^4>}{<\psi^2>^2}$ depend on the spatial average $<>$ of a periodic order parameter ψ corresponding to the lattice. β_A is independent of the size of this order parameter, but will only depend on the symmetry of the lattice and from the free energy above it is seen that the lowest free energy is obtained by the lattice having the lowest β_A. Numerical calculations show that $\beta_{A\square} = 1.18$ and $\beta_{A\triangle} = 1.16$ for the square and hexagonal lattice respectively. Thus the equilibrium lattice is hexagonal and the free energy difference is about 2%.

One has to solve the full GL equations in order to determine the field and order parameter distribution when the cores are overlapping in the field region near H_{c2}. This has been done by many people[8] and the main result is illustrated on the insert on figure 12 showing that the order parameter is reduced below the saturation value ψ_0 and the magnetic flux density is only varying slightly from the average magnetic flux density $\bar{B}$. Still the magnetic flux in every unit cell of the lattice is one flux quantum Φ_0 caused by circulating currents seen as a phase change of the order parameter around a flux line.

2.9 Anisotropy

The superconducting length scales were assumed isotropic in the previous chapters, but by looking at the microscopic relations (34) and (35) it is seen that they depend on the Fermi velocity, which can have a large directional dependence in anisotropic crystals. Thus the ratio between the penetration depth in different directions reflects the anisotropy of the Fermi velocities and one can define an anisotropy parameter as

$$\Gamma = \frac{\lambda_i}{\lambda_j} = \frac{\xi_j}{\xi_i} \quad i,j = x,y,z \tag{96}$$

Note that the coherence length anisotropy is the inverse of the penetration depth anisotropy.

More generally the relation between current density and vector potential given by (21) and (22) resulting in the London equation must also be extended to include the anisotropy of the penetration depth.

$$\frac{4\pi}{c}\mathbf{j} = \frac{1}{\lambda^2}\left(\frac{\hbar c}{2e}\nabla\phi - \mathbf{A}\right) \tag{97}$$

By combining the phase of the condensate and the vector potential into a quantity $\boldsymbol{a}$

$$\boldsymbol{a} = \frac{\hbar c}{2|e|}\nabla\phi + \mathbf{A} = \frac{\Phi_0}{2\pi}\nabla\phi + \mathbf{A} \tag{98}$$

the London relation can be written as

$$\frac{4\pi}{c}j_i = -\frac{1}{\lambda^2}a_j \tag{99}$$

where a summation over indexes $i,j = x,y,z$ is omitted for clarity. From the microscopic relation of the penetration depth given by (35) it is seen that the

---

[7] deGennes [15] p. 206
[8] See Review by Brandt [21]

anisotropy of the Fermi surface can be expressed as a directional dependence on the "inverse" mass of the particles in the condensate in the Ginzburg-Landau theory

$$
\begin{aligned}
\lambda(T)^{-2} &= \frac{16\pi e^2 |\psi_0|^2}{m^* c^2} \\
&\sim \frac{e^2}{c^2} N(0) v_F^2 \left(\frac{T_c - T}{T_c} \right)
\end{aligned}
\tag{100}
$$

An inverse mass tensor with elements of the type $< v_i v_j >$, where $<>$ denotes an average over the Fermi surface and v_i is the Fermi velocity along direction i, can be introduced and the normalization of the matrix elements is given by $det(< v_i v_j >)^{\frac{1}{3}}$ (for cubic crystal structure the normalization is simply $< v^2 > /3$) [22]

$$
m_{ij}^{-1} = \frac{< v_i v_j >}{det(< v_i v_j >)^{\frac{1}{3}}}
\tag{101}
$$

Thus the London relation becomes

$$
\frac{4\pi}{c} j_i = -\frac{m_{ij}^{-1}}{\lambda^2} a_j
\tag{102}
$$

with penetration depths along the principal axes given by

$$
\lambda_i = \sqrt{m_{ii}}\lambda \quad i = a, b, c
\tag{103}
$$

and

$$
\lambda = (\lambda_a \lambda_b \lambda_c)^{\frac{1}{3}}
\tag{104}
$$

Figure 13 show how the shape of a flux line is changes into an ellipse when it is sitting in an anisotropic superconductor. It should be noted that the field decay in the a direction is determined by the current in the b direction and thereby the penetration depth λ_b. Similar arguments lead to the conclusion that the flux line lattice is distorted by the anisotropic overlap between field and current distributions. This distortion can be found by stating that if the interaction energy (70) between two flux lines sitting along a or b should be the same then the separation should be r_a and r_b respectively

$$
K_0(\frac{r_a}{\lambda_b}) = K_0(\frac{r_b}{\lambda_a}) \quad \Rightarrow r_a = \frac{\lambda_b}{\lambda_a} r_b
\tag{105}
$$

2.10   Collective pinning

Flux lines are attracted to points in a superconductor where the order parameter has been reduced by crystalline defects or impurities, because the condensation energy is lost in the normal core of the flux line and this lost is reduced if the point of a suppressed order parameter is included in the core. This effect is called pinning of flux lines to pinning cites and a flux line lattice therefore tend to deform in order to take advantage of placing the pinning cites in the cores, but the deformations are limited by the repulsive interaction between the flux lines. Here the theory of collective pinning by Larkin and Ovchinnikov is outlined [9].

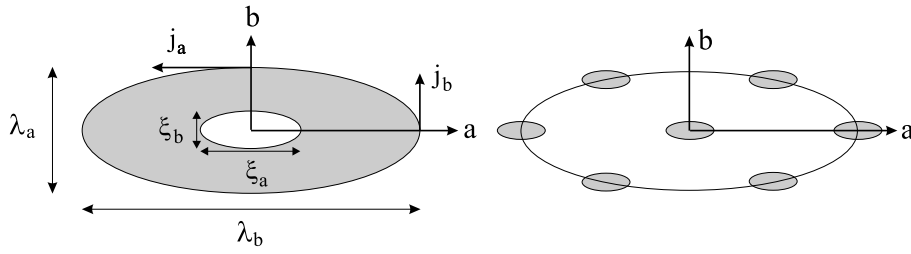
[9][23] or see Tinkham [16] p. 348

Figure 13. Left: Elliptical shape of the core and field distribution of a flux line in an anisotropic superconductor with $\frac{\lambda_b}{\lambda_a} = \frac{\xi_a}{\xi_b} > 1$. The field decay in a certain direction a (or b) is determined by the perpendicular current flow j_b (or j_a). Right: The flux line lattice is also distorted by the penetration depth ratio due to the anisotropic overlap of the flux lines.

Pinning force

In the high-κ limit the condensation energy loss of a flux line core and a pinning cite can approximately be added to the free energy by

$$\tilde{F_{pin}} = \tilde{F}_{kin} + \tilde{F}_{mag} + \int \frac{\psi(r)}{\psi_0} \frac{H_c^2}{8\pi} \pi \xi^2 dl + \frac{H_c^2}{8\pi} \frac{4}{3} \pi \xi^3 \tag{106}$$

where the first two terms include the kinetic and magnetic energy of the flux line, the third term is an integral of the lost of condensation energy density $\frac{H_c^2}{8\pi}$ along the flux line with a cross sectional area $\pi\xi^2$ and the last term is the lost of condensation energy density in a sphere of volume $\frac{4}{3}\pi\xi^3$ around the pinning cite. Thus it cost less condensation energy to position the flux line with the pinning cite included in the core and the pinning cite thereby acts as a energy well of a depth u approximately given by

$$u = \frac{H_c^2}{8\pi} \frac{4}{3} \pi \xi^3 \tag{107}$$

giving a force on the flux line of the order

$$f_{pin} = \frac{\delta u}{\delta x} \approx \frac{u}{\xi} \tag{108}$$

From the form of u it is seen that the pinning force will depend on both field and temperature, since both the condensation energy and the coherence length change with these variables.

Larkin-Ovchinnikov theory

Larkin and Ovchinnikov have addressed the problem of taking advantage of having the pinning sites in the cores of the flux lines in a lattice and the cost of deforming the lattice elastically [23]. They solved the problem by summing the pinning forces like a random-walk in a unit volume and then assumed that the flux line lattice was deformed collectively in the same unit volume due to the interaction between the flux lines. The size of the correlated unit volume then depends on the balance between the energy gain of the pinning sites and the increase in elastic deformation. Figure 14 illustrates the collective volume which is generally cigar shaped with different extends L_c along and R_c perpendicular to the flux lines. In a simple box approximation they are related by $V_c = R_c^2 L_c$. The elastic energy due to deformation of the flux line lattice is most easily formulated from the tilt $s_t = \frac{\delta x}{L_c}$

and shear $s_s = \frac{\delta x}{R_c}$ strain as shown on figure 14 and the elastic constants for tilt and shear deformation C_{44} and C_{66}

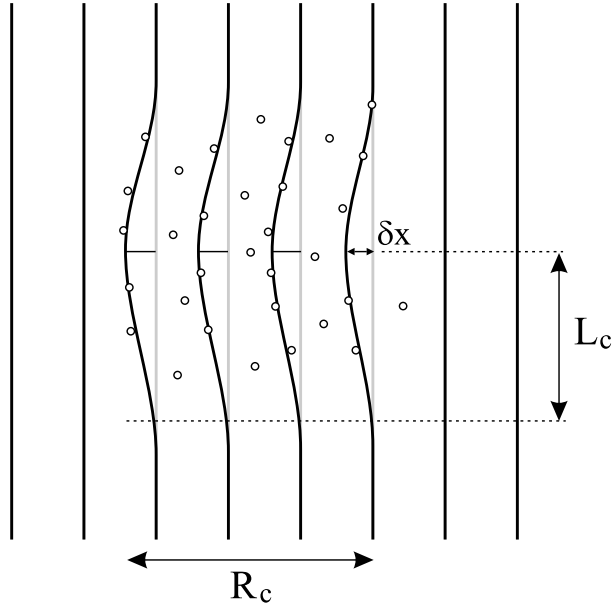$$\delta F_e = \frac{1}{2}C_{44}s_t^2 + \frac{1}{2}C_{66}s_s^2 \tag{109}$$

Figure 14. Flux lines are strait and ordered in the flux line lattice, when no pinning sites are present in the sample. The flux line lattice will however break up into smaller well ordered volumes in the presence of pinning sites, as shown in the central part of the figure. All flux lines in the correlated volume $V_c = R_c^2 L_c$ are distorted by δx and the corresponding tilt strain is $s_t = \frac{\delta x}{L_c}$. A distortion of the flux line positions in the lattice also result and gives a shear strain of $s_s = \frac{\delta x}{R_c}$. The size of the correlated volume is controlled by the balance between the pinning energy and the elastic energy due to the strain of the flux line lattice.

In a random-walk the extend of the walk is given by the square root of the number of steps in the walk multiplied with the step length. By analogy the random pinning energy of the flux line lattice is given by the number of pinning cites N_p and the energy gain $u_{pin} = \xi f_{pin}$ per cite

$$\delta F_{pin} = \sqrt{N_p} u_{pin} \Rightarrow$$
$$\frac{\delta F_{pin}}{V_c} = \frac{\xi f_{pin}\sqrt{n_p}}{\sqrt{V_c}} \tag{110}$$

where the pinning force f_{pin} and density of pinning cites $n_p = \frac{N_p}{V_c}$ has been introduced.

The free energy change due to collective pinning can be written by noticing that the distortion due to pinning will be of the order $\delta x = \xi$

$$\delta F = \frac{1}{2}C_{44}\left(\frac{\xi}{L_c}\right)^2 + \frac{1}{2}C_{66}\left(\frac{\xi}{R_c}\right)^2 - \frac{\xi f_{pin}\sqrt{n_p}}{\sqrt{V_c}} \tag{111}$$

By minimizing this with respect to R_c and L_c one gets the following relations between the elastic constants, the pinning strength $w = n_p f_{pin}^2$ and the dimensions of the correlated volume

$$\frac{R_c}{L_c} = \sqrt{\frac{1}{2}\frac{C_{66}}{C_{44}}} \tag{112}$$

$$R_c = \frac{\sqrt{2}C_{44}^{\frac{1}{2}}C_{66}^{\frac{3}{2}}\xi^2}{w} \tag{113}$$

$$L_c = \frac{2C_{44}C_{66}\xi^2}{w} \tag{114}$$

$$V_c = \frac{4C_{44}^2 C_{66}^4 \xi^6}{w^3} \tag{115}$$

$$\delta F = -\frac{w^2}{8C_{44}C_{66}^2\xi^2} \tag{116}$$

Thus the correlated volume decreases with an increased pinning strength w and decreasing elastic modula C_{44} and C_{66}.

It was show in section 2.5 that a current result in a force acting on a flux line and the force per unit volume is $f_J = \frac{J\Phi_0}{c}n_L = \frac{J\bar{B}}{c}$. A critical current density J_c can be defined from this by setting f_J equal to the random walked pinning force density

$$f_J = \frac{J_c\bar{B}}{c} = f_{pin}\sqrt{\frac{n_p}{V_c}} = \frac{w^2}{2C_{44}C_{66}^2\xi^3} \tag{117}$$

This relates the Larkin-Ovchinnikov theory to transport measurements.

2.11 Generic phase diagram

The flux line lattice can be considered as a system of elastic strings coupled together by elastic forces determine by the elastic modula. Distortions away from the equilibrium position can be caused by pinning centers as discussed with the collective pinning model, but thermal fluctuations can cause dynamic distortions and if the fluctuation becomes sufficiently strong compared to the elastic force the flux line lattice can melt. Figure 15 show the generic phase diagram for the flux line phases in type-II superconductors containing randomly distributed pinning centers. Another melting region is present close to H_{c1} where the flux line interactions are very week due to the low flux line density, however this line is not shown in the figure.
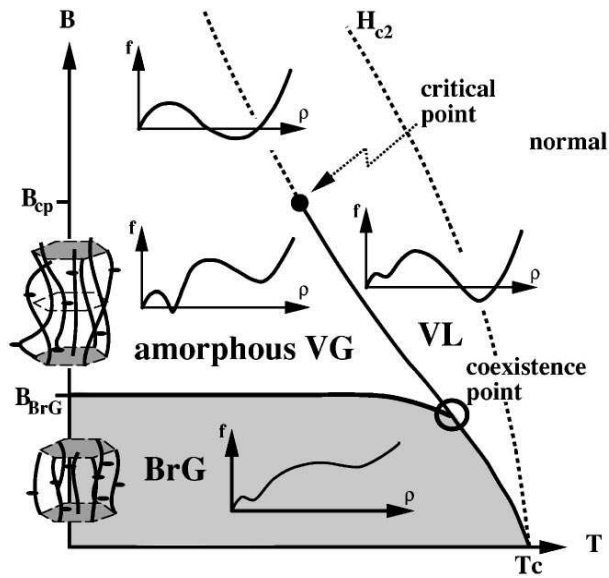
Figure 15. Phase diagram of flux lines in a superconductor containing pinning sites. The Bragg glass(BrG) is stable at low field and temperature, where the flux line lattice is only slightly distorted by pinning sites and the lattice contains no dislocation as seen by the free energy minimum of dislocation at $\rho = 0$ on the insert. Dislocation start to occur in the lattice at higher fields and this phase is called the amorphous vortex glass(VG). Thermal fluctuation will enhance the mobility of the dislocations and a vortex liquid(VL) is present below the H_{c2} curve. The figure represent the phase diagram of a high temperature superconductor, but it is equivalent for a low-T_c superconductor with the difference that the liquid region is moved much closer to the H_{c2} line. Taken from Kierfeld et. al. [24]

3 Neutron scattering on flux line lattice

The neutron is a charge neutral elementary particle with a magnetic moment $\boldsymbol{\mu}_n$ and it is ideal for studying the flux line lattice, since the neutron is sensitive to the local magnetic field as it passes through a sample and is only weakly absorbed due to the charge neutrality [10]. A neutron can be scattered on the flux line lattice, because the interaction with the sample will cause perturbations to the wavefunction of the incident neutron and if the perturbations add up constructively it result in a finite probability of having a neutron propagating away from the sample into a new direction. Here the scattering cross section for neutron scattering on magnetic structures is introduced in a rather detailed way leading to a correlation function description.

3.1 Partial Differential cross section

The partial differential cross section is defined as the number of neutrons scattered per second into a solid angle $d\Omega$ and with energies in the range E' to $E' + dE'$ divided by the flux of incident neutrons. Integrating this quantity over all neutron energies gives the differential cross section

$$\frac{d\sigma}{d\Omega} = \int_{-\infty}^{\infty} \frac{d^2\sigma}{d\Omega dE'} dE' \tag{118}$$

and by further integration over all directions one get the total cross section which is the number of neutrons scattered per second from the sample normalized with the incident neutron flux

$$\sigma_{tot} = \int_{\Omega} \frac{d\sigma}{d\Omega} d\Omega \tag{119}$$

The partial differential cross section can be found from 1. order perturbation theory and is directly connected to the matrix element for transitions of the total system consisting of the neutron and the sample. By denoting the state of the system by the wavefunction $|\boldsymbol{k}\sigma\lambda>$, where $|\boldsymbol{k}\sigma> = \exp{(i\boldsymbol{k}\cdot\boldsymbol{r})}|\sigma>$ is a plane wave description of the neutron with wavevector $\boldsymbol{k}$ and spin-state $|\sigma>$, and $|\lambda>$ is the state of the sample, one can write [11]

$$\frac{d^2\sigma}{d\Omega dE'} = \frac{k'}{k}\left(\frac{m}{2\pi\hbar^2}\right)^2 \sum_{\lambda\lambda'} P_\lambda \sum_{\sigma\sigma'} P_\sigma |<\boldsymbol{k}'\sigma'\lambda'|V|\boldsymbol{k}\sigma\lambda>|^2 \delta(E_\lambda - E_{\lambda'} + E - E') \tag{120}$$

Here the matrix elements gives the probability for a change of the system from the initial state $|\boldsymbol{k}\sigma\lambda>$ into $|\boldsymbol{k}'\sigma'\lambda'>$ and the δ - function ensures energy conservation where E_λ and E is the energy of the sample state and the neutron. The summation is over all initial states with probability P and final states. The pre-factor arise from normalization and the density of final neutron states in $d\Omega$ of the scattered neutron $\boldsymbol{k}'$. m is the neutron mass and $\hbar$ is Planck's constant.

A neutron can interact with matter through the potential of the nucleus of atoms or the dipole potential of the neutron moment in a magnetic field $\boldsymbol{B}$.

---

[10] Large absorption is caused by nuclear reactions in some elements such as Gd, B and Li.

[11] See Squires [25] section 2.3

$$V = \sum V_{nuc} + \boldsymbol{\mu_n} \cdot \boldsymbol{B(r)} \tag{121}$$

In the following the focus will be on the magnetic interaction and by inserting the plane wave representation of the neutron on gets

$$\frac{d^2\sigma}{d\Omega dE'} = \frac{k'}{k}\left(\frac{m}{2\pi\hbar^2}\right)^2 \sum_{\lambda\lambda'} P_\lambda \sum_{\sigma\sigma'} P_\sigma \left| \int \exp\left(-i\boldsymbol{k'}\cdot\boldsymbol{r}\right) <\sigma'\lambda'|\boldsymbol{\mu_n}\cdot\boldsymbol{B(r)}|\sigma\lambda> \exp\left(i\boldsymbol{k}\cdot\boldsymbol{r}\right)d\boldsymbol{r} \right|^2$$
$$\times\delta(E_\lambda - E_{\lambda'} + E - E') \tag{122}$$

where the integration is carried out over the neutron coordinate. The neutron moment $\boldsymbol{\mu_n}$ is given by the product of the gyromagnetic ratio $\gamma = 1.913$, the nuclear magneton $\mu_N = \frac{e\hbar}{2m}$ and the Pauli spin operator $\boldsymbol{\sigma}$ with eigenvalues of ± 1.

$$\boldsymbol{\mu_n} = -\gamma\mu_N\boldsymbol{\sigma} \tag{123}$$

By inserting this in the partial differential cross section equation one gets the following prefactor

$$\left(\frac{m}{2\pi\hbar^2}\right)^2 \gamma^2 \left(\frac{e\hbar}{2m}\right)^2 = \left(\frac{\gamma e}{2h}\right)^2 \tag{124}$$

and

$$\frac{d^2\sigma}{d\Omega dE'} = \left(\frac{\gamma e}{2h}\right)^2 \frac{k'}{k} \sum_{\lambda\lambda'} P_\lambda \sum_{\sigma\sigma'} P_\sigma \left| \int <\sigma'\lambda'|\boldsymbol{\sigma}\cdot\boldsymbol{B(r)}|\sigma\lambda> \exp\left(i\boldsymbol{\kappa}\cdot\boldsymbol{r}\right)d\boldsymbol{r} \right|^2$$
$$\times\delta(E_\lambda - E_{\lambda'} + E - E') \tag{125}$$

where the momentum transfer vector is given by $\boldsymbol{\kappa} = \boldsymbol{k} - \boldsymbol{k'}$. A double integral can replace the square of the matrix elements

$$\frac{d^2\sigma}{d\Omega dE'} = \left(\frac{\gamma e}{2h}\right)^2 \frac{k'}{k} \sum_{\lambda\lambda'} P_\lambda \sum_{\sigma\sigma'} P_\sigma \int\int <\sigma'\lambda'|\boldsymbol{\sigma}\cdot\boldsymbol{B(r_1)}|\sigma\lambda>^* <\sigma'\lambda'|\boldsymbol{\sigma}\cdot\boldsymbol{B(r_2)}|\sigma\lambda>$$
$$\times \exp\{i\boldsymbol{\kappa}\cdot(\boldsymbol{r_2} - \boldsymbol{r_1})\}d\boldsymbol{r_1}d\boldsymbol{r_2}\delta(E_\lambda - E_{\lambda'} + E - E') \tag{126}$$

The δ- function in energy can be represented as a time integral

$$\delta(E_\lambda - E_{\lambda'} + E - E') = \frac{1}{2\pi\hbar}\int_{-\infty}^{\infty} \exp\left(\frac{i(E_{\lambda'} - E_\lambda)t}{\hbar}\right)\exp\left(-i\omega t\right)dt \tag{127}$$

where ω is given by the energy difference between the incident and scattered neutron $\hbar\omega = E - E'$. Using this relation one can change the operators into the time depend Heisenberg representation by noting that $\exp\left(\frac{-iHt}{\hbar}\right)|\lambda> = \exp\left(\frac{-iE_\lambda t}{\hbar}\right)|\lambda>$

$$\frac{d^2\sigma}{d\Omega dE'} = \left(\frac{\gamma e}{2h}\right)^2 \frac{1}{2\pi\hbar}\frac{k'}{k} \int\int\int \sum_{\lambda\lambda'} P_\lambda \sum_{\sigma\sigma'} P_\sigma <\sigma\lambda|\boldsymbol{\sigma}\cdot\boldsymbol{B(r_1,0)}|\sigma'\lambda'> <\sigma'\lambda'|\boldsymbol{\sigma}\cdot\boldsymbol{B(r_2,t)}|\sigma\lambda>$$
$$\times \exp\{i\boldsymbol{\kappa}\cdot(\boldsymbol{r_2} - \boldsymbol{r_1})\}\exp\left(-i\omega t\right)d\boldsymbol{r_1}d\boldsymbol{r_2}dt \tag{128}$$

Now the summation over the spin states will be carried out for an unpolarized neutron beam with equal probability for having spin up and spin down, $P_u = P_d = \frac{1}{2}$. The Pauli operator acting on the field can be split up into the x, y and z component

$$\boldsymbol{\sigma} \cdot \boldsymbol{B}(\boldsymbol{r}) = \sigma_x B_x + \sigma_y B_y + \sigma_z B_z = \sum_{\alpha=x,y,z} \sigma_\alpha B_\alpha \tag{129}$$

whereby the summation can be written as

$$\sum_{\lambda\lambda'} P_\lambda \sum_{\sigma\sigma'} P_\sigma < \sigma\lambda|\boldsymbol{\sigma}\cdot\boldsymbol{B}(\boldsymbol{r}_1,0)|\sigma'\lambda' >< \sigma'\lambda'|\boldsymbol{\sigma}\cdot\boldsymbol{B}(\boldsymbol{r}_2,t)|\sigma\lambda >$$

$$= \sum_{\lambda\lambda'} P_\lambda \sum_{\sigma\sigma'} P_\sigma < \sigma\lambda|\sum_\alpha \sigma_\alpha B_\alpha(\boldsymbol{r}_1,0)|\sigma'\lambda' >< \sigma'\lambda'|\sum_\beta \sigma_\beta B_\beta(\boldsymbol{r}_2,t)|\sigma\lambda' >$$

$$= \sum_{\alpha,\beta} \sum_{\lambda\lambda'} P_\lambda \sum_{\sigma\sigma'} P_\sigma < \sigma|\sigma_\alpha|\sigma' >< \sigma'|\sigma_\beta|\sigma >< \lambda|B_\alpha(\boldsymbol{r}_1,0)|\lambda' >< \lambda'|B_\beta(\boldsymbol{r}_2,t)|\lambda >$$

$$= \sum_{\alpha,\beta} \left\{ \sum_{\sigma\sigma'} P_\sigma < \sigma|\sigma_\alpha|\sigma' >< \sigma'|\sigma_\beta|\sigma > \right\} \left\{ \sum_{\lambda\lambda'} P_\lambda < \lambda|B_\alpha(\boldsymbol{r}_1,0)|\lambda' >< \lambda'|B_\beta(\boldsymbol{r}_2,t)|\lambda > \right\}$$

$$= \sum_{\alpha,\beta} \left\{ \sum_\sigma P_\sigma < \sigma|\sigma_\alpha\sigma_\beta|\sigma > \right\} \left\{ \sum_\lambda P_\lambda < \lambda|B_\alpha(\boldsymbol{r}_1,0)B_\beta(\boldsymbol{r}_2,t)|\lambda > \right\}$$

$$= \sum_{\alpha,\beta} \{P_u < u|\sigma_\alpha\sigma_\beta|u > +P_d < d|\sigma_\alpha\sigma_\beta|d >\} \left\{ \sum_\lambda P_\lambda < \lambda|B_\alpha(\boldsymbol{r}_1,0)B_\beta(\boldsymbol{r}_2,t)|\lambda > \right\} \tag{130}$$

The properties of the Pauli operators result in the following matrix elements

$$\begin{aligned} < u|\sigma_\alpha\sigma_\beta|u >=& - < d|\sigma_\alpha\sigma_\beta|d >= i \quad \alpha \neq \beta \\ < u|\sigma_\alpha^2|u >=& < d|\sigma_\alpha^2|d >= 1 \quad\quad\quad \alpha = x,y,z \end{aligned} \tag{131}$$

which shows that all the mixed terms in the sum vanish for the unpolarized beam with $P_u = P_d = \frac{1}{2}$ and

$$P_u < u|\sigma_\alpha\sigma_\beta|u > +P_d < d|\sigma_\alpha\sigma_\beta|d >= \delta_{\alpha\beta} \tag{132}$$

Inserting this gives

$$\sum_{\alpha,\beta} \delta_{\alpha\beta} \sum_\lambda P_\lambda < \lambda|B_\alpha(\boldsymbol{r}_1,0)B_\beta(\boldsymbol{r}_2,t)|\lambda >$$

$$= \sum_\alpha \sum_\lambda P_\lambda < \lambda|B_\alpha(\boldsymbol{r}_1,0)B_\alpha(\boldsymbol{r}_2,t)|\lambda >$$

$$= \sum_\lambda P_\lambda < \lambda|\sum_\alpha B_\alpha(\boldsymbol{r}_1,0)B_\alpha(\boldsymbol{r}_2,t)|\lambda >$$

$$= \sum_\lambda P_\lambda < \lambda|\boldsymbol{B}(\boldsymbol{r}_1,0)\cdot\boldsymbol{B}(\boldsymbol{r}_2,t)|\lambda >$$

$$= < \boldsymbol{B}(\boldsymbol{r}_1,0)\cdot\boldsymbol{B}(\boldsymbol{r}_2,t) > \tag{133}$$

The brackets above $<>$ represents the thermal average of the states $|\lambda >$ of the magnetic system in the sample and the probability P_λ is given by

$$P_\lambda = \frac{1}{Z}\exp\left(\frac{-E_\lambda}{k_B T}\right) \tag{134}$$

with Z being the partition function

$$Z = \sum_\lambda \exp\left(\frac{-E_\lambda}{k_B T}\right) \tag{135}$$

In the case of the flux line lattice the thermal average is over all configurations of the flux lines and the weight of the different configurations P_λ depends on the energy of the configurations E_λ compared to the thermal energy $k_B T$.

Finally the magnetic partial differential cross section of any sample is

$$\frac{d^2\sigma}{d\Omega dE'} = \left(\frac{\gamma e}{2h}\right)^2 \frac{1}{2\pi\hbar}\frac{k'}{k}\int\int\int < \boldsymbol{B}(\boldsymbol{r}_1,0)\cdot\boldsymbol{B}(\boldsymbol{r}_2,t) > \exp\{i\boldsymbol{\kappa}\cdot(\boldsymbol{r}_2-\boldsymbol{r}_1)\}\exp\left(-i\omega t\right)d\boldsymbol{r_1}d\boldsymbol{r_2}dt$$
$$\tag{136}$$

By introducing a new coordinate given by $-\boldsymbol{r} = \boldsymbol{r}_2 - \boldsymbol{r}_1$ one gets

$$\frac{d^2\sigma}{d\Omega dE'} = \left(\frac{\gamma e}{2h}\right)^2 \frac{1}{2\pi\hbar}\frac{k'}{k}\int\int G(\boldsymbol{r},t)\exp\left(-i\boldsymbol{\kappa}\cdot\boldsymbol{r} - i\omega t\right)d\boldsymbol{r}dt \tag{137}$$

where $G(\boldsymbol{r},t)$ is the correlation function of the magnetic field

$$G(\boldsymbol{r},t) = \int < \boldsymbol{B}(\boldsymbol{r}_1,0)\cdot\boldsymbol{B}(\boldsymbol{r}_1-\boldsymbol{r},t) > d\boldsymbol{r_1} \tag{138}$$

This formulation is completely general and states that the scattering of any sample with magnetic ordering of spins, free electron orbital motions or flux lines is given by the Fourier transform in space and time of the magnetic field correlation function $G(\boldsymbol{r},t)$.

3.2 Differential Cross section of frozen flux lines

In the following the correlation function formulation above will be applied to a simple model of a flux line lattice consisting of frozen flux lines. The term frozen refers to the assumption that the flux lines do not move due to thermal fluctuations, jumping between pinning sites or the presence of a liquid flux line phase.

This assumption is somewhat justified by the fact that flux lines dissipate energy in the normal core when they are moving and thereby behave like over-damped oscillators with relaxation times of the order 10^{-12} seconds as shown by H. Suhl [26]. Thus it is not very likely to have collective oscillations propagating through the flux line lattice like phonons does in solids. Such excitations has been called 'vortons' by L.N. Bulaevskii *et. al.* [27] in the layered HTc materials.

Due to the assumption of frozen flux lines the time dependence of the correlation function is removed and one can set $t = \infty$

$$G(\boldsymbol{r}) = G(\boldsymbol{r},\infty) = \int < \boldsymbol{B}(\boldsymbol{r}_1,0)\cdot\boldsymbol{B}(\boldsymbol{r}_1-\boldsymbol{r},\infty) > d\boldsymbol{r_1} = \int < \boldsymbol{B}(\boldsymbol{r}_1)\cdot\boldsymbol{B}(\boldsymbol{r}_1-\boldsymbol{r}) > d\boldsymbol{r_1}$$
$$\tag{139}$$

The time integration in the partial differential cross section may then be performed

$$\begin{aligned}
\frac{d^2\sigma}{d\Omega dE'} &= \left(\frac{\gamma e}{2h}\right)^2 \frac{1}{2\pi\hbar}\frac{k'}{k}\int G(\boldsymbol{r})\exp\left(-i\boldsymbol{\kappa}\cdot\boldsymbol{r}\right)d\boldsymbol{r}\int\exp\left(-i\omega t\right)dt \\
&= \left(\frac{\gamma e}{2h}\right)^2 \frac{1}{2\pi\hbar}\frac{k'}{k}\int G(\boldsymbol{r})\exp\left(-i\boldsymbol{\kappa}\cdot\boldsymbol{r}\right)d\boldsymbol{r}2\pi\hbar\delta(\hbar\omega) \\
&= \left(\frac{\gamma e}{2h}\right)^2 \int G(\boldsymbol{r})\exp\left(-i\boldsymbol{\kappa}\cdot\boldsymbol{r}\right)d\boldsymbol{r}\delta(\hbar\omega) \tag{140}
\end{aligned}$$

where the energy difference between the incident and scattered neutron is given by $\hbar\omega = E - E'$ and the δ function in energy transfer shows that the frozen flux line assumption leads to elastic scattering $|k| = |k'|$ where the neutron is not changing its energy in the scattering process.

The differential cross section of elastic scattering on the frozen flux lines may now be obtained by integrating over all energies of the scattered neutron and by noting $d(\hbar\omega) = -dE'$

$$
\begin{aligned}
\frac{d\sigma}{d\Omega} &= \int_0^\infty \frac{d^2\sigma}{d\Omega dE'} dE' \\
&= \int_E^{-\infty} \frac{d^2\sigma}{d\Omega dE'} - d(\hbar\omega) \\
&= \int_{-\infty}^E \frac{d^2\sigma}{d\Omega dE'} d(\hbar\omega) \\
&= \int_{-\infty}^E \left(\frac{\gamma e}{2h}\right)^2 \int G(\boldsymbol{r}) \exp\left(-i\boldsymbol{\kappa}\cdot\boldsymbol{r}\right) d\boldsymbol{r}\,\delta(\hbar\omega) d(\hbar\omega) \\
&= \left(\frac{\gamma e}{2h}\right)^2 \int G(\boldsymbol{r}) \exp\left(-i\boldsymbol{\kappa}\cdot\boldsymbol{r}\right) d\boldsymbol{r} \\
&= \left(\frac{\gamma e}{2h}\right)^2 \mathcal{F}\{G(\boldsymbol{r})\}
\end{aligned}
\tag{141}
$$

Thus the elastic differential cross section of frozen flux lines is given by the Fourier transform $\mathcal{F}$ of the time independent field correlation function.

3.3 Flux line configuration

In general the magnetic field distribution of a flux line configuration can be quite complicated and the superconductor will not act as a linear media at high flux line densities, because the field from two flux lines is not just the vectorial sum of the fields from two isolated flux lines due to the reduction of the order parameter between the two flux lines (see insert of figure 12). However superposition of the field from isolated flux lines is valid at intermediate and low flux line densities where the order parameter reaches its saturation value in between the flux line cores. Thus a configuration of strait flux lines can be expressed as a convolution of the field distribution of a single flux line and a set of δ-functions specifying the position of the flux lines

$$
\begin{aligned}
\boldsymbol{B}(\boldsymbol{r}) &= g(z)\hat{z} \int h(\boldsymbol{r}_{xy} - \boldsymbol{r}'_{xy}) f(\boldsymbol{r}'_{xy}) d\boldsymbol{r}'_{xy} \\
&= g(z)\hat{z}\, h * f
\end{aligned}
\tag{142}
$$

where the function $g(z)$ is a step function specifying the thickness of the sample and thereby the length of the flux lines, $\hat{z}$ is a unit vector along the field direction, $h(\boldsymbol{r}_{xy} - \boldsymbol{r}'_{xy})$ is the field distribution in the xy-plane of an isolated flux line with the core positioned at $\boldsymbol{r}'_{xy}$ and $f(\boldsymbol{r}'_{xy})$ is a sum of δ-functions

$$
f(\boldsymbol{r}'_{xy}) = \sum_i \delta_{2D}(\boldsymbol{r}'_{xy} - \boldsymbol{r}'_{xy,i})
\tag{143}
$$

where $\boldsymbol{r}'_{xy,i}$ specifies the position of i'th flux line.

Now when the field distribution is known the differential cross section can be calculated. First the correlation function is further reduced by noting that the

dot product disappear, since the field only has a z-component, and secondly the thermal average becomes the ground state due to the frozen flux line assumption

$$G(\boldsymbol{r}) = \int B(\boldsymbol{r}_1)B(\boldsymbol{r}_1 - \boldsymbol{r})d\boldsymbol{r}_1 \tag{144}$$

The differential cross section is proportional to the Fourier transform of the correlation function and by applying the convolution theorem (284) of appendix B one gets

$$
\begin{aligned}
\mathcal{F}\{G(\boldsymbol{r})\} &= \mathcal{F}\{B\tilde{*}B\} \\
&= \mathcal{F}\{B\}\mathcal{F}\{B\}^\dagger \\
&= |\mathcal{F}\{B\}|^2
\end{aligned}
\tag{145}
$$

The Fourier transform of the magnetic field given by (142) can be separated into the z and xy component and decomposed by the convolution theorem (280)

$$
\begin{aligned}
\mathcal{F}\{(B)\} &= \mathcal{F}\{g(z)h * f\} \\
&= \mathcal{F}_z\{g(z)\}\mathcal{F}_{2D}\{h * f\} \\
&= \mathcal{F}_z\{g(z)\}\mathcal{F}_{2D}\{h\}\mathcal{F}_{2D}\{f\}
\end{aligned}
\tag{146}
$$

Thus the differential cross section can be written as

$$
\frac{d\sigma}{d\Omega} = \left(\frac{\gamma e}{2h}\right)^2 |\mathcal{F}_z\{g(z)\}|^2 |\mathcal{F}_{2D}\{h\}|^2 |\mathcal{F}_{2D}\{f\}|^2
\tag{147}
$$

which shows that the differential cross section can be written as the product between a factor only depending on the magnetic field distribution of an isolated flux line and a factor only depending on the position of the flux lines. These two factors are denoted the flux line lattice form factor and structure factor in analog to usual scattering theory.

Fourier transform of g(z)

The Fourier transform of the step function g(z) gives

$$
\begin{aligned}
|\mathcal{F}_z\{g(z)\}|^2 &= \left| \int_{z=-\infty}^{\infty} g(z) \exp\left(-i\kappa_z z\right) dz \right|^2 \\
&= \left| \int_{z=-\frac{L}{2}}^{\frac{L}{2}} \exp\left(-i\kappa_z z\right) dz \right|^2 \\
&= \left| \frac{\sin\left(\frac{\kappa_z}{2}L\right)}{\frac{\kappa_z}{2}} \right|^2 \\
&= 2\pi L\delta(\kappa_z)
\end{aligned}
\tag{148}
$$

This shows that the reciprocal lattice of the flux line lattice is two dimensional and scattering can only be obtained when the momentum transfer is zero along the z-axis, $\kappa_z = 0$. The last step in the calculation is shown in appendix B formula (288).

Structure factor

The structure factor can be traced back to be the Fourier transform of a two-dimensional positional correlation function of the form

$$G_p(\boldsymbol{r}_{xy}) = \int f(\boldsymbol{r}'_{xy}) f(\boldsymbol{r}'_{xy} - \boldsymbol{r}_{xy}) d\boldsymbol{r}'_{xy} \tag{149}$$

where f is the sum of δ-functions giving the position of the flux lines as specified by (144). Often the structure factor is given as the double lattice sum

$$
\begin{aligned}
|\mathcal{F}_{2D}\{f\}|^2 &= \left| \sum_i \exp\left(-i\boldsymbol{\kappa}_{xy} \cdot \boldsymbol{r}_{xy,i}\right) \right|^2 \\
&= \sum_{ij} \exp\left(i\boldsymbol{\kappa}_{xy} \cdot (\boldsymbol{r}_{xy,j} - \boldsymbol{r}_{xy,i})\right) \\
&= N \sum_l \exp\left(i\boldsymbol{\kappa}_{xy} \cdot \boldsymbol{l}\right) \\
&= N \frac{(2\pi)^2}{A_u} \sum_{\boldsymbol{\tau}} \delta_{2D}(\boldsymbol{\kappa}_{xy} - \boldsymbol{\tau}) \tag{150}
\end{aligned}
$$

Here N is the number of flux lines in the sample and the last two steps are valid if the flux lines are ordered in a lattice with a unit cell area A_u and reciprocal lattice vectors $\boldsymbol{\tau}$.

Differential cross section of flux line lattice

The differential cross section of a lattice of frozen strait flux lines finally becomes

$$
\begin{aligned}
\frac{d\sigma}{d\Omega} &= \left(\frac{\gamma e}{2h}\right)^2 |\mathcal{F}_z\{g(z)\}|^2 |\mathcal{F}_{2D}\{h\}|^2 |\mathcal{F}_{2D}\{f\}|^2 \\
&= (2\pi)^3 \left(\frac{\gamma}{4\Phi_0}\right)^2 \frac{NL}{A_u} \sum_{\boldsymbol{\tau}} h(\boldsymbol{\kappa})^2 \delta(\boldsymbol{\kappa} - \boldsymbol{\tau}) \tag{151}
\end{aligned}
$$

where γ is the gyromagnetic ratio, $\Phi_0 = \frac{h}{2e}$ is the flux quantum, N the number of flux lines in the sample, L the length of the flux lines which is equivalent to the sample thickness in the direction of the flux lines, A_u the area of the flux line lattice unit cell, $h(\boldsymbol{\kappa})$ is the Fourier transform of the magnetic field distribution of an isolated flux line, $\boldsymbol{\kappa}$ is the momentum transfer in 3 dimensions and $\boldsymbol{\tau}$ are the two dimensional reciprocal lattice vectors of the flux line lattice.

4 Small Angle Neutron Scattering camera

A small angle neutron scattering(SANS) camera is used to obtain structural information about systems with characteristic length scales of the order $d = 10^2 - 10^4$ Å. These length scales are large compared to the wavelength of available neutrons ($\lambda \approx 4$ Å) and a small scattering angle of the order $\theta = \arcsin(\frac{\lambda}{2d}) \approx 0.01 - 1^o$ result from Bragg's law. In order to resolve such small angles a typical SANS camera is between 12-40 meters long and the components are shown on figure 16.
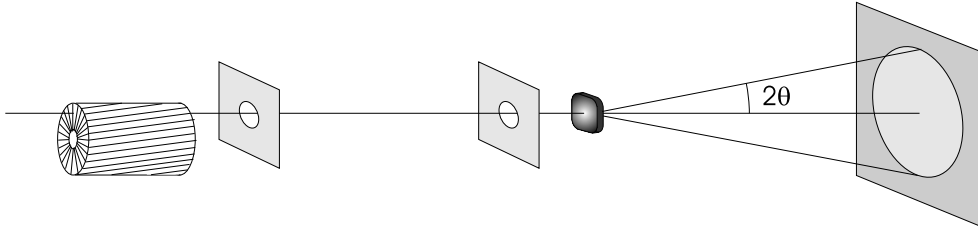

Figure 16. A SANS camera consists of a velocity selector and a collimator section for defining respectively the wavelength and divergence of the incoming neutron beam, which is scattered in the sample and then detected by a 2-dimensional(2D) neutron detector. The collimation is obtained by passing the beam through two pinholes made of neutron absorbing material.

4.1 Single crystal scattering

The scattering condition for any periodic structure can be formulated in reciprocal space by

$$\boldsymbol{\kappa} = \mathbf{k_f} - \mathbf{k_i} = \boldsymbol{\tau} \tag{152}$$

where $\boldsymbol{\kappa}$ is the momentum transfer, $\mathbf{k_i}$ the initial wave vector of the incoming neutron, $\mathbf{k_f}$ the final wave vector of the scattered neutron and $\boldsymbol{\tau}$ denotes a reciprocal lattice vector of the periodic structure in the sample. For elastic scattering with $|k| = |k_f| = |k_i|$ the scattering condition shows that the momentum transfer vector $\boldsymbol{\kappa}$ must be placed on the Ewalds sphere, which is spanned by k_f and k_i as illustrated on figure 17. Thus scattering into the direction of k_f is obtained when the momentum transfer matches a reciprocal lattice vector of the sample.

A typical SANS study of the flux line lattice in a superconductor is performed by placing the superconductor in a cryomagnet at the sample position and collecting the scattered intensity on the detector as the cryomagnet is rotated in small steps in order obtain the scattering condition. The background scattering from the sample due to crystallographic defects is often subtracted from the flux line signal by heating the sample above T_c or applying a field higher than H_{c2}.

4.2 Neutron production

Neutrons for scattering experiments are either produced by fission processes in a reactor or by spallation processes in heavy elements which are bombarded by a high-energy proton beam from an accelerator. The energy of the produced neutrons is of the order MeV and they must be moderated before they can be used for
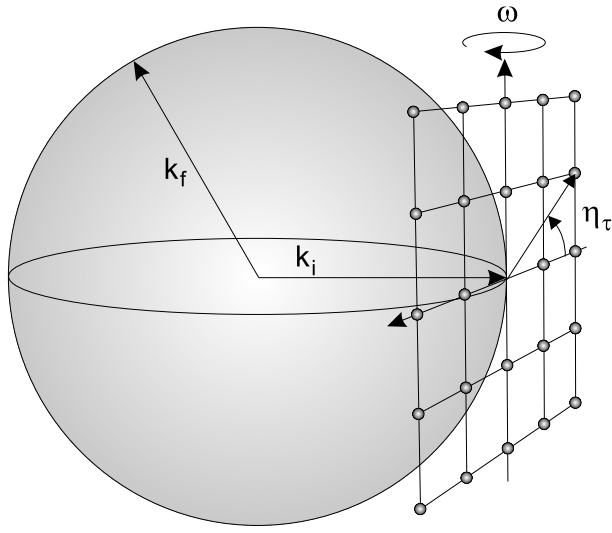
Figure 17. Illustration of the Ewalds sphere defined by $|k_f| = |k_i|$. By placing the center of the two dimensional reciprocal lattice of the flux line lattice at the end point of $\mathbf{k}_i$ the scattering condition $\boldsymbol{\kappa} = \mathbf{k}_f - \mathbf{k}_i = \boldsymbol{\tau}$ becomes equivalent to the condition that the reciprocal lattice points must be on the Ewalds sphere. In order to obtain this condition the reciprocal lattice must be rotated around the vertical axis by the angle ω and the scattered neutrons are collected as function of the rotation angle in a rocking curve. It should be noticed that the lattice vectors τ are orders of magnitude smaller than the size of the Ewalds sphere of a SANS camera.

small angle scattering. This is often done by letting the neutrons diffuse through a container of liquid deuterium, which will thermalize the neutrons at the temperature of the D_2 due to collisions and thereby cause the neutron velocities to approach a Maxwell-Boltzmann distribution. By cooling the deuterium $T_D \approx 20$ K one can obtain low energetic neutrons, which are often called cold and the deuterium container is called a cold source. Figure 18 shows the wavelength spectrum of neutrons from a cold source compared to a room temperature source.
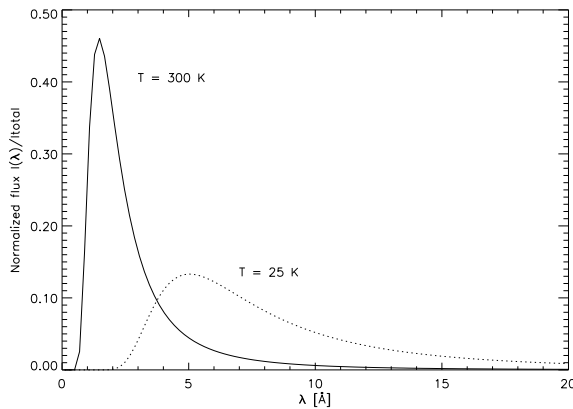

Figure 18. Normalized wavelength spectrum of thermalized neutrons from a source at $T = 25$ K and 300 K. The neutron flux is approximately given by $\phi(\lambda) \propto \lambda^{-3} \exp\left(-\frac{\alpha}{\lambda^2}\right)$, where $\alpha = \frac{h^2}{2mK_BT}$ depends on Planck's constant h, the neutron mass m, the Boltzmann constant K_B and the temperature T. Thus the maximum intensity is found at $\lambda_0 = \frac{h}{\sqrt{3mK_BT}}$.

4.3 Velocity selector

The velocity selector is used to extract a certain wavelength range of the neutrons from the source. This is done by passing the neutrons through tilted blades which are made of neutron absorbing material and mounted on a rotating cylinder. Only the neutrons with a velocity v_n matching the forward movement of the channels between the blades will pass and neutrons moving either faster or slower will be absorbed by the blades.
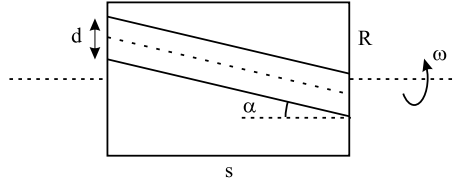

Figure 19. The neutron absorbing blades of the velocity selector are mounted with a distance d and are tilted by an angle α with respect to the rotation axis. Length and radius of the blades are denoted s and R respectively. The incoming neutrons enter the channels between the blades on the left hand side and are absorbed if they move to slow or to fast compared to the movement of the blades.

Figure 19 shows the center position between two blades rotating with a velocity of $R\omega$ and tilted by an angle α with respect to the rotation axis. The displacement l between the entrance and exit opening depends on the time $t = \frac{s}{v_n}$ it takes the neutrons to travel along the blades and the tilt of the blades.

$$l = R\omega t - s\tan(\alpha) \tag{153}$$

Thus the intensity of neutrons with a wavelength $\lambda = \frac{h}{mv_n}$ is proportional to the channel size d with the displacement subtracted

$$I(\lambda) \quad \alpha \quad d - |l| \tag{154}$$

$$= \quad d - \frac{smR\omega}{h}|\lambda - \lambda_0| \tag{155}$$

This is a triangular function with a peak intensity at the wavelength

$$\lambda_0 = \frac{h}{mR\omega}\tan(\alpha) \tag{156}$$

and a relative FWHM value given by

$$\frac{\Delta\lambda}{\lambda_0} = \frac{d}{s\tan(\alpha)} \tag{157}$$

Thus the neutron wavelength is selected by adjusting the rotation speed at a given tilt angle α, which determines the wavelength spread together with the velocity selector geometry. The wavelength spread can be changed by tilting the rotation axis of the velocity selector away from the beam direction by an angle ϕ, whereby an effective tilt angle of $\alpha_e = \alpha + \phi$ must be used in the equation above, which is approximately valid for small ϕ angles.

4.4 Collimation section

Only the neutrons moving in a direction close to the optical axis of the SANS camera can pass the pinholes of the collimation section and this determines the divergence of the neutrons hitting the sample. Often the sample is placed just after the second pinhole which matches the sample size, in order to maximize the ratio between the signal scattered from the sample and the background caused by the direct beam. If the sample is considered to be infinitely small the beam divergence $\Delta\theta_i$ can be estimated simply from the radius r_1 of the first pinhole and the separation L between the two pinholes

$$\Delta\theta_i = \arctan\left(\frac{r_1}{L}\right) \approx \frac{r_1}{L} \qquad r_1 \ll L \tag{158}$$

However a more detailed analysis of the intensity as function of the scattering angle result in a nearly trapezoidal shaped distribution [28]. The intensity is proportional to the overlap between the solid angles of the two pinholes as seen from the detector at a scattering angle $2\theta_i$. A FWHM value $\Delta\theta$ is found from the distribution

$$\begin{array}{ll} \Delta\theta_i = \frac{2r_1}{L} & \text{for} \quad a_1 > a_2 \\ \Delta\theta_i = 2r_2(\frac{1}{L} + \frac{1}{l}) & \text{for} \quad a_1 < a_2 \end{array} \tag{159}$$

where r_1 and r_2 are the radii of the pinholes, L is the distance between the pinholes, l is the distance between pinhole 2 and the detector, and the solid angles of the pinholes at zero scattering angle are denoted $a_1 = \frac{r_1}{L+l}$ and $a_2 = \frac{r_2}{l}$. The trapeziodal distribution becomes nearly a triangular distribution when $a_1 = a_2$ and a box function when a_1 and a_2 are very different.

4.5 Sample environment

The physics of interest is often the sample properties as a function of external variables such as temperature, pressure, magnetic field, stress ect. and therefore a sample table is used to support sample environments like a cryostat, furnace, pressure cell, magnet ect. A typical sample table consist of a XYZ-translation for positioning the sample on the optical axis of the camera, a ω table and a goniometer for rotating and tilting the sample environment with respect the vertical axis. The rotation and tilt are used to scan and align the reciprocal lattice of the sample with respect to the camera as shown on figure 17.

For the flux line lattice studies presented here, different superconducting cryomagnets were used as sample environment giving temperatures down to $T = 1.5$ K and magnetic field up to $H = 5$ Tesla. All crystals were glued onto a Cd mask acting as the second pinhole and mounted inside the cryostats. The final pin-hole of the collimation section was chosen a bit larger than the hole in the Cd mask in order only to illuminate the sample. Sapphire single crystals were used as entrance and exit windows of the cryostats to reduce the small angle background in the experiments.

4.6 2D neutron detector

Neutrons interact weakly with matter which only makes it possible to detect them effectively by an absorption process whereby the neutron is transformed into some detectable particles. Reactions with ^{3}He or ^{10}B in a gas mixture is the most used methods for neutron detection. The absorption reaction for ^{3}He is

$$n + {}^3\text{He} \rightarrow p(0.57\text{MeV}) + {}^3\text{T}(0.20\text{MeV}) \tag{160}$$
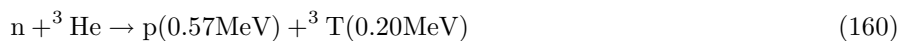
whereby the created proton and Tritium atom will ionize the gas mixture. By placing the gas mixture between an anode and cathode with a high voltage potential difference one can obtain a gas amplification, which will result in a current pulse proportional to the energy of the proton or Tritium. Thus the pulses caused by neutron absorption can be distinguished from pulses created by low energy gamma radiation. However the detected pulse do not carry any information of the energy of the absorbed neutron and therefore the total number of counted neutrons represent an integration over all neutron energies.

A position sensitive detection is obtained by measuring the signal on two sets of wires which are perpendicular to each other. 128 times 128 regions of 5-10 mm in size is often standard resolution for SANS detectors. Thus the data from the camera is a matrix holding the intensity of the pixels indexed by their horizontal and vertical position on the detector.

5 Data analysis

In this chapter the momentum transfer is determined from the detector intensity distribution and the resolution of the SANS camera is estimated in momentum transfer space by assuming that the neutrons are scattered in the sample without any energy exchange. Finally the integrated intensity is calculated from the differential scattering cross section of a given sample.

5.1 Momentum transfer

Figure 20 shows how the scattering geometry of the SANS camera can be used to relate a detector pixel to a corresponding momentum transfer vector. The direction of the incoming neutron $\mathbf{k_i}$ is assumed to be along the optical axis denoted z and the scattered neutron $\mathbf{k_f}$ leaves the sample in a direction given by the angles θ_f and ϕ_f. By assuming elastic scattering ($|k_i| = |k_f| = k$) the momentum transfer reads

$$\kappa = \mathbf{k_f} - \mathbf{k_i} \tag{161}$$

$$= k \begin{pmatrix} \sin\theta_f \cos\phi_f - 0 \\ \sin\theta_f \sin\phi_f - 0 \\ \cos\theta_f - 1 \end{pmatrix} \tag{162}$$
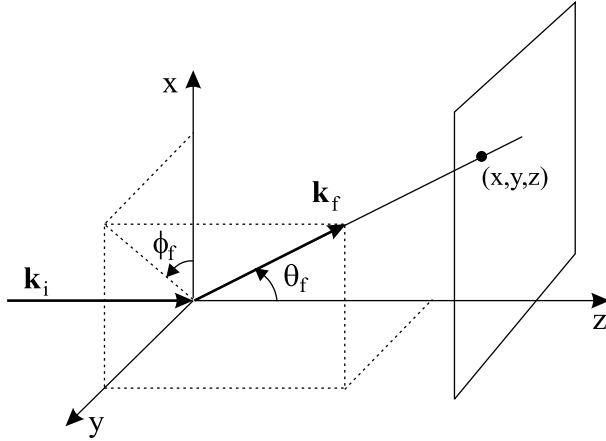

Figure 20. Scattering geometry of the SANS camera where the incoming neutron wave vector $\mathbf{k_i}$ is scattered into $\mathbf{k_f}$ which is observed in the coordinate (x,y,z) on the 2D detector placed a distance z from the sample which is at origo. The direction of $\mathbf{k_f}$ is given by the angles θ_f and ϕ_f, which can be found from the detector coordinate (x,y,z).

By placing the detector a distance z from the sample one can determine the direction of the scattered neutron from the position (x, y) where it was absorbed in the detector

$$\begin{array}{ll} \sin\theta_f = \frac{\sqrt{x^2+y^2}}{\sqrt{x^2+y^2+z^2}} & \cos\theta_f = \frac{z}{\sqrt{x^2+y^2+z^2}} \\ \sin\phi_f = \frac{y}{\sqrt{x^2+y^2}} & \cos\phi_f = \frac{x}{\sqrt{x^2+y^2}} \end{array} \tag{163}$$

whereby the momentum transfer is given by the detector coordinates (x, y, z) and the neutron wavelength $k = \frac{2\pi}{\lambda}$ as

$$\kappa_x = k\frac{x}{\sqrt{x^2+y^2+z^2}} \approx k\frac{x}{z}$$

$$\kappa_y = k\frac{y}{\sqrt{x^2+y^2+z^2}} \approx k\frac{y}{z}$$

$$\kappa_z = k\left(\frac{z}{\sqrt{x^2+y^2+z^2}} - 1\right) \approx 0 \qquad (164)$$

The last expressions are approximations valid in the small angle limit with $x, y \ll z$.

5.2 Resolution function

The transformation from detector position into momentum transfer space given by (164) is based on the assumption that all incoming neutrons are directed along z and have the same wavelength λ. However the distribution of the wavelength and the incoming angles caused by the velocity selector and the collimation section will make it possible for different incoming neutrons to be scattered into the same detector position. One should think of the distribution of wave lengths and direction as resulting in a distribution of Ewalds spheres with different radia and positions of the centers instead of just one sphere as shown on figure 17. Thus the measured signal I at (x, y, z) is an integration of the differential scattering cross section $\frac{d\sigma}{d\Omega}$ of the sample and the resolution function R_κ describing the available neutrons of the camera

$$I(<\boldsymbol{\kappa}>) = \int R_\kappa(\boldsymbol{\kappa}, <\boldsymbol{\kappa}>)\frac{d\sigma}{d\Omega}(\boldsymbol{\kappa})d\boldsymbol{\kappa} \qquad (165)$$

The nominal momentum transfer $<\boldsymbol{\kappa}>$ is defined from equation (164) by inserting the wavelength λ_0 of the maximum intensity of the incoming beam. Thus the resolution function $R_\kappa(\boldsymbol{\kappa}, <\boldsymbol{\kappa}>)$ describes the distribution of neutrons with a momentum transfer $\boldsymbol{\kappa}$ which can be scattered into the a detector position corresponding to the nominal $<\boldsymbol{\kappa}>$ vector.

Appendix A gives an approximative expression for the SANS resolution function for scattering into a single detector pixel specified by the angle θ_f as illustrated on figure 21. All scattering vectors τ of the sample, which are placed within the resolution ellipse will contribute to the intensity detected in the pixel, and the weights of the contributions are determined by the gaussian resolution function given by

$$R(\kappa_q, <\kappa_q>) = \frac{1}{\sqrt{2\pi}\sigma_{||}\sigma_\perp\sigma_\phi}\exp\left\{-\frac{1}{2}\left(\frac{(\kappa_{q||} - <\kappa_q>)^2}{\sigma_{||}^2} + \frac{\kappa_{q\perp}^2}{\sigma_\perp^2} + \frac{\kappa_{q\phi}^2}{\sigma_\phi^2}\right)\right\} \qquad (166)$$

Here the momentum transfer vector κ_q is described in a local coordinate system with $\kappa_{q||}$ directed along the nominal momentum transfer $<\boldsymbol{\kappa}>$ and perpendicular to this are $\kappa_{q\perp}$ and $\kappa_{q\phi}$ respectively in and out of the scattering plane. The corresponding widths are in the small angle limit $\theta_f \approx 1^o$ given by
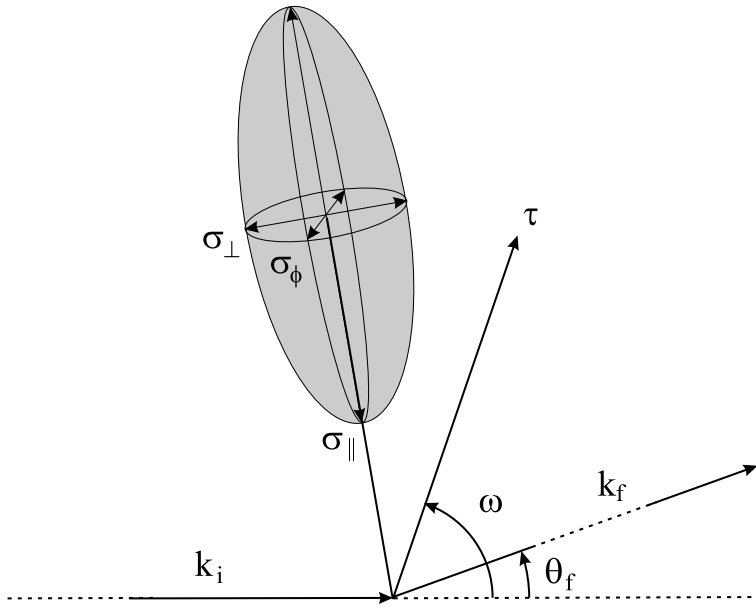
Figure 21. Gaussian resolution function for scattering into the detector pixel corresponding to the nominal momentum transfer $< \kappa >$ at the center of the distribution. The shape of the distribution is given by the longitudinal width $\sigma_{||}$, the transverse width $\sigma_\perp$ and the azimuthal width σ_ϕ. τ is a scattering vector of the sample and will only give scattering in the detector pixel when it is moved inside the resolution ellipse by changing the angle ω during a rocking curve.

$$\sigma_{||}^2 \quad = \quad k_0^2 \left\{ \left(\frac{< \kappa_q >}{2\pi} \sigma_\lambda \right)^2 + \left(\sigma_{\theta_f}^2 + \sigma_{\theta_i}^2 \right) \right\} \tag{167}$$

$$\sigma_\perp^2 \quad = \quad \frac{< \kappa_q >^2}{4} \left(\sigma_{\theta_f}^2 + \sigma_{\theta_i}^2 \right) \tag{168}$$

$$\sigma_\phi^2 \quad = \quad k_0^2 (\sigma_{\phi_f}^2 + \sigma_{\phi_i}^2) \tag{169}$$

and are denoted the longitudinal, transverse and azimuthal width. Here the neutron wavevector is $k_0 = \frac{2\pi}{\lambda_0}$. The width of the wavelength distribution σ_λ, the incoming angles σ_{θ_i} and scattered angles σ_{θ_f} are determined by the wavelength spread $\frac{\Delta\lambda}{\lambda}$ of the velocity selector, the collimation $\Delta\theta_i$ set by the pin-hole configuration and the detector resolution given by the pixel size Δr and the position of the detector z.

$$\sigma_\lambda \quad = \quad \frac{\lambda_0}{2\sqrt{2ln2}} \frac{\Delta\lambda}{\lambda_0} \tag{170}$$

$$\sigma_{\theta_i} \quad = \quad \frac{1}{2\sqrt{2ln2}} \Delta\theta_i \tag{171}$$

$$\sigma_{\theta_f} \quad = \quad \frac{1}{2\sqrt{2ln2}} \frac{\Delta r}{z} \tag{172}$$

The gaussian approximation derived here is only suited for giving a qualitative understanding of the resolution function since it is formulated in a local coordinate system, which is not giving the intensity distribution on the detector directly. For a single scattering vector τ the intensity distribution on the detector will however have a close similarity to the resolution ellipse, since ellipses of neighboring detector pixels overlap. Thus the scattering from τ is expected to result in a gaussian

intensity distribution on the detector and the width of this distribution on the detector is approximately given by the expression in (167). It should be noticed that the transverse resolution $\sigma_\perp$ is orders of magnitude better that the longitudinal $\sigma_\|$ and azimuthal resolution σ_ϕ, since it is proportional with the scattering vector $< \kappa_q >$ instead of the neutron wave vector k_0. P. Harris [29] has carried out a much more detailed analysis of the resolution function of a Laue camera and her main result is a global gaussian resolution function, which can be used to convolute a fitting function of the differential cross section. Here the data will be analyzed by calculating the integrated intensity of the flux line lattice.

5.3   Integrated intensity

The integrated intensity of a single crystal reflection refers to the total number of neutrons scattered by a reciprocal lattice vector τ as this vector is rocked through the Ewalds sphere. It is found by first integrating the differential cross section over all solid angles for a given rocking angle ψ and then integrating the cross section over the rocking angle of the rocking curve. This calculation has been carried out in Squires [25] p. 41 and by Eskildsen [8] p. 25 and only the main steps are shown here.

The first step is written as

$$\sigma_{tot}(\psi) = \int_{Alldir} \frac{d\sigma}{d\Omega} d\Omega = \left| \frac{d\sigma}{d\Omega} \right| \int_{Alldir} \delta_{3D}(\boldsymbol{\kappa} - \boldsymbol{\tau}) d\Omega \tag{173}$$

where the differential cross section is separated into the magnitude $\left| \frac{d\sigma}{d\Omega} \right|$ and the δ - function in reciprocal space, which is related to the rocking angle ψ. The second step is to integrate the cross section over the rocking angle ψ

$$P = \phi \int_{\psi=0}^{\pi} \sigma_{tot}(\psi) d\psi \tag{174}$$

where ϕ is the neutron flux hitting the sample. The result of the calculation is that the magnitude of the differential cross section $\left| \frac{d\sigma}{d\Omega} \right|$ must be multiplied by a factor

$$P = \left| \frac{d\sigma}{d\Omega} \right| \frac{\phi}{k^2 \tau \cos(\eta_\tau)} = \left| \frac{d\sigma}{d\Omega} \right| \frac{\lambda_n^2 \phi}{(2\pi)^2 \tau \cos(\eta_\tau)} \tag{175}$$

which depend on the size of the Ewalds sphere set by the neutron wavelength λ_n and how fast the reciprocal lattice vector τ is rotated through the Ewalds sphere, which depend on the length of the reciprocal lattice vector and the angle η_τ between the lattice point and the rotation axis as shown on figure 17. Lattice points on the rotation axis will not rock and will always be on the Ewalds sphere whereby the integrated intensity becomes infinite.

The reflectivity R of a scattering vector is defined as the ratio between the total number of neutrons scattered per second P and the number of neutrons hitting the sample per second given by the product of the incident neutron flux ϕ and the illuminated sample area A_s

$$R = \frac{P}{\phi A_s} = \frac{scattered\,neutrons}{incident\,neutrons} \tag{176}$$

The reflectivity of the flux line lattice can now be found from the differential cross section given by (151)

$$R_{FLL} = \frac{\lambda_n^2}{(2\pi)^2 \tau \cos(\eta_\tau) A_s}(2\pi)^3 \left(\frac{\gamma}{4\Phi_0}\right)^2 \frac{NL}{A_u}h(\boldsymbol{\tau})^2$$

$$= 2\pi \left(\frac{\gamma}{4\Phi_0}\right)^2 \frac{L}{A_u^2}\frac{\lambda_n^2}{\tau \cos(\eta_\tau)}h(\boldsymbol{\tau})^2 \tag{177}$$

where γ is the gyromagnetic ratio, Φ_0 is the flux quantum, L is the sample thickness or length of the flux lines, A_u is the area of the flux line lattice unit cell, λ_n is the neutron wavelength, τ is the length of the scattering vector, n_τ is the angle between the scattering vector and the rotation axis as shown on figure 17 and $h(\boldsymbol{\tau})$ is the form factor of a flux line, which is given by the Fourier transform of the field distribution of an isolated flux line.

5.4   Experimental determination of reflectivity

Figure 22 shows the diffraction pattern from the flux line lattice in $TmNi_2B_2C$ when all the images of a rocking curve with the rotation axis vertical are summed into one image. The diffraction spots have an elliptical shape as expected from the resolution function analysis, but the major axis of these ellipses are not pointing towards the center of the detector, because the illuminated sample area is rectangular (4.5 mm x 6.0 mm) and result in a different beam divergence in the vertical and horizontal plane of the SANS camera. An estimate of the spot size from the camera settings is outlined in the figure text.

The rocking curve of the (10) flux line lattice reflection is constructed by integrating the intensity inside a box surrounding the diffraction spot and plotting this as function of the rock angle as shown on figure 23. Then the integrated intensity becomes the area under the rocking curve divided by the counting time in each point, but this is only valid if the neutron flux is constant in time, which is not fulfilled when the neutron source is fluctuating like a spallation source. Instead an almost transparent neutron detector called a monitor is inserted in the direct beam after the velocity selector and it will detect a small fraction of the beam hitting the sample, whereby the total monitor count will be proportional to the total number of neutrons hitting the sample. The scaling can be determined by inserting an attenuator in the direct beam and removing the beamstop sitting in front of the center of the detector to protect it from the direct beam. Thus the monitor scaling f_{mon} is defined as the ratio between the number of neutrons counted by the monitor and the number of neutrons in the direct beam counted with the detector when the beamstop is removed.

$$f_{mon} = \frac{N_{monitor}}{N_{Direct\,beam}} \tag{178}$$

Using this the reflectivity may be rewritten

$$R = \frac{P}{\phi A_s} = \frac{\int \frac{I(\psi)}{\Delta t}d\psi}{\frac{N_{sample}}{\Delta t}}$$

$$= \frac{\int I(\psi)d\psi}{N_{sample}}$$

$$= \frac{f_{mon}}{N_{monitor}}\int I(\psi)d\psi \tag{179}$$

where the integral is the area under the rocking curve and $I(\psi)$ is the number of neutrons counted at the angle ψ when counting $N_{monitor}$ neutrons in the monitor.
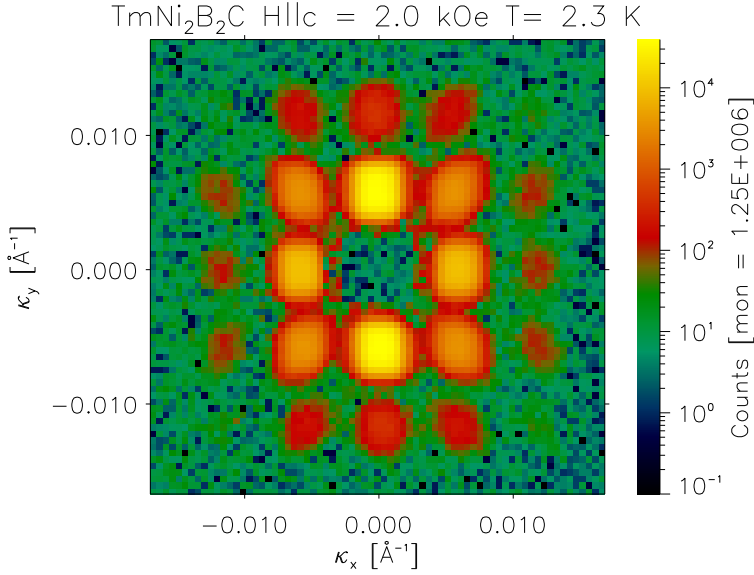
TmNi$_2$B$_2$C H||c = 2.0 kOe T= 2.3 K

Figure 22. Diffraction pattern of the flux line lattice in $TmNi_2B_2C$ cooled to $T = 2.3$ K in an applied field of $H = 2.0$ kOe along the crystalline c-axis and with the crystallographic [110] axis in the horizontal and vertical plane of the SANS camera. The image shows the summation of a series of images in a rocking curve obtained by rotating the lattice around the vertical direction. A series of background images without flux lines at $T = 12.3K > T_c = 11.5K$ has been subtracted from the data. The settings of the SANS camera was $\lambda_n = 5\,\AA$, $\frac{\Delta\lambda}{\lambda} = 0.10$, pinhole1 = 5.0 cm × 5.0 cm, pinhole2 = 4.5 mm × 6.0 mm, collimation $L = 18$ m and detector distance $l = 19.75$ m. If the sample pinhole is approximated as circular of a size 5 mm one gets an estimate of the longitudinal and azimuthal resolution of $\sigma_{||} = 1.51{\cdot}10^{-3}\,\AA^{-1}$ and $\sigma_\perp = 1.49{\cdot}10^{-3}\,\AA^{-1}$ in some agreement with experimental values $\sigma_{||,exp} = 8.2 \pm 0.2 \cdot 10^{-4}\,\AA^{-1}$ and $\sigma_{\perp,exp} = 1.0 \pm 0.02 \cdot 10^{-3}\,\AA^{-1}$ found by fitting a 2D gaussian to the (10) spots of the flux line lattice.

It should be noticed that N_{sample} is the number of neutrons which has passed the sample, whereby the sample absorption has been included in the calculation. The situation where neutrons are scattered in the front part of the crystal and damped along the path through the crystal is equivalent to damping the incident beam through the crystal and scattering near the backside.

There will be a difference in neutron flux on the front side I_0 and backside I_1 of the sample due to the absorption

$$I_1 = I_0 \exp\left(-\gamma t\right) \tag{180}$$

where t is the sample thickness and the absorption coefficient γ depend on the tabulated [12] absorption cross sections σ_{abs} of the atoms in the crystalline unit cell of volume V_{uc} and the neutron wavelength λ_n

$$\gamma(\lambda_n) = \frac{\sum_{uc}\sigma_{abs}}{V_{uc}}\frac{\lambda_n[\AA]}{1.8\,\AA} \tag{181}$$

By introducing a monitor efficiency as $N_{monitor} = \xi_{mon}I_0$ it is seen that the monitor scaling

---

[12]See Shirane [30] appendix 1

$$f_{mon} = \frac{N_{monitor}}{N_{Direct\,beam}} = \frac{\xi_{mon}I_0}{I_1} = \xi_{mon}\exp{(\gamma t)} \tag{182}$$

will depend on the sample thickness, the absorption coefficient of the sample and on the neutron wavelength. Thus the monitor scaling must be determined as function of wavelengths in each experiment.

Thus the reflectivity provides an absolute scale for comparison of the cross section of scattering from the flux line lattice as determined from varies models.
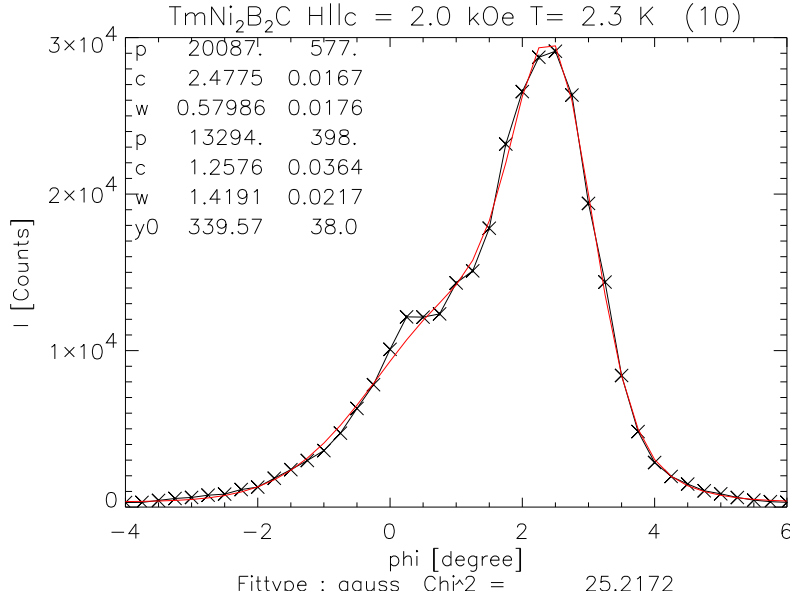

Figure 23. Rocking curve of the (10) FLL reflection in $TmNi_2B_2C$ determined by integrating the intensity in a box surrounding the diffraction spot on figure 22. The asymmetric shape of this rocking curve indicate that the sample consists of several single crystals, which is probably connected to the fact that borocarbides grow in platelets with the c-axis normal to the plate. A fit by 2 gaussians $f(x) = p\exp{\left(-\frac{(x-c)^2}{2w^2}\right)} + y_0$ describes the observed intensity fairly well and the width of the peaks are $w_1 = 0.58^o$ and $w_2 = 1.42^o$. An estimate of the transverse resolution gives $\sigma_\perp = 3.7 \cdot 10^{-6} \, \mathring{A}^{-1}$ and the corresponding angular resolution of the rocking curve will be approximately $w = \frac{\sigma_\perp}{\tau} = 0.03^o$ showing that the observed rocking curve is broad compared to the resolution.

5.5 Optimal sample thickness

There exist an optimal sample thickness in a flux line lattice SANS experiment since the scattered intensity from the flux lines is proportional to the sample thickness t, but the absorption depends exponentially on the sample thickness. The scattered intensity becomes

$$I_{FLL}(t) \propto t\exp{(-\gamma t)} \tag{183}$$

which has a maximum at

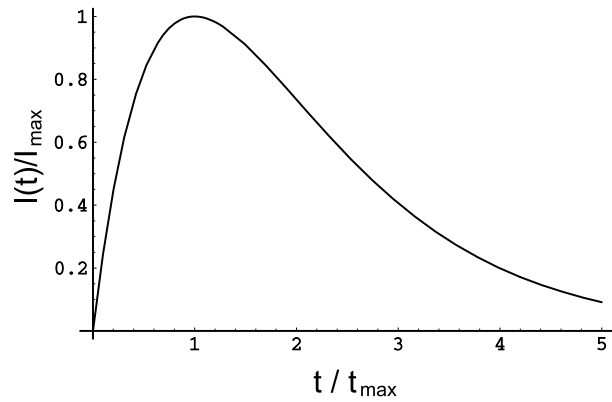$$t_{max} = \frac{1}{\gamma} \tag{184}$$

as shown on figure 24.

Figure 24. Scattered intensity $I \propto t \exp\left(-\gamma t\right)$ from the flux line lattice in a sample of thickness t and with an absorption coefficient γ, which causes the optimal sample thickness $t_{max} = \frac{1}{\gamma}$. For $TmNi_2B_2C$ one gets $\gamma = 1.68\,cm^{-1}$ at $\lambda_n = 1.8\,\mathring{A}$ and $t_{max} = 2.1\,mm$ at $\lambda_n = 5\,\mathring{A}$. The average thickness of the sample giving the scattering in figure 22 is approximately 0.7 mm, which is close to t_{max}.

6 Borocarbide superconductors

The borocarbides RNi_2B_2C (R = Y, rare earth La-Lu) has been studied intensively since the discovery in 1994 [2], because these compounds exhibits superconductivity when R = Dy-Tm, Lu, Y and magnetic ordering for R = Pr-Tm. Superconductivity co-exist with the magnetic ordering in the case of R = Dy-Tm [1].

6.1 Structure

Figure 25 show the tetragonal crystal structure of RNi_2B_2C (R-1221) which consist of Ni_2B_2 layers separated by RC planes [3]. The site R can be occupied by the rare-earth atoms ranging from La-Lu, since the gradual filling of the 4f electronic shell in the series only changes the chemical bonding of the outermost $6s^2$ electrons slightly. A linear variation of the lattice parameters is seen as the ionic radius is changing in the series and typical values for the superconducting compounds are $a = b = 3.46 - 3.53$ Å and $c = 10.49 - 10.63$ Å [5].

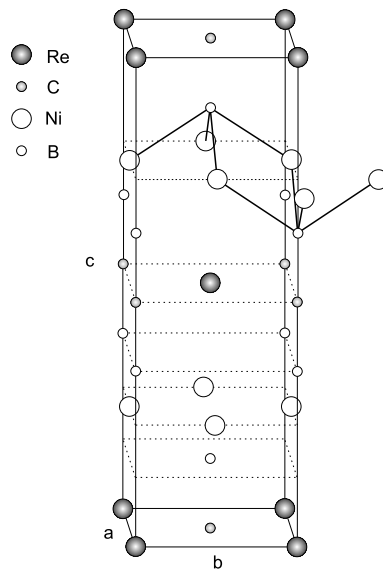*Figure 25. Tetragonal unit cell I4/mmm of the borocarbides* RNi_2B_2C *where the rare earth atoms La-Lu and Y can occupy the R site. Typical lattice parameters are* $a = b = 3.46 - 3.53Å$ *and* $c = 10.49 - 10.53$ Å, *and the tetrahedrally coordination of Ni in the* Ni_2B_2 *layers has been emphazised by solid lines in the top part of the figure.*

6.2 Fermi surface

Band structure calculations have been performed on the borocarbides and the obtained electronic structures are quite complicated [31, 32, 33]. Several bands crosses the Fermi level and the resulting Fermi surface separate into 3 sheets experimentally confirmed by Dugdale *et. al.* [33] on R = Lu. These sheets have a 3 dimensional character and the resulting normal state is metallic with almost isotropic conductivity [34].

6.3 Superconductivity

Borocarbides are considered as BCS superconductors with phonon mediated coupling of the Cooper pairs and the density of state at the Fermi level is dominated by the Ni orbitals [31]. All superconducting R-1221 are of the second type with $\kappa > \frac{1}{\sqrt{2}}$ and critical temperatures and fields are in the range $T_c = 6 - 16.1$ K and $H_{c2} = 5 - 90$ kOe as showed on figure 26 and listed in table 1.
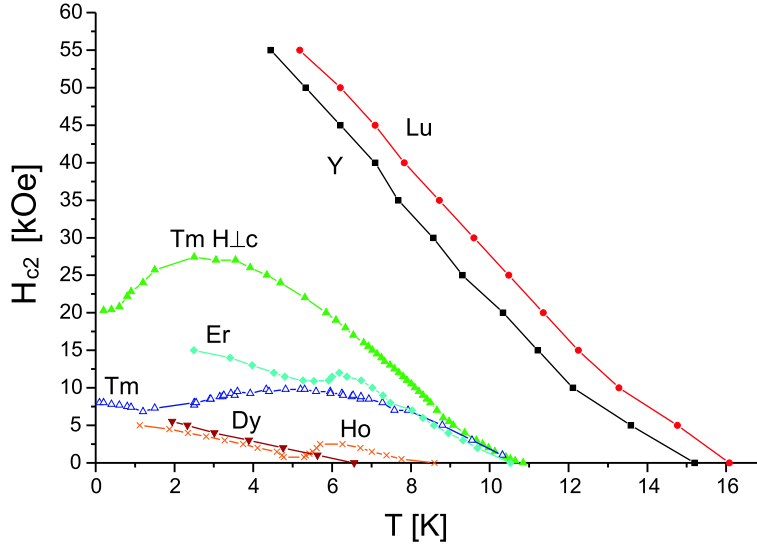

Figure 26. Upper critical fields H_{c2} for $H||c$ of the superconducting RNi_2B_2C borocarbides based on [35, 36, 37, 38, 39, 40]. H_{c2} extends almost linearly to approximately 90 kOe for the non-magnetic members $R = Y$, Lu and the suppression of both H_{c2} and T_c of the magnetic members is caused by Cooper pair-breaking due to the magnetic moment of the rare earth atoms. Features in the curves for the magnetic members are connected to onset or changes in the magnetic order. For $R = Tm$ both the in- and out of plane H_{c2} curve is showed illustrating the influence of the susceptibility of the magnetic atoms.

The relative high T_c value of the non-magnetic members can qualitatively be understood from the BCS relation (2)

$$T_c = 1.14 \Theta_D e^{-\frac{1}{N(0)V}} \tag{185}$$

where the Debye temperature $k_B \Theta_D = \hbar \omega_D$ of the phonons has been introduced. Specific heat measurements [13] gives $\Theta_D = 464$ K for $R = Y$ whereby the product $N(0)V = 0.28$ is found. This shows that the weak coupling limit $N(0)V \ll 1$ of the BCS theory is not well satisfied indicating that the borocarbides are moderately strong coupled superconductors, which is supported by band structure calculations [32].

An estimate of the gap in $R = Y$ can be obtained from $T_c = 15.5$ K giving $\Delta_{BCS} = 1.76 k_B T_c \sim 2.4$ meV with some agrement to STM measurements giving $\Delta = 2.2$ meV [42] and $\Delta = 1.8$ meV [43].

The almost linear temperature dependence of the upper critical field for the non-magnetic members is deviating from the BCS theory predicting the thermodynamic critical field H_c to be approximately given by [14]

---

[13]H. Michor *et. al.* [41]

[14]Schrieffer [14] p. 56

$$H_c(T) \approx H_c(0) \left[1 - \left(\frac{T}{T_c} \right)^2 \right] \tag{186}$$

which is proportional to the upper critical field $H_{c2} = \sqrt{2}\kappa H_c$ in the GL theory (64).

Several explanations have been suggested in the literature such as coupling between superconductivity on different Fermi surface sheets (two-band model), non-local extension of the GL model, an order parameter of d-wave symmetry and pair breaking by magnetic correlations [36]. Generally the superconducting gap in the nonmagnetic borocarbides should be considered to have anisotropic s-wave symmetry, while the anisotropy of the characteristic length scales in table 1 mainly result from the Fermi velocity distribution on the Fermi surface. It should be noted that the coherence length is considerable larger than the size of the crystallographic unit cell indicating a 3 dimensional character of the superconducting state.

R	T_c[K]	T_N[K]	$\xi_{c,ab}$ [Å]	$\lambda_{c,ab}$ [Å]	$\kappa_{c,ab}$	q_{mag}	μ_{Dir}	Ref.
Y	15.6	-	64, 64	1207, 1207	17,17	-	-	[35]
Lu	16.1	-	46, 60	1010, 690	16.0, 11.6	-	-	[36]
Tm	11.0	1.5	124,110	780,850	6.3,7,7	$0.093(a^* + b^*)$	(001)	[44, 5]
Er	10.5	6.0	131,150	1160	8.8	$0.55\ a^*$	(100)	[38, 44, 5]
Ho	8.7	6.0	280			$0.915\ c^*$	Spiral	[39]
		5.5				$0.55\ a^*$	b^*	[45, 46]
		5.2				$1.0\ c^*$	(110)	
Dy	6.2	10.3			3.0	$1.0\ c^*$	(110)	[47, 48, 5]

Table 1. Characteristic parameters of the superconducting borocarbides RNi_2B_2C in terms of critical temperature T_c, Magnetic ordering temperature T_N, coherence length ξ, penetration depth λ, Ginzberg-Landau κ, ordering vector q_{mag} of magnetic phases and the direction of the magnetic moments.

6.4   Magnetism

Rare earth atoms have a magnetic moment due to the partial filled 4f electronic shell, but the separation between the rare earth atoms in the borocarbides is too large to have any effective direct exchange interaction. However the local magnetic moment will polarize the conduction electrons of the metal and these electrons can thereby mediate an indirect coupling known as the Ruderman-Kittel-Kasuya-Yosida(RKKY) interaction. The polarization disturbance created by the local moment is screened by the conduction electrons resulting in a periodically changing polarization decaying away from the local moment. This effect is similar to Friedel oscillations in a free electron gas due to a charge disturbance [15] and is described by the non-local susceptibility $\bar{\bar{\chi}}(r - r')$ of the conduction electrons. The Hamiltonian of the indirect interaction between two local moments $\boldsymbol{J}_{i,j}$ sitting at $\boldsymbol{R}_{i,j}$ can be written as [16]

$$\mathcal{H}_{ij} \sim \int \int I(r - \boldsymbol{R}_j)(g-1)\boldsymbol{J}_j(\boldsymbol{R}_j)\chi(r - r')I(r' - \boldsymbol{R}_i)(g-1)\boldsymbol{J}_i(\boldsymbol{R}_i)dr dr' \tag{187}$$

where the function $I(r - \boldsymbol{R}_j)$ describes the overlap between the 4f and the conduction electrons of the atom at $\boldsymbol{R}_j$, g is the Landé factor connected to addition

---

[15] See Ashcroft/Mermin [49] p. 343
[16] J. Jensen [50] chap. 1.4

of orbital $\boldsymbol{L}$ and spin moment $\boldsymbol{S}$ into the total angular moment $\boldsymbol{L}+2\boldsymbol{S} = g\boldsymbol{J}$ found from Hund's rule. When summing over all moments the total Hamiltonian is more conveniently written as

$$\mathcal{H} \sim -\sum_{\boldsymbol{q}} \mathcal{J}(\boldsymbol{q})\boldsymbol{J}(\boldsymbol{q})\boldsymbol{J}(-\boldsymbol{q}) \tag{188}$$

with the Fourier transform of the magnetic structure given by

$$\boldsymbol{J}(\boldsymbol{q}) = \frac{1}{N}\sum_{i} \boldsymbol{J}_i e^{-i\boldsymbol{q}\cdot\boldsymbol{R}_i} \tag{189}$$

and the interaction term

$$\mathcal{J}(\boldsymbol{q}) \sim (g-1)^2 |I(\boldsymbol{q})|^2 \chi(\boldsymbol{q}) \tag{190}$$

This shows that a magnetic structure with a $\boldsymbol{q}$ value corresponding to the maximum of the interaction function $\mathcal{J}(\boldsymbol{q})$ will be favored by the indirect interaction. The resulting ordering of the rare earth moments is in the form of a spin density wave, where the time average of the rare earth moments attains a fixed orientation and a finite value changing periodically in space. Crystal field effects and the specific electronic band structure has a large influence on direction and periodicity of the spin density wave.

Thermal fluctuations destroys the magnetic order at the Néel temperature T_N which is proportional to the Hamilton above

$$T_N \quad \sim \quad \frac{\mathcal{J}(\boldsymbol{q})J(J+1)}{K_B}$$

$$\sim \quad \frac{|I(\boldsymbol{q})|^2\chi(\boldsymbol{q})}{K_B}(g-1)^2 J(J+1) \tag{191}$$

Thus if the pre-factor describing the electronic system is assumed constant in the borocarbide series it is seen that the magnetic ordering temperature should scale with the deGennes factor $dG = (g-1)^2 J(J+1)$ describing the magnitude of the Hund's rule moment. This explains the increasing T_N of the magnetic borocarbides listed in table 1.

The most common spin density wave observed in the borocarbides is directed along the crystalline a(or b) axis, have the moment along b (or a) and a periodicity of $q \approx 0.55a^*$ (or $q \approx 0.55b^*$), with a^* being the reciprocal unit vector $a^* = \frac{2\pi}{a}$. Figure 27 illustrates the spin density wave along the crystalline a axes. This wave is in-commensurate with the atomic lattice, but quite close to simply antiferromagnetic ordering which would have $q = 0.5a^*$ and cause neighboring atoms to have moments of equal magnitude but alternating direction. Band structures for $R = Lu$ has been used to evaluate the electronic susceptibility given by[51]

$$\chi(\boldsymbol{q}) = \sum_{n,m,\boldsymbol{k}} \frac{f[\epsilon_m(\boldsymbol{k})]\{1 - f[\epsilon_n(\boldsymbol{k}+\boldsymbol{q})]\}}{\epsilon_n(\boldsymbol{k}+\boldsymbol{q}) - \epsilon_m(\boldsymbol{k})} \tag{192}$$

where $f(\epsilon)$ is the Fermi-Dirac occupation function. Large contributions to the sum is obtained for pairs of occupied and empty states which are separated by a wave-vector $\boldsymbol{q}$ and have almost the same energy. This is obtained for states close to the Fermi surface and the $q = 0.55a^*$ magnetic phase has been explained from the existence of parallel parts of the Fermi surface causing nesting and a peak in the susceptibility [33]. The periodicity and direction of the magnetic moments observed in the magnetic superconductors are listed in table1.
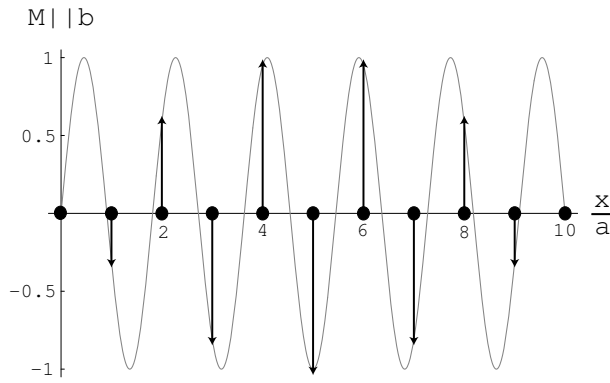
Figure 27. Spin density wave of the rare earth moments directed along the b axis and changing periodically along the a axis with a periodicity $q = 0.55a^*$. The moments are modulated as $M(x) = M_0 \sin(qx)$ with $x = na$ giving the positions of the rare earth atoms along a indicated by solid dots.

6.5 Interaction between superconductivity and magnetism

Both the RKKY magnetism and the superconducting ground state are based on the many-body interaction of the conduction electrons and one might expect the two ground states to exclude one another. A hand-waving argument for the co-existence is that the coherence length is much larger than the period of the spin density wave, whereby the magnetic field averaged over the coherence length is practically zero.

In the previous discussion of the upper critical field H_{c2} the suppression of the superconducting order parameter has been cause by the acceleration of the Cooper pairs, which break up when the kinetic energy exceeds the superconducting gap. This is called the orbital effect, but a magnetic field can directly break the Cooper pair, because the zeeman effect will shift the energy of the spin up and spin down electron in the Cooper pair in opposite directions as pointed out by Clogston [52].

The presence of a localized magnetic moment will cause a similar Zeeman splitting of the energy of the spin up and spin down electron and the resulting spin flipping can break the Cooper pairs and cause a reduction of the superconducting order parameter. This spin flip breaking of the Cooper pairs will scale with the magnitude of the localized moment and De Gennes [15, 4] has shown that the critical temperature T_c will be suppressed by the deGennes factor $dG = (g-1)^2 J(J+1)$ introduced in the previous section. Thus the increasing magnetic ordering temperature of the different borocarbides result in a decreasing critical temperature of the superconducting phase in agreement with the deGennes scaling for the pure compounds as reported by Canfield *et. al.* [53]

7 Flux line lattice in borocarbides

Shortly after the discovery of the borocarbides a square flux line lattice induced by an applied field along the crystalline c-axis was observed in $ErNi_2B_2C$ using SANS [6]. Later experiments revealed a field induced transition from a hexagonal to a square flux line lattice as the field was increased from low to intermediate fields [54]. This transition is common for both magnetic and non-magnetic borocarbides and has been observed for Re = Y, Lu, Er and Tm [55, 56, 7].

Figure 28 shows a Bitter decoration of the flux line lattice in $R = Tm$ revealing the hexagonal symmetry at an applied field $H = 20$ Oe and the square lattice at $H = 2$ kOe observed with SANS.
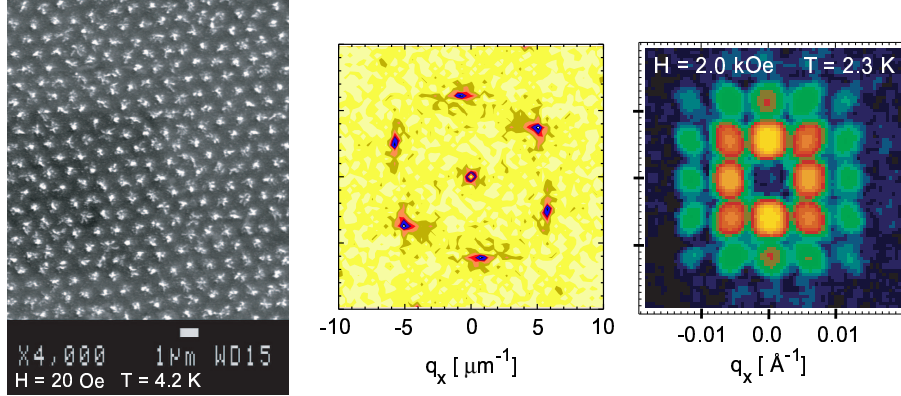
Figure 28. The flux line lattice changes from hexagonal to square symmetry as the applied along the c-axis is increased from low to intermediate fields as shown in the case of $R = Tm$. Left: Decoration of the surface with magnetic particles collecting at the flux line centers imaged by a scanning electron microscope. Middle: Fourier transform of the decoration image showing a hexagonal lattice at $H||c = 20$ Oe. Right: Neutron diffraction pattern of the flux line lattice at $H||c = 2$ kOe revealing the square symmetry.

7.1 Hexagonal to square symmetry transition

From the theoretical introduction to Ginzburg Landau theory it was argued that the inherent structure of the flux line lattice is hexagonal and some extension of the model is needed to stabilize the square lattice. It should also be noticed that the anisotropy introduced in section 2.9 result in isotropic properties of the ab-plane of the borocarbides, since the band structure is identical along the a and b direction and the effective masses likewise. The extension of the model must therefore include the four-fold symmetry of the Fermi surface and by minimum describe the superconducting properties along the high symmetry directions [100] and [110] of the ab-plane.

This has been done by adding higher order gradient terms of the form

$$C_2 \left\{ \left| D_x^2 \Delta(\boldsymbol{r}) \right|^2 + \left| D_y^2 \Delta(\boldsymbol{r}) \right|^2 \right\} \tag{193}$$

to the free energy expansion (15) where

$$D_\alpha = -i\nabla_\alpha - \frac{2eA_\alpha}{\hbar c} \tag{194}$$

The square lattice could thereby be obtained by a suitable choice of the pre-factor C_2 [57]. However the GL theory is only strictly valid at the phase-transition and the accuracy of the additional terms can be questioned well below the H_{c2} line at low and intermediate flux line densities. An alternative is to re-derive the London equation from microscopic theory and examine corrections caused by the symmetry of the Fermi-surface. This has been done by Kogan *et. al.* [58, 22] offering an explanation for the field induced hex to square symmetry transition.

7.2   Non-local Electrodynamics

One of the major differences between microscopic and Ginzburg-Landau theory is a non-local relation between current and vector potential reflecting the finite extent of a Cooper pair given by the coherence length ξ_0. Non-local refers to the fact that the current response $\boldsymbol{j}(\boldsymbol{r})$ of the condensate at the point $\boldsymbol{r}$ depends on the vector potential $\boldsymbol{A}$ within a sphere of size ξ. This non-local electrodynamics was first suggested by Pippard and takes the form

$$\boldsymbol{j}(\boldsymbol{r}) = C \int \frac{[\boldsymbol{A}(\boldsymbol{r}') \cdot \boldsymbol{R}]\boldsymbol{R}}{R^4} \exp\left(-\frac{R}{\xi}\right) d(\boldsymbol{r}') \quad \boldsymbol{R} = \boldsymbol{r} - \boldsymbol{r}' \tag{195}$$

where the effective coherence length ξ is limited by the mean free path l of the normal electrons

$$\frac{1}{\xi} = \frac{1}{\xi_0} + \frac{1}{l} \tag{196}$$

Thus the presence of impurities tend to decrease the mean free path l and thereby shrink the integration volume, whereby the Pippard relation reduces to the local relation in the "dirty" limit where $l << \xi_0$.

The Pippard expression is written as a convolution between the vector potential and a function $Q(\boldsymbol{r} - \boldsymbol{r}')$ called the kernel. In Fourier space this relation becomes the product between the Fourier transform of the two functions and generally

$$\boldsymbol{j}(\boldsymbol{k}) = Q(\boldsymbol{k})\boldsymbol{A}(\boldsymbol{k}) \tag{197}$$

where the kernel is determined from microscopic theory.

7.3   Nonlocal London theory

Kogan and co-workers [58] have used the Eilenberger formulation of the BCS theory to derive the kernel in the limit of small currents where the magnitude of the order parameter is unchanged, which is a good description of the high-κ superconductors, where the core is considered as a singularity as discussed in chapter 2.4. By introducing suitable expansions and keeping terms of lowest order they arrive at the following relation between current j_i and generalized vector potential a_j [22]

$$\frac{4\pi}{c}j_i = -\frac{1}{\lambda^2}\left(m_{ij}^{-1} - \lambda^2 n_{ijlm}k_l k_m\right)a_j \tag{198}$$

which reduces to the anisotropic London equation introduced in chapter 2.9 if the second term is neglected, which happens in the limit of $\boldsymbol{k} \to 0$. Small k values means changes in the vector potential on large length scales, where the London model works fine. However the second term becomes large when

$$k^2 > \frac{1}{\lambda^2 n_{ijlm}} = \frac{1}{\rho^2} \tag{199}$$

which defines a new length scale denoted the non-locality radius ρ and the second term in (198) gives the non-local corrections to the London equation.

The four fold symmetry of the Fermi surface and thereby the coupling to the crystalline lattice is taken into account by the 4 rank tensor n_{ijlm} given by

$$n_{ijlm} = C \frac{< v_i v_j v_l v_m >}{< v^2 >^2} \tag{200}$$

where $<>$ denoted the average over the Fermi surface, v_α ($\alpha = x, y, z$) are the Fermi surface velocities and the pre-factor C is

$$C = \frac{\hbar^2 < v^2 >^2 \gamma}{4 D \Delta_0^2 \lambda^2} \tag{201}$$

with D being the normalization of the inverse masses $D = (det < v_i v_j >)^{\frac{1}{3}}$), Δ_0 the zero temperature BCS gap, λ the penetration depth and γ is a function depending on impurity scattering time τ and temperature. In the clean limit ($\tau \to \infty$) γ is $\frac{2}{3}$ at T = 0, but it is reduced to 0 in the dirty limit ($\tau \to 0$) and the non-local corrections vanish. These expressions boil down to showing that the non-local radius is of the order of the zero temperature coherence length ξ_0.

From the current-vector potential relation the fourier components of the magnetic field h_z can be determined by imposing the flux quantization condition and for the applied field along the c-axis they become

$$h_z(\boldsymbol{k}) = \frac{\Phi_0}{1 + \lambda_{ab}^2 k^2 + \lambda_{ab}^4 (n_2 k^4 + d k_x^2 k_y^2)} \tag{202}$$

with $n_1 = n_{aaaa}$, $n_2 = n_{aabb}$ and the anisotropy of the non-local corrections in the ab-plane given by $d = 2n_1 - 6n_2$. The real space field distribution of an isolated flux line can be obtained analytically [17] for the isotropic case giving

$$h_z(\boldsymbol{r}) = \frac{\Phi_0}{2\pi\lambda^2} \left[K_0 \left(\frac{r}{\lambda} \right) - K_0 \left(\frac{r}{\rho} \right) \right] \tag{203}$$

The first term is the usual London expression given by the modified Bessel function K_0, but the divergence at the core is removed by the second term, which is the non-local correction being large within the non-local radius ρ as shown on figure 29.

Equilibrium flux line lattice

The fourier components of the field given by (202) is just what is needed to apply the Fourier method outlined in chapter 2.7 for a determination of the equilibrium flux line lattice in the borocarbides. However the components for $k > \frac{1}{\xi_0}$ are still not correct due to the singular description of the core, but instead of introducing a cut-off in the summations of the Fourier components Kogan *et. al.* multiplied them by an exponential factor of the GL form $\exp(-\xi^2 k^2)$, which suppresses the fourier components at high k. Thus the effective Fourier components of the non-local model are given by

$$h_z(\boldsymbol{k}) = \frac{\Phi_0}{1 + \lambda_{ab}^2 k^2 + \lambda_{ab}^4 (n_2 k^4 + d k_x^2 k_y^2)} \exp(-\xi^2 k^2) \tag{204}$$

Using bandstructure calculations for LuNi$_2$B$_2$C to obtain the Fermi velocity averages and thereby estimates of the non-local corrections Kogan *et. al.* were
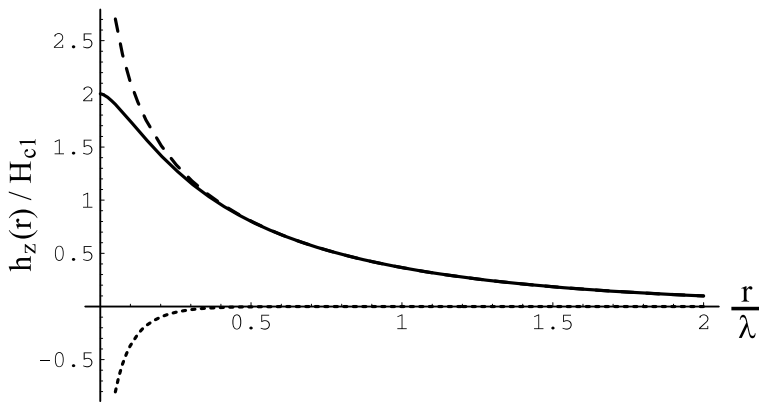
---

[17]Kogan *et. al.* [58] Appendix B

Figure 29. Illustration of the field distribution of an isolated flux line described by the isotropic non-local London model. The standard London result shown by the dashed curve is diverging at the core, but the non-local correction shown by the dotted curve gives a negative contribution within the non-local radius $\rho \sim \xi_0$ and removes the divergence in the resulting field distribution shown by the solid curve. $\kappa = 10$ and $\rho = 0.1\,\lambda$ has been used to construct the plot.

able to calculate the free energy per flux line lattice unit cell as function of the opening angle β between the two unit vectors spanning the cell.

Figure 30 shows the free energy as function of opening angle β at two different fields. A single minimum at $\beta = 90^o$ is found for the high field curve confirming a square flux line lattice with the diagonal along the a axis, but at lower field the square minimum splits up into two equivalent minima and the symmetry of the flux line lattice is rhombic. The two minima reflect the 4-fold symmetry of the Fermi surface, which makes the energy of the 2-fold symmetric rhombic lattice equivalent when the diagonal of the unit cell is either along the a or b axes. This degeneracy will cause the flux line lattice to split up into domains oriented along the principal axes.
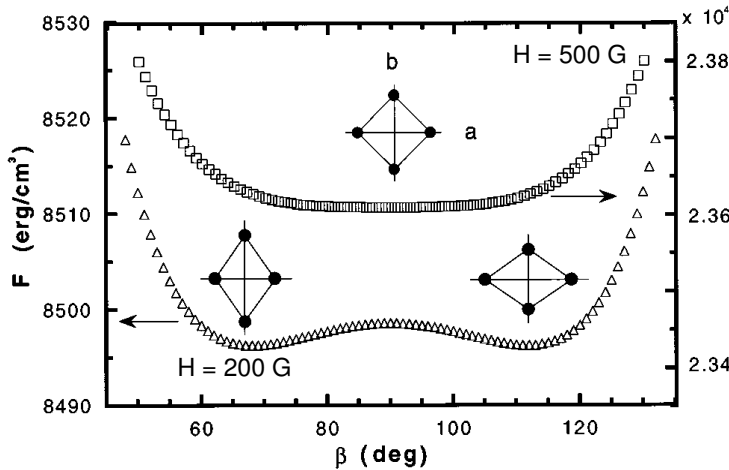
Figure 30. Free energy of the flux line lattice induced by a field $H\|c$ as function of the opening angle β of the unit cell. A rhombic lattice is found at low fields and the square lattice becomes stable at higher fields. Taken from Kogan et. al. [22].

Figure 31 shows the opening angle β of the equilibrium flux line lattice as

function of applied field along the c and a axis. For $H||c$ the square lattice is stable for applied fields above H_2 and the opening angle of a rhombic lattice gradually decreases towards the hexagonal configuration below H_2. However a reorientation transition where the unit cell rotates 45° is taking place at the field H_1.

The story is basically the same for $H||a$, where the opening angle is scaled by the anisotropy of the masses along the a and c axis and the saturation field H_2 is higher due to different Fermi surface averages in the ac-plane. However the 45° degree reorientation transition is absent.
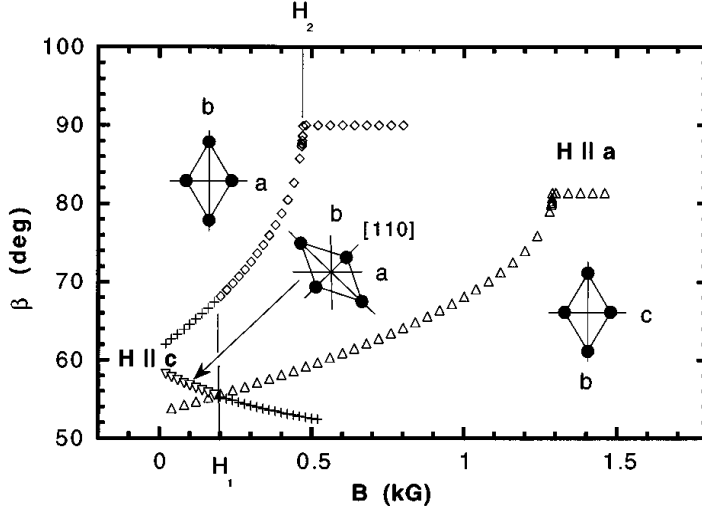
Figure 31. Equilibrium opening angle β and unit cell orientation as function of applied field along the a and c axis. For $H||c$ the unit cell starts out as almost hexagonal and with the diagonal of the cell along the [110] direction. At $H = H_1$ the orientation of the cell rotates 45° and the opening angle of the rhombic cell gradually increases towards 90° of the square lattice, which is found above $H = H_2$. The reorientation transition is absent for $H||a$ and the angle change is scaled by the mass anisotropy in the ac-plane. Taken from Kogan et. al. [22].

In summary the hexagonal to square flux line lattice transition is driven by the non-local corrections, which are dominant when the vector potential is changing on length scales similar to the non-local radius ρ. This happens in two situations a) close to the vortex core as illustrated on figure 29 and b) when the field distributions of the flux lines become highly overlapping. The transition field H_2 is therefore expected to occur at a certain flux line overlap when the distance between the flux lines $a = \sqrt{\frac{\Phi_0}{B}}$ is some factor c_{NL} larger than the non-locality radius ρ

$$\Phi_0 = \bar{B}_2 a^2 = \bar{B}_2 (c_{NL}\rho)^2 \Rightarrow \bar{B}_2 = \frac{\Phi_0}{(c_{NL}\rho)^2} \tag{205}$$

Thus the presence of impurities will move the transition towards higher fields compared to the "pure" case, since the non-local radius ρ will shrink when the mean free path l of the normal electrons decreases below the coherence length ξ_0.

The square symmetry of the flux line lattice above H_2 is caused by the 4-fold symmetry of the non-local corrections reflecting the underlying Fermi surface symmetry. At low fields the corrections are only affecting the field distribution close to the cores resulting in a 4-fold symmetry, with the field along [110] decaying a bit faster than along [100]. Far from the core the field distribution of an isolated flux

line becomes isotropic and the overlap of these nearly isotropic flux lines result in a lattice of almost hexagonal symmetry, as shown on figure 32a. When the overlap between the flux lines increases a larger part of the unit cell is influenced by the non-local corrections favoring a 4-fold symmetric field distribution, which is obtained for the square lattice as illustrated on figure 32b. Figure 32c shows the resulting reciprocal lattice of the two rhombic lattices, which smoothly approaches the same square lattice as the opening angle of the unit cell increases towards $\beta = 90^o$ when the field is increased.
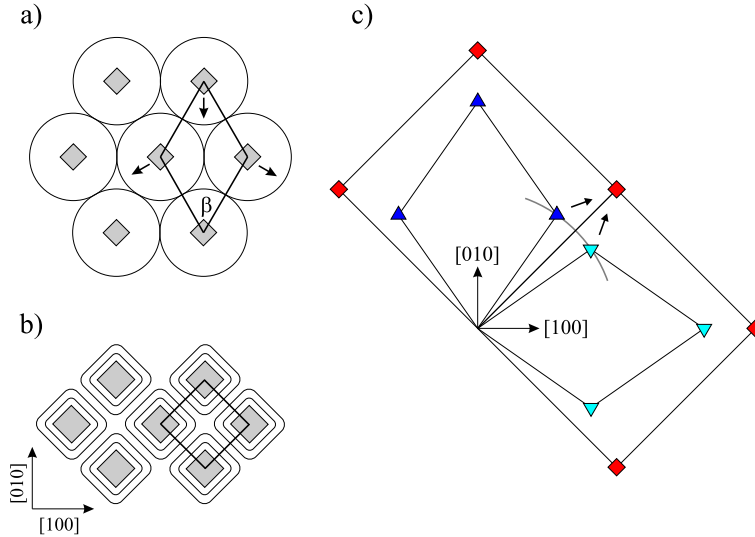
Figure 32. a) Low field hexagonal lattice formed of flux lines, which are corrected by non-local electrodynamics close to the cores making the field distribution 4-fold symmetric(shaded squares) and locks the flux line lattice to the crystalline lattice. The corrections vanish far from the core and the overlap of nearly isotropic field distributions result in an almost hexagonal lattice. Arrows indicate the movement of the flux lines as the field and thereby the opening angle β of the unit cell increases towards 90° of the square lattice. b) The non-local corrections are effective in a large part of the unit cell at intermediate fields, whereby a 4-fold symmetric field distribution is favored and the square lattice result. c) Transition from rhombic to square symmetric unit cell $\beta \approx 60 \rightarrow 90^o$ shown in reciprocal space. There are two co-existing rhombic lattices at low fields, one lattice with a unit cell equal to a)(∇) and one which is rotated by 90° ($\triangle$). The unit vectors form pairs around the [110] direction and the angular splitting along the arc shown by grey is $\beta' = 90^o - \beta$. Thus the two rhombic unit cells collapses into the square unit cell at the transition field H_2.

Experimental verification of the Non-local London model

The features of the Kogan model has been studied experimentally and qualitative agreement has been found with a few minor differences. A systematic SANS study by Gammel *et. al.* [56] of the transition field H_2 in $Lu(Ni_{2-x}Co_x)B_2C$ confirmed that a decrease of the mean free path by the introduction of magnetic Co impurities moved the transition towards higher fields. This proved that the non-local electrodynamics is the physics driving the hexagonal to square symmetry transition and that direct comparison between transition fields observed in different samples is difficult due to the difference in the sample specific mean free path.

The reorientation transition at H_1 has been observed with SANS in $R = Y$ by McPaul *et. al.* [59] and more convincing by Bitter decoration of annealed sample by Vinnikov *et. al.* [60]. For $H||a$ STM measurements by Sakata *et. al.* [43] have shown the transition into a distorted square lattice at high fields $H = 1\,T$, but a 90° degree reorientation transition has been observed at lower field in the STM measurement and with SANS by Eskildsen *et. al.* [61]. This transition can not be explained by the Kogan model and Knigavko *et. al.* [62] have argued that its origin is an anisotropic gap, which was introduced into a two band model.

Phase boundary of the square flux line lattice

Figure 33 shows the phase boundary $H_2(T)$ of the square flux line lattice in $R = Lu$ determined by a vanishing angular splitting β' between the unit vectors of the rhombic lattices as defined on figure 32c. The splitting was determined from the SANS diffraction pattern of the reciprocal lattice and the insert shows the azimuthal intensity distribution along the grey arc on figure 32c. At $T = 2\,K$ the peak is resolution limited with an azimuthal width of 13.8^o, but at higher temperature $T = 12\,K$ the width increases above the resolution and the splitting of the two rhombic unit vectors was determined by fitting the intensity distribution with two gaussian peaks of fixed width given by the resolution. The resolution was kept constant at different fields by adjusting the neutron wavelength. The procedure above resulted in a $\pm 2^o$ error in the zero split limit and the transition field H_2 was defined somewhat above this value at $\beta' = 3^o$ as indicated on the figure.
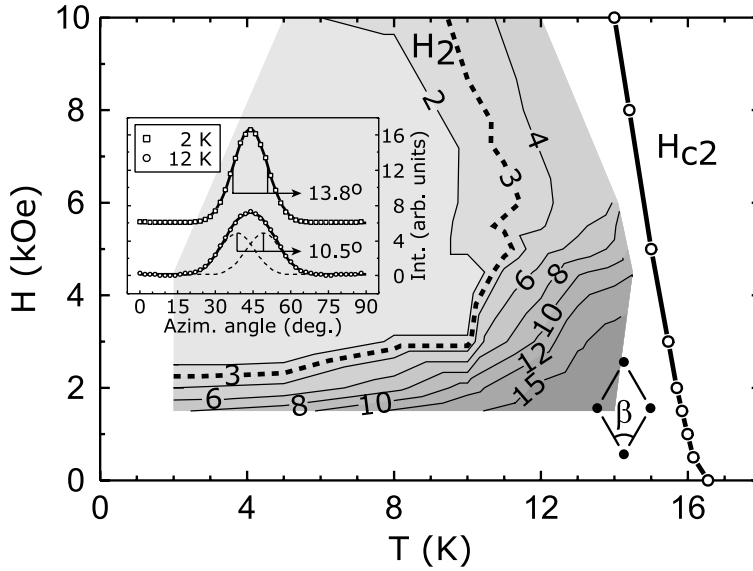

Figure 33. Contour plot of the angular splitting β' between the unit vectors of the two rhombic lattices induced by an applied field along the c-axis of $LuNi_2B_2C$. The insert shows the azimuthal intensity distribution at $H = 3.0\,kOe$ and the splitting of the reciprocal lattice vectors is determined by fitting two gaussian functions to the curve. The transition field H_2 from the square to hexagonal symmetry has been defined by the criteria that $\beta' = 3^o$ taking the experimental error margin into account. Taken from Eskildsen et. al. [63].

Below $T = 10\,K$ the transition field $H_2(T)$ is only increasing slightly with temperature as expected from the Kogan model. Above $T > 10\,K$ the non-local London model breaks down as the upper critical field is approached and the order

parameter is suppressed between the flux lines. Kogan has argued [63] that, this suppression causes the free energy to increase, but the larger separation between the flux lines in the hexagonal lattice will favor this compared to the square lattice and $H_2(T)$ is bending away from the upper critical field H_{c2} line. From this argument a flux line lattice of a symmetry closer to the hexagonal than square is expected close to H_{c2}, which is also argued by Gurevich *et. al.* [64] from the influence of thermal fluctuations.

8 Interaction between magnetism and superconductivity in $\mathrm{TmNi_2B_2C}$

The Tm member of the borocarbides orders magnetically while it is superconducting and a quite intricate composite phase diagram has been observed by Eskildsen *et. al.* [7] using small angle neutron scattering. However an understanding of the interaction between the flux line lattice and the magnetism has remained unclear since the publication in 1998. Here a series of experiment and a reexamination of the original data in [7] will be presented and a re-interpretation of the data is proposed.

8.1 Phase diagram for $H\|c$

Figure 34 show the composite phase diagram of $\mathrm{TmNi_2B_2C}$ with the applied field along the crystalline c-axis. Superconductivity is observed below a $T_c = 10.8\,K$ and co-existing magnetism in the form of a spin density wave is observed below a Néel temperature $T_N = 1.5\,K$. The lattice spacing of the tetragonal unit cell is $a = b = 3.4866\,\text{Å}$ and $c = 10.5860\,\text{Å}$ [5].

Magnetism

The spin density wave in zero magnetic field propagates with an incommensurate wavevector $q_{mI} = [0.094a^*, 0.094b^*, 0]$, where a^* and b^* are reciprocal unit vectors of the crystallographic ab-plane, and the moment $\mu = 3.78\mu_B$ is directed along the crystalline c-axis [5]. Magnetization measurements [44] and inelastic neutrons scattering studies [65] in the paramagnetic phase show that the crystal-field(CEF) splitting causes the system to become almost Ising-like with the c-axis as the easy axis. As the applied field is increased above $H = 2.0\,kOe$ a suppression of the zero field phase begins while a new spin density wave appears with a propagation vector rotated by 45 degrees with respect to q_{mI} and with a magnitude $q_{mII} = 0.88\,q_{mI} = 0.21\,\text{Å}^{-1}$ [7]. A splitting into pairs of reflections separated between $11 - 15^o$ around the [100] direction can be observed depending on the field history [66, 8].

Superconductivity

At low fields $H = 0 - 1\,kOe$ the flux line lattice changes from a hexagonal to square symmetry seen by an increase of the opening angle of the FLL unit from $\beta_u \approx 60^o \rightarrow 90^o$ and with the diagonal of the unit cell along the crystallographic $\hat{a}$ or $\hat{b}$ direction as shown on figure 28. This transition is common for both the magnetic and non-magnetic borocarbide superconductors and is caused by corrections to the flux line interaction by non-local electrodynamics as explained in chapter 6. However the square FLL changes into two rhombic lattices with the diagonal of the unit cell still along the crystallographic $\hat{a}$ or $\hat{b}$ direction but with the opening angle decreasing from 90° towards lower values around 70° as the applied field is increased. At low temperature and high fields a third FLL phase of hexagonal symmetry is observed, but the diagonal of the unit cell is rotated 45 degrees compared to the previous phases and is now directed along the crystalline [110] direction.
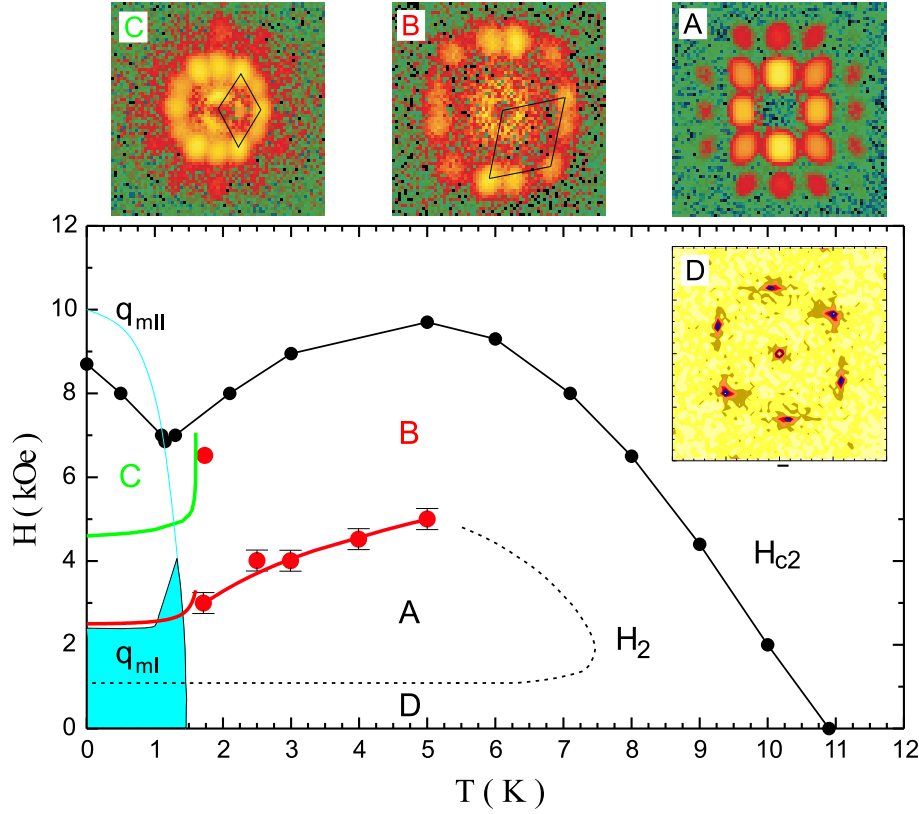
Figure 34. Composite phase diagram of magnetism and superconductivity in
$TmNi_2B_2C$ when $H \| c$. Four flux line lattice phases denoted A, B, C and D
with different symmetries are seen below the critical temperature $T_C = 11.0\,K$ of
the superconducting phase and two spin density waves denoted q_{mI} and q_{mII} are
observed below the magnetic ordering temperature $T_N = 1.5\,K$. The A phase is a
square FLL lattice resulting from non-local electrodynamics imposing the symmetry
of the Fermi surface in the ab-plane into the FLL when the flux lines are suffi-
ciently overlapping. A SANS diffraction pattern of the square FLL at $H = 2.0\,kOe$
and $T = 2.3\,K$ is shown in the insert A with the crystalline (110) directions hor-
izontal and vertical. As the overlap is reduced at lower fields the symmetry is
changing smoothly towards hexagonal marked as the D phase and the insert shows
the Fourier transform of a magnetic decoration at $H = 20\,Oe$ and $T = 4.2\,K$,
but the orientation of the FLL is arbitrary with respect to the SANS diffraction
patterns. All borocarbides have shown the AD transition and the lower part of the
H_2 line in the figure is only a guide to the eye, since it is based on the decoration
at $H = 20\,Oe$ and the SANS diffraction patterns above $H = 1.0\,kOe$. The B-phase
consist of two rhombic lattices with the unit cell diagonal along the crystallographic
$\hat{a}$ or $\hat{b}$ direction and an opening angle of $\beta_u \approx 75^o$ as shown on insert B corre-
sponding to the point at $H = 6.5\,kOe$ and $T = 1.7\,K$. The C phase is observed at
low temperature and high field and is composed of two hexagonal lattices with the
unit cell diagonal along the crystallographic [110] direction as shown on the insert
for $H = 6.0\,kOe$ and $T = 1.0\,K$. The AB-phase boundary(red points) has been
found by the author as shown in later sections, while the low temperature phase
diagram $(T < 1.7\,K)$ has been reproduced from Eskildsen et. al. [7].

8.2   Determination of AB FLL phase boundary in the paramagnetic region

The transition from the square A to the rhombic B FLL phase in $TmNi_2B_2C$ appears similar to the symmetry transition from the low field hexagonal phase into the square phase as illustrated on figure 32. Thus the AB phase boundary can be determined by studying the splitting of the square FLL diffraction spots as function of applied field, which has been done in the paramagnetic phase in order to complete the FLL phase diagram on figure 34. All measurement were done at constant neutron wavelength, because a direct comparison of the FLL reflectivity at different fields and temperature was preferred over a mode of constant resolution at the time of the experiment. This give some limitation in the fitting procedure, since the resolution must be estimated.

Experimental conditions

The 6 m SANS camera in the cold neutron guide hall at the Risø DR3 reactor was used to study the sample sitting in a 5 tesla Oxford cryomagnet holding a 1K pot for cooling to 1.5 K. Diffraction patterns from the FLL were obtained by cooling the sample below T_c in a field along the crystalline $\hat{c}$-axis and rotating the cryostat $\pm 4^o$ with the flux lines directed along the neutron beam. The crystalline small angle neutron scattering background of the sample was determined by cooling the sample below T_c in zero applied field and this background was subtracted from the data. All diffraction patterns were taken at the same neutron wavelength $\lambda_n = 6.75$ Å with a wavelength spread of $\frac{\Delta\lambda}{\lambda} = 0.18$ and the settings of the SANS camera were : Collimation $L = 6.0$ m, sample detector distance $l = 6.0$ m, Pinhole1 circular diameter $D_1 = 25mm$, pinhole2 rectangular 4.5×6.0 mm.

Azimuthal intensity distribution

Figure 35 shows how the azimuthal distribution of the scattering is obtained by integrating the detector intensity in intervals of the azimuthal angle and in a radial band of momentum transfer in the range $\kappa = \tau_{FLL} \pm \Delta\kappa$. Diffraction patterns of summed rocking curves are shown on the left hand side and the corresponding azimuthal intensity distribution is shown on the right hand side. Fits by a single gaussian function are summarized in figure 36 and show the FWHM width as function of applied field and different temperatures. The curves almost collapse into one curve at low applied fields with small error bars, but an increase of the width is seen as the applied field is increased and the error bars increase as the peaks of the rhombic B phase can be resolved separately. Figure 37 shows the splitting between the rhombic peaks determined by fitting two gaussian functions to the azimuthal intensity. A splitting of zero has been inserted when the fit effectively reduced to one gauss function and the error bar of the peak position has been assigned. The two peak fits for $T = 4\,K$ has been shown without setting the splitting to zero to illustrated the unsuccessful fitting at low applied fields.

Discussion

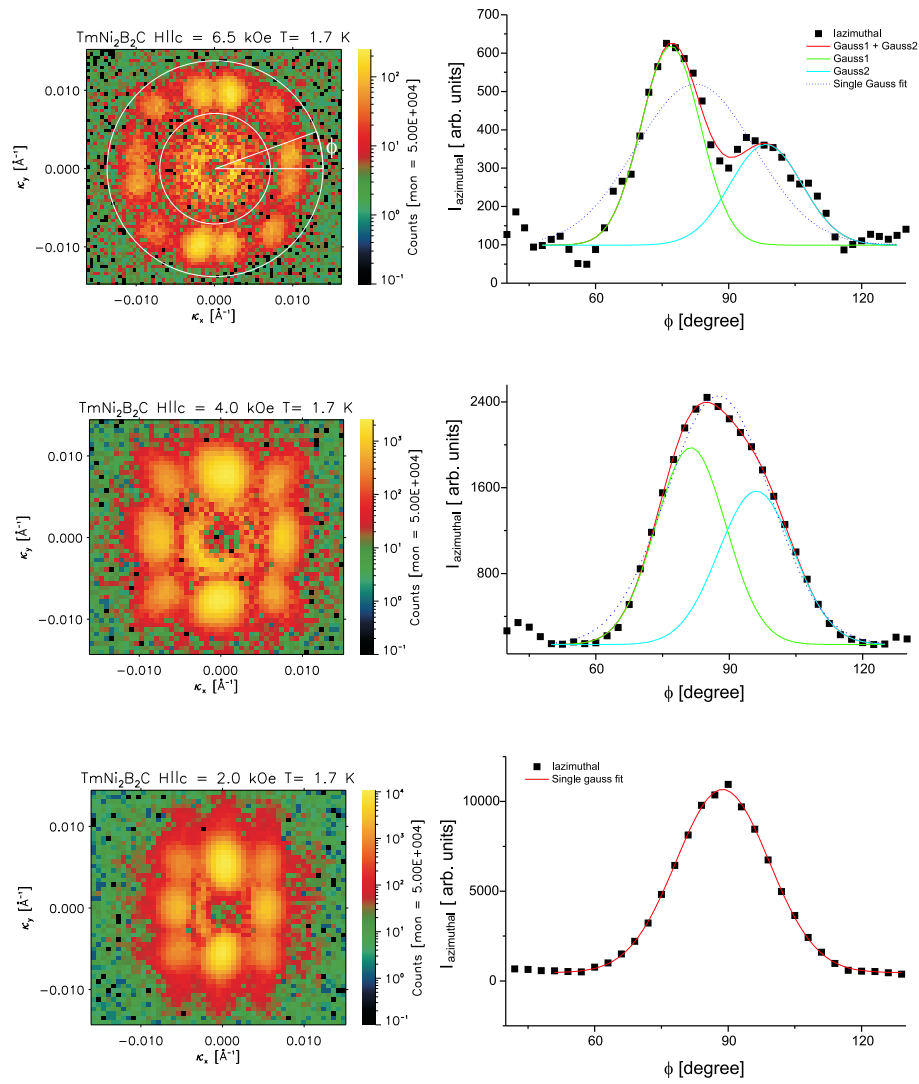An estimate of the FWHM angular resolution can be obtained from the azimuthal resolution in reciprocal space

Figure 35. Left : Diffraction patterns of FLL scattering across the transition from the B(top) to the A(bottom) FLL phase at $T = 1.7K$. The transition from the A to the B phase causes the vertical and horizontal peaks to split apart due to the rhombic symmetry of the B phase. Top figure was obtained at a neutron wavelength $\lambda_n = 9\,\AA$ to resolve the rhombic FLL better and $\lambda_n = 6.75\,\AA$ for all other figures. Right : Azimuthal intensity distribution found by integrating the intensity in angular slices between the two circles inclosing the FLL diffraction spots obtained at $\lambda_n = 6.75\,\AA$. The azimuthal intensity of the B phase can be fitted by two gaussian functions giving a FWHM width of 16.1 ± 1.0^o, which should be considered as the resolution and an angular splitting between the peaks of 21.5^o. A fit by a single gaussian function is shown by the dotted line giving a FWHM width of 31.4 ± 3.9^o with large error bars due to the bad fit. The splitting decreases across the transition from the B to the A phase and the azimuthal intensity distribution is best described by a single gaussian at $H = 2.0\,kOe$ giving a width of 24.6 ± 0.2^o.

$$\begin{aligned}
\Delta_\phi &= 2\sqrt{2\ln 2}\frac{\sigma_\phi}{\tau} \\
&= \frac{2\pi}{\lambda_n \tau}\Delta\phi_i \\
&= \frac{\sqrt{\Phi_0 \sin \beta_u}}{\lambda_n \sqrt{B}}\frac{D_1}{L}
\end{aligned} \qquad (206)$$
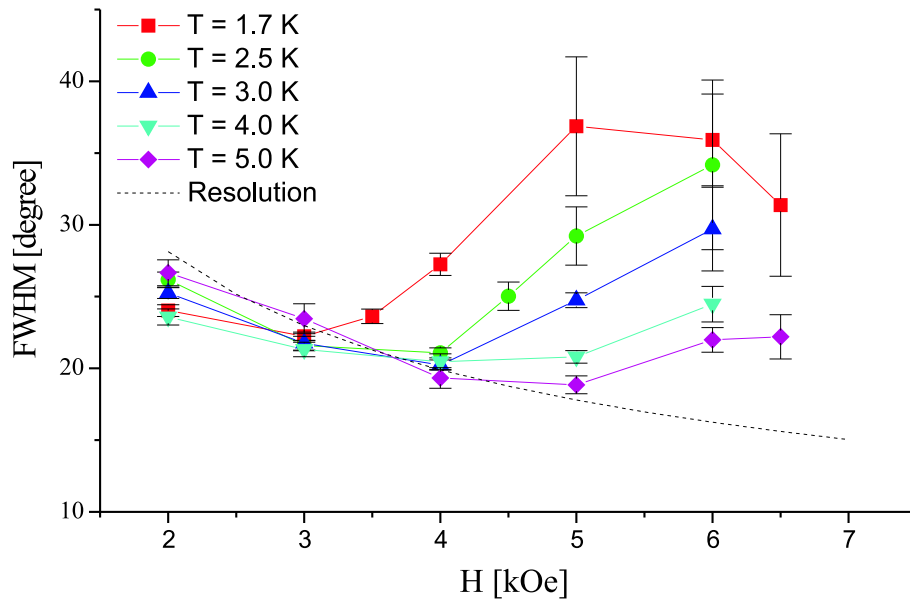
Figure 36. Full width half maximum width of gauss function fitted to the azimuthal intensity distribution. The curves almost collapse into one curve with a negative slope at low field, but an increase of the width is seen as the applied field is increased and large error bars appear when the two peaks of the rhombic B phase are resolved. The dashed line shows a rough estimate of the resolution fixed by the value 16.1° obtained from fitting the separated peaks of the B-phase at H = 6.5 kOe and T = 1.7 K. This indicate that the width of the peaks at low field are resolution limited.
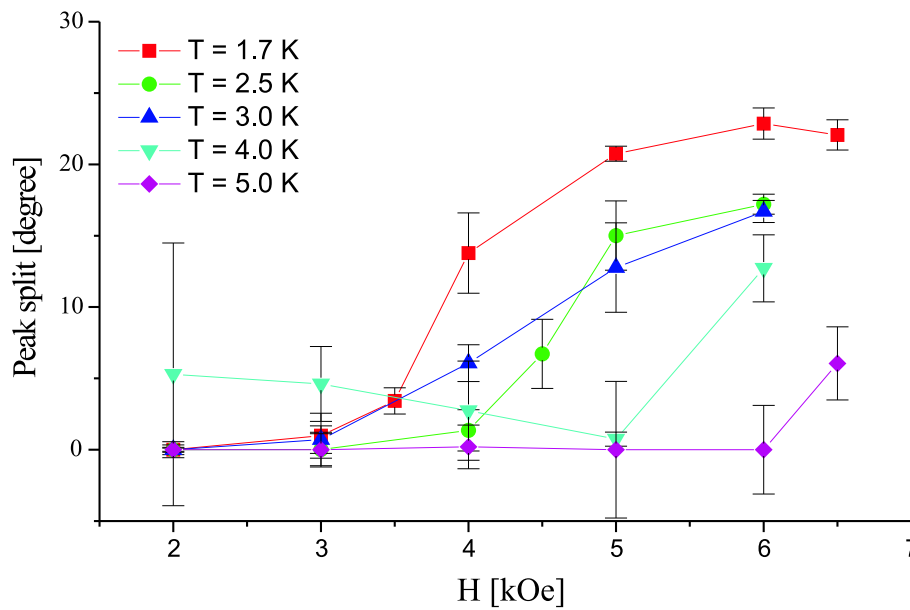
Figure 37. Split between two gauss peaks fitted to the azimuthal intensity distribution. These fits were only possible in the B phase and a splitting of zero was assign when the two peak fit reduced to one peak. The large error bars for T = 4 K and at low field illustrates a failed fitting.

where the reciprocal lattice vector τ depending on the field B and the unit cell opening angle β_u

$$\tau = \frac{2\pi}{\sqrt{\sin \beta_u}}\sqrt{\frac{B}{\Phi_0}} \tag{207}$$

has been inserted together with the beam divergence

$$\Delta\phi_i = \frac{2r_1}{L} = \frac{D_1}{L} \tag{208}$$

Thus it is seen that the angular resolution is expected to scale as $\frac{1}{\sqrt{B}}$ and the dashed line on figure 36 has been constructed from this functional form and by fixing the resolution to the width obtained in the two gauss peak fit at $H = 6.5\,kOe$ and $T = 1.7\,K$. The estimated resolution is in qualitative agreement with the measured width at low fields, where the diffraction spots are resolution limited. The transition from the A to the B phase can now be defined as the field where the slope of the gauss width curve changes from negative to positive indicating that the width of the diffraction spot is increasing above the resolution limit and the red points on figure 34 has been constructed from this criteria by assigning an error bar of $\pm 0.5\,kOe$ to each point. The red line through the points is only a guide to the eye.

It is interesting to note the similarity between the AB phase boundary and the H_{c2} curve indicating that these are closely related. Kogan has argued that the square FLL is destabilized when the cores of the flux lines start to overlap due to the loss of condensation energy and the hexagonal symmetry is thereby favored because the separation between the flux lines is larger compared to the square lattice (see section 7.3). Thus the physics driving the AB transition seems to be the crossover from intermediate flux line density to high flux line density and the transition field can be determined by the criteria that the flux line spacing a is some factor c_{IH} larger than the core size given by the coherence length ξ whereby $a = c_{IH}\xi$ and

$$\Phi_0 = B_{AB}a^2 = B_{AB}c_{IH}^2\xi^2 \Rightarrow B_{AB} = \frac{\Phi_0}{c_{IH}^2\xi^2} \tag{209}$$

The upper critical field is given by $B_{c2} = \frac{\Phi_0}{2\pi\xi^2}$ and the AB transition field can thereby be written as

$$\frac{B_{AB}}{B_{c2}} = \frac{2\pi}{c_{IH}^2} \tag{210}$$

From figure 34 the above ratio can be determined giving $\frac{B_{AB}}{B_{c2}} = 0.40 - 0.53$ between $T = 1.7 - 5.0\,K$ and the corresponding scaling factor becomes $c_{IH} = 3.96 - 3.45$.

D. McK. Paul and co-workers [18] have reported similar studies on $TmNi_2B_2C$ with $H||c$ and found that the FLL only approaches the square symmetry with a maximum opening angle of $\beta_u = 78.5^o$ at an applied field of $H = 3\,kOe$ as shown on figure 38. A plot of the maximum opening angle in the HT phase diagram is shown in figure 39 and is very similar to the AB phase boundary described in this report and shown on figure 34. The fact that D. McPaul *et. al.* never sees a square lattice is probably connected to a higher impurity concentration in the sample, whereby the transition line H_2 between the A and D FLL phases is moved towards higher fields as discussed in section 7.3 and the square FLL phase might

---

[18]K.-H. Müller and V. Narozhnyi [67], page 323-332

disappear. However the transition into the high flux line density region will still take place and will be the same, since the B_{c2} lines are qualitatively identical for the two samples. Thus the largest opening angle of the flux line lattice will be found on the AB transition line, when the non-local corrections are to weak to drive the FLL all the way into the square symmetry.

The data of D.McPaul are interesting since they shows that the flux line lattice is driven towards the hexagonal symmetry at high temperatures, which supports the idea that the AB-phase boundary will follow the B_{c2} line in a similar way to what was found for $LuNi_2B_2C$ and shown on figure 33.

Based on the observations above it is suggested that the transition line $H_2 = \frac{\Phi_0}{r^2}$ consist of two branches which are determined from different length scales r. The AD transition line is caused by the non-local electrodynamics and the length scale involved is the non-locality radius ρ of the Kogan model $r = c_{NL}\rho$ (see equation 205), whereby a lower H_2 field is given by

$$H_{2l} \approx \frac{\Phi_0}{(c_{NL}\rho)^2} \tag{211}$$

The AB transition line is determined by the crossover from intermediate to high flux line density set by the length scale $r = c_{IH}\xi$ and the corresponding upper H_2 field is given by

$$H_{2u} \approx \frac{\Phi_0}{(c_{IH}\xi)^2} \tag{212}$$

with the coherence length ξ being the length scale connected to the upper critical field H_{c2} of the superconducting state by $r = \sqrt{2\pi}\xi$.

The qualitative trend of the composite H_2 curve is marked by the dashed line in the phase diagram shown on figure 34. This indicates that the vortex physics in the paramagnetic phase does not seem directly connected to the magnetism, but only indirectly because the presence of the Tm ions reduces the upper critical field H_{c2} and thereby defines the temperature dependence of the coherence length $\xi(T)$.

One could speculate that the AB transition in the magnetic ordered phase $T < T_N = 1.5\,K$ is also a crossover from the intermediate- to high flux line density, whereby the magnetic phase transition between q_{mI} and q_{mII} is driven by the symmetry change of the flux line lattice and the faster reduction of the superconducting order parameter as the field is increased. This argument is supported by the observation of hysteresis in the splitting of the magnetic diffraction spots of the q_{mII} phase depending on the field history of the sample as reported by Eskildsen *et. al.* [66]. The q_{mII} spots are split when the field is increased after cooling the sample to $T = 100\,mK$ in zero field, but the split is first observed when $H \leq 3\,kOe$ as the applied field is decreased below H_{c2} at $T = 100\,mK$.

The flux line lattice transition from the rhombic B to the hexagonal C phase is of first order since the unit cell is rotating 45 as shown by the inserts of figure 34. However the origin of this transition is still unclear, but might be related to the reduction of the superconducting order parameter whereby the influence of the magnetism increases.

In conclusion the vortex physics in the paramagnetic region is only indirectly influenced by the magnetism, which determines the features in the temperature dependence of the coherence length $\xi(T)$. The square flux line lattice is suggested to exists in between two transition lines $H_t = \frac{\Phi_0}{r^2}$ defined from two new length scales : the non-locality radius ρ caused by non-local electrodynamics of clean superconductors and the flux line cores size ξ which start to overlap when the flux line separation becomes $r = c_{IH}\xi$. Thus the length scales involved are
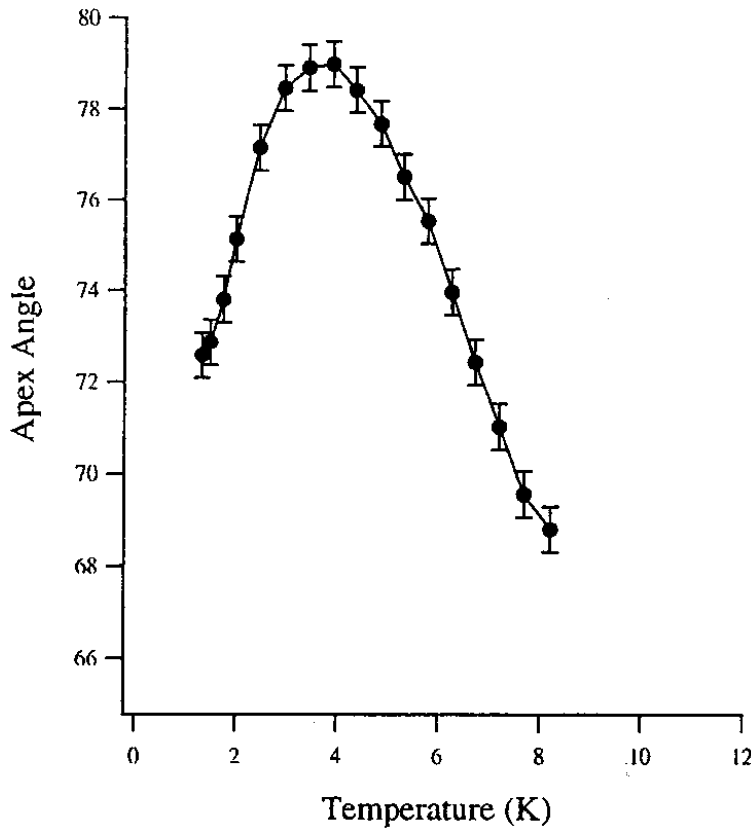
Figure 38. Opening angle of the FLL unit cell in $TmNi_2B_2C$ induced by an applied field of $H\|c = 3.0\,kOe$ as reported by D. McPaul et. al. [67] p. 330

$$r = \begin{cases} \sqrt{2\pi}\xi \\ c_{IH}\xi \\ c_{NL}\rho \\ \sqrt{\frac{\pi}{\ln\kappa}}2\lambda \end{cases} \Rightarrow H_t = \frac{\Phi_0}{r^2} = \begin{cases} H_{c2} \\ H_{2u} \\ H_{2l} \\ H_{c1} \end{cases} \tag{213}$$

resulting in the upper critical field H_{c2}, the upper- and lower transition field of the square flux line lattice and the lower critical field H_{c1} of the superconducting state. Finally the observed phase boundaries demonstrates that the idea of Kogan that the overlap of the vortex cores will drive the FLL away from the square symmetry is qualitatively correct.

8.3 Reflectivity analysis at $H\|c = 2.0\,kOe$

Besides the many changes seen in the symmetry of the flux line lattice as the magnetic phases are entered a large increase of the scattering is also observed as shown on figure 40. Again the interaction between superconductivity and magnetism is obvious and the change of the reflectivity indicates that the properties of the superconductor is changing dramatically across the magnetic phase transition. Here a quantitative analysis of the FLL reflectivity is performed in an attempt to determine how the superconducting length scales given by the penetration depth λ and the coherence length ξ are changing across the transition.
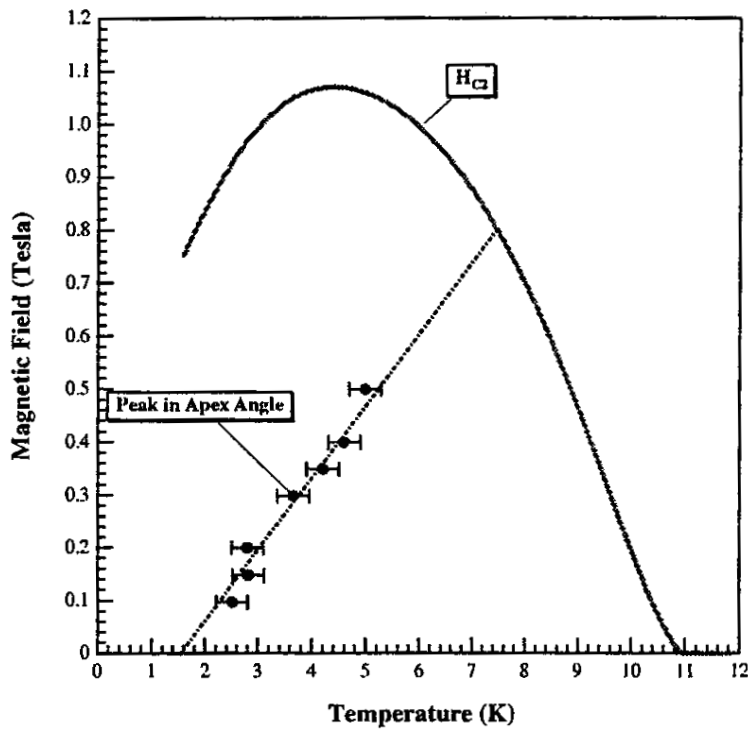
Figure 39. Position of maximum opening angle of the FLL unit cell in the HT phase diagram of $TmNi_2B_2C$ as found by D. McPaul et. al. [67] p. 330
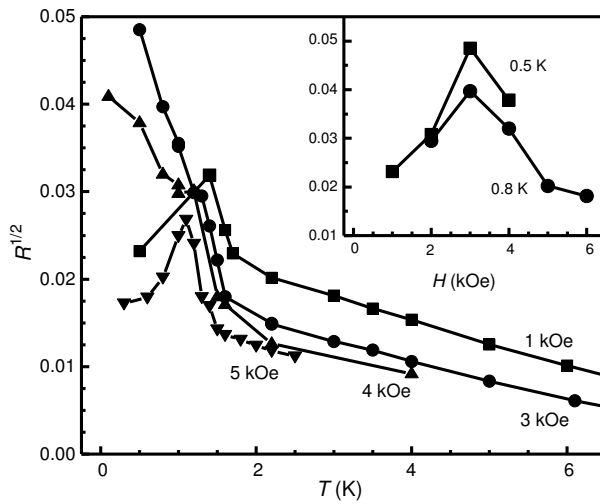

Figure 40. The reflectivity of the (10) FLL diffraction spot is showing large changes as the magnetic phases are entered below the Néel temperature $T_N = 1.5\,K$. The insert shows how the reflectivity is peaking when the phase boundary between the two magnetic phases q_{mI} and q_{mII} is crossed at constant temperature. Taken from Eskildsen et. al. [7].

Restricting the parameter space

From a theoretical point of view the description of the reflectivity of the flux line lattice in the borocarbides is quite limited, since one of the best suggestions in the form of the Kogan model outlined in section 7.3 is only valid for intermediate flux

line densities. A comparison between the Kogan model and the data is therefore restricted to the square or low field hexagonal flux line lattice. In the section about the neutron scattering from the flux line lattice at intermediate flux line densities it was argued that the neutron cross section can be separated into a form factor of an isolated flux line and a structure factor depending of the spatial configuration of the flux lines. Thus by making the reflectivity analysis at a constant field and in the square flux line lattice phase is equivalent to fixing the structure factor and all changes in the reflectivity should come from changes in the form factor of the isolated flux line. From the composite phase diagram in figure 34 it is seen that $H = 2.0\,kOe$ is inside the square phase A when the magnetic transition is crossed and this field was chosen for the analysis.

8.4 Extracting the superconducting length scales from the SANS reflectivity

Small angle neutron scattering has been used extensively to study the flux line lattice of superconductors and one of the main activities in the 70'ties was to compare newly developed descriptions of the flux line form factor with the experimental neutron scattering data on Niobium [68, 69, 70, 71]. The main approach was to examine how the reflectivity of the different diffraction spots decay in reciprocal space.

From the definition (177) of the reflectivity

$$R_{FLL} \quad = \quad 2\pi \left(\frac{\gamma}{4\Phi_0}\right)^2 \frac{L}{A_u^2} \frac{\lambda_n^2}{\tau \cos(\eta_\tau)} h(\boldsymbol{\tau})^2 \tag{214}$$

it is seen that it is proportional with the the square of the form factor $h(\tau)$ of an isolated flux line, which in the Kogan model takes the form

$$h_z(\boldsymbol{\kappa}) = \frac{\Phi_0}{1 + \lambda_{ab}^2 \kappa^2 + \lambda_{ab}^4 (n_2 \kappa^4 + d\kappa_x^2 \kappa_y^2)} \exp\left(-\xi^2 \kappa^2\right) \tag{215}$$

depending on both the penetration depth λ appearing in the denominator of the first factor describing the non-local London model and on the coherence length ξ in the exponential cut-off caused by the insufficient description of the flux line core in the London model. Thus the intensity of the diffraction spots will decrease the further out in reciprocal space the spots are positioned. Here it should be noted that the unit of the form factor $h(\tau)$ is $[field \times area]$, because it is the Fourier transform of the magnetic field distribution, but this also shows that one can introduce a normalized form factor by normalizing with either the flux quantum Φ_0 or with the area of the FLL unit cell A_u. In the first case used by Schelten $et.$ $al.$ [69] the normalized form factor becomes unit less and in the second case used by Forgan [72] it takes the unit of the magnetic field

$$F(\tau) \quad = \quad \frac{h(\tau)}{A_u} = \frac{\bar{B}}{\Phi_0} h(\tau)$$

$$= \quad \frac{\bar{B}}{1 + \lambda_{ab}^2 \tau^2 + \lambda_{ab}^4 (n_2 \tau^4 + d\tau_x^2 \tau_y^2)} \exp\left(-\xi^2 \tau^2\right) \tag{216}$$

which is in the same form as the solution obtained to the London equation in section 2.7 by expressing the field distribution as a Fourier series and using the flux quantization condition $\Phi_0 = \bar{B} A_u$. In the last case the reflectivity then becomes

$$R_{FLL} \quad = \quad 2\pi \left(\frac{\gamma}{4\Phi_0}\right)^2 \frac{L\lambda_n^2}{\tau \cos(\eta_\tau)} F(\boldsymbol{\tau})^2 \tag{217}$$

The superconducting length scales of several of the borocarbides have been determined from the SANS reflectivity of the (10) diffraction spot as the position of the diffraction spot in reciprocal space was changed by increasing the applied magnetic field [73, 74]. τ_{10} is related to the average field $\bar{B}$ in the FLL unit cell by the flux quantization condition $\Phi_0 = \bar{B} A_u = \bar{B}(\frac{2\pi}{\tau_{10}})^2$ whereby the flux line form factor $F(\tau_{10})$ can be rewritten

$$F(\tau_{10}) \quad = \quad \frac{\bar{B}}{1 + \frac{(2\pi\lambda_{ab})^2}{\Phi_0}\bar{B} + \left(n_2 + \frac{d}{4}\right)\frac{(2\pi\lambda_{ab})^4}{\Phi_0^2}\bar{B}^2} \exp\left(-\frac{c_\xi(2\pi\xi)^2}{\Phi_0}\bar{B}\right) \quad (218)$$

The factor $c_\xi = \frac{1}{4} - 2$ is introduced because the gaussian exponential cut-off is only an approximative description of the influence by the flux line core as suggested by Yaouanc $et.$ $al.$ [20]. By plotting the logarithm of the squared form factor an almost linear curve as function of the average field $\bar{B}$ is obtained due to the exponential cut-off

$$\ln F_{\tau_{10}}^2(\bar{B}) = \ln \frac{\bar{B}^2}{\left(1 + \frac{(2\pi\lambda_{ab})^2}{\Phi_0}\bar{B} + \left(n_2 + \frac{d}{4}\right)\frac{(2\pi\lambda_{ab})^4}{\Phi_0^2}\bar{B}^2\right)^2} - \frac{2c_\xi(2\pi\xi)^2}{\Phi_0}\bar{B} \quad (219)$$

Figure 41 shows a linear fit to $ln|F_{\tau_{10}}|^2$ for $LuNi_2B_2C$ on data reported by Eskildsen $et.$ $al.$ [73, 8] and the obtained fitting parameters are in close agrement with original parameters by Eskildsen $et.$ $al.$ [8]. The coherence length is determined from the slope of the linear fit, which is given by

$$\alpha = -\frac{2c_\xi(2\pi\xi)^2}{\Phi_0} \quad (220)$$

and the penetration depth is determined from the intersection with the axis, which can be approximated by neglecting the first and last term in the denominator of expression (219)

$$\beta = \ln\left(\frac{\Phi_0^2}{(2\pi\lambda)^4}\right) \quad (221)$$

One thereby obtains the values $\lambda = 1061 \pm 37 \, \mathring{A}$ and $\xi = 82.0 \pm 2.3 \, \mathring{A}$, which is deviating from recent transport measurements quite a bit with $\lambda = 690 \, \mathring{A}$ and $\xi = 60 \, \mathring{A}$ [36]. A choice of $c_\xi = 0.90$ would give the coherence length equal to the one determined from the transport measurement and it is still within the boundaries suggested by Yaouanc.

A fit by the full Kogan model given by (219) is also shown on figure 41 and the deviation from a straight line can be explained by the presence of the non-local corrections specified by the third term in the denominator. The following fitting parameters were obtained

$$p_1 \quad = \quad \frac{(2\pi\lambda)^2}{\Phi_0} = (1.56 \pm 0.11) \cdot 10^{-2} \, G^{-1} \quad (222)$$

$$p_2 \quad = \quad n_2 + \frac{d}{4} = (8.15 \pm 2.2) \cdot 10^{-3} \quad (223)$$

$$p_3 \quad = \quad \frac{2c_\xi(2\pi\xi)^2}{\Phi_0} = (4.01 \pm 0.7) \cdot 10^{-5} \, G^{-1} \quad (224)$$

giving $\lambda = 903 \pm 32 \, \mathring{A}$ and $\xi = 46 \pm 4 \, \mathring{A}$. Here the penetration depth is closer to the transport data, but the coherence length becomes smaller than the transport estimate and $c_\xi = 0.29$ is needed to make correspondence between the two.

The interesting detail of the fit with the full Kogan model is that it gives an estimate of the magnitude of the non-local corrections parameterized by p_2. In the original model calculation by Kogan *et. al.* [22] the non-local corrections were estimated by evaluating Fermi velocity averages of the Fermi surface of $LuNi_2B_2C$ determined from bandstructure calculations. The following parameters were reported

$$
\begin{aligned}
n_2 &= 0.0705c \\
d &= 0.675c \\
c &= 0.221 - 0.365
\end{aligned}
\tag{225}
$$

which should give

$$
p_2 = n_2 + \frac{d}{4} = 5.3 \cdot 10^{-2} - 8.7 \cdot 10^{-2}
\tag{226}
$$

This estimate is about a factor of 10 larger than the value obtained in the fit, but the non-local corrections depend on the impurity concentration of the sample and will vanish in the dirty limit. Thus fitting values smaller than the above estimate are quite likely.

When turning to $TmNi_2B_2C$ the method outlined in this section is breaking down completely as illustrated on figure 42. A slight increase of $ln|F_{\tau_{10}}|^2$ is seen for $H < 3\,kOe$ followed by a non-linear decrease. It is interesting to compare this field dependence with the composite phase diagram shown in figure 34, which indicates that the decrease of the form factor above $H = 3\,kOe$ is co-incident with the transition from the intermediate- to high flux line density.

Thus the method of analyzing the intensity of the most intense diffraction spot as the position in reciprocal space is increased by increasing the applied field is not applicable to $TmNi_2B_2C$ and an alternative is needed.

8.5 Reflectivity ratio

One way to compare the scattered intensity from the flux line lattice with any model without changing the applied field or temperature is to evaluated the ratio between the reflectivity of the different diffraction spots and the (10) peak. The advantage of this method is that many of the pre-factors entering the reflectivity equation (177) will drop out of the calculation giving

$$
\frac{R(\tau)}{R(\tau_{10})} = \frac{\tau_{10}\cos(\eta_{10})}{\tau\cos(\eta_\tau)}\left(\frac{h(\tau)}{h(\tau_{10})}\right)^2
\tag{227}
$$

By introducing the indexes n_a and n_b of the square flux line lattice with $\boldsymbol{a}$ horizontal and $\boldsymbol{b}$ vertical in figure 17 then the reciprocal lattice vectors are given by $\tau = \sqrt{n_a^2 + n_b^2}\,\tau_{10}$ and the geometric factor $\cos(\eta_\tau) = \frac{n_a}{\sqrt{n_a^2 + n_b^2}}$. The first factor in the reflectivity ratio then only depends on the index n_a of the FLL reflection in the horizontal plane, because this determines how fast the lattice point is rocked through the Ewalds sphere

$$
\frac{\tau_{10}\cos(\eta_{10})}{\tau\cos(\eta_\tau)} = \frac{1}{n_a}
\tag{228}
$$

Thus the reflectivity ratio is directly connected to the flux line form factor given by the Kogan model equation (215) as described in the previous section.
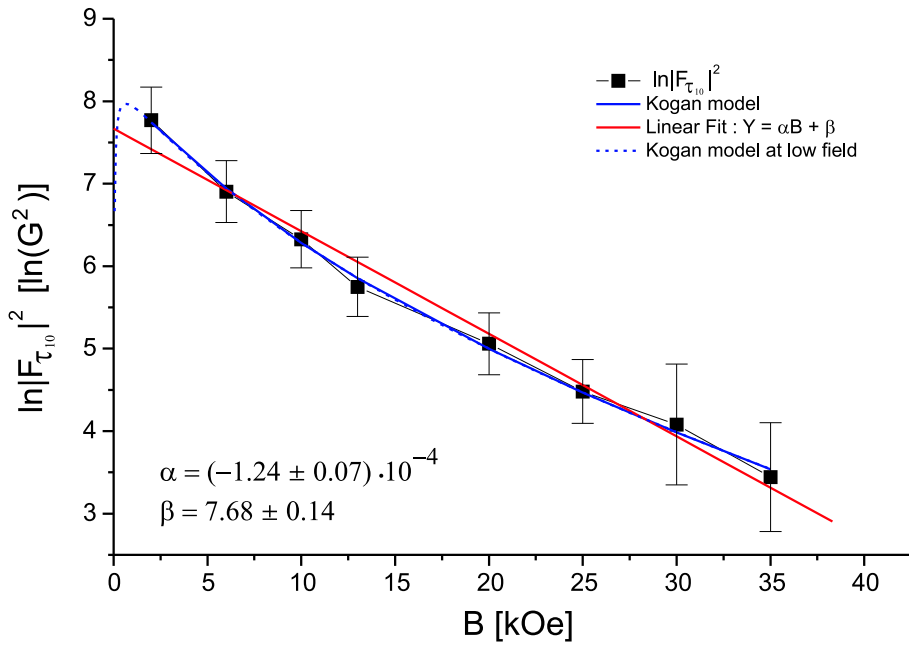
Figure 41. Logarithm of the squared form factor $ln|F_{\tau_{10}}|^2$ of $LuNi_2B_2C$ at $T = 1.9\,K$ plotted as function of the applied field. The data has been reproduced from Eskildsen [8] and the linear fit to the data giving $\alpha = (-1.24 \pm 0.07) \cdot 10^{-4}$ and $\beta = 7.68 \pm 0.14$ is in close agreement with the original fit. A penetration depth $\lambda = \frac{\sqrt{\Phi_0}\exp\left(-\frac{\beta}{4}\right)}{2\pi} = 1061 \pm 37\,\text{Å}$ and a coherence length $\xi = \frac{1}{2\pi}\sqrt{\frac{\Phi_0(-\alpha)}{2c_\xi}} = 82.0 \pm 2.3\,\text{Å}$ is obtained from the linear fit using $c_\xi = \frac{1}{2}$. The data is slightly deviating from a straight line, which is caused by the non-local corrections of the Kogan model. A fit based on the full Kogan model in the form $\ln|F_{\tau_{10}}|^2 = \ln\frac{\bar{B}^2}{\left(1 + p_1\bar{B} + p_2(p_1\bar{B})^2\right)^2} - p_3\bar{B}$ gives a somewhat better fit reproducing the slight curvature and the parameters $p_1 = \frac{(2\pi\lambda)^2}{\Phi_0} = (1.56 \pm 0.11) \cdot 10^{-2}\,G^{-1}$, $p_2 = n_2 + \frac{d}{4} = (8.15 \pm 2.2) \cdot 10^{-3}$ and $p_3 = \frac{2c_\xi(2\pi\xi)^2}{\Phi_0} = (4.01 \pm 0.7) \cdot 10^{-5}\,G^{-1}$. These parameters correspond to a penetration depth $\lambda = 903 \pm 32\,\text{Å}$ and a coherence length $\xi = 46 \pm 4\,\text{Å}$ again using $c_\xi = \frac{1}{2}$.

Reexamination of low temperature data

The SANS data published by Eskildsen *et. al.* [7] was reexamined in the temperature interval $T = 0.5 - 1.6\,K$ at $H = 2.0\,kOe$ and figure 43 show the diffraction pattern at $T = 0.5\,K$ together with the integrated intensity of the (10), (11), (20) and (12) diffraction spots as function of temperature. Numerical integration of the rocking curve as described in section 5.4 was used to obtain the integrated intensities and these were normalized to a monitor count of $N_{monitor} = 10^5$, which is the monitor counting for the $T = 0.5\,K$ diffraction pattern. An increase of the scattering by a factor of almost 2 is seen by lowering the temperature from $T = 1.6\,K$ to $T = 0.5\,K$ in agreement with the trend seen on figure 40. This trend is also seen in the diffractions spots with higher indices and the reflectivity ratio as defined in (227) has been determined from the integrated intensity and is shown in figure 44.

Model comparison

The parameters n_2 and d of the Kogan model depends on averages of the Fermi velocities on the Fermi surface, but neither band structure calculation nor mea-
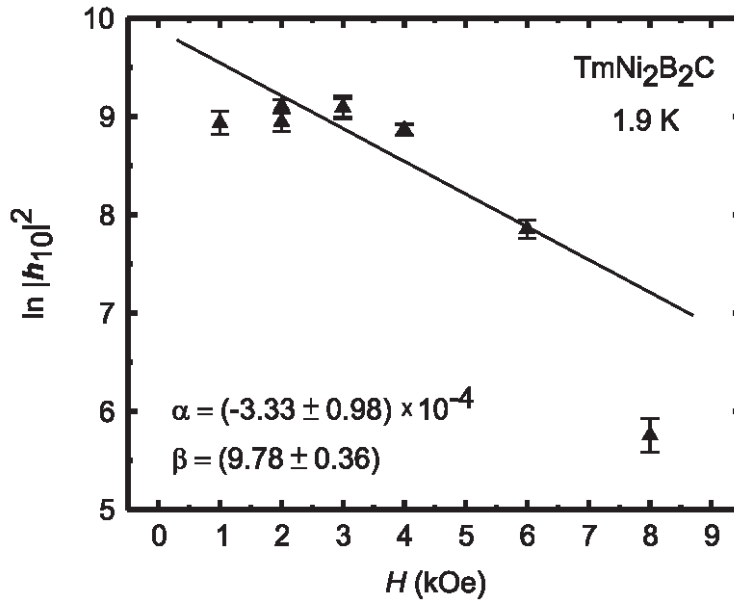
Figure 42. Logarithm of the squared form factor $ln|F_{\tau_{10}}|^2$ of $TmNi_2B_2C$ at $T = 1.9\,K$ plotted as function of the applied field. This plot illustrates that the method for extracting the superconducting length scales from the almost linear field dependence is not working. An attempt to fit a straight line to the data is shown with the corresponding fitting parameters suggesting $\lambda = 613 \pm 58\,\AA$ and $\xi = 132 \pm 21\,\AA$. Taken from Eskildsen [8].
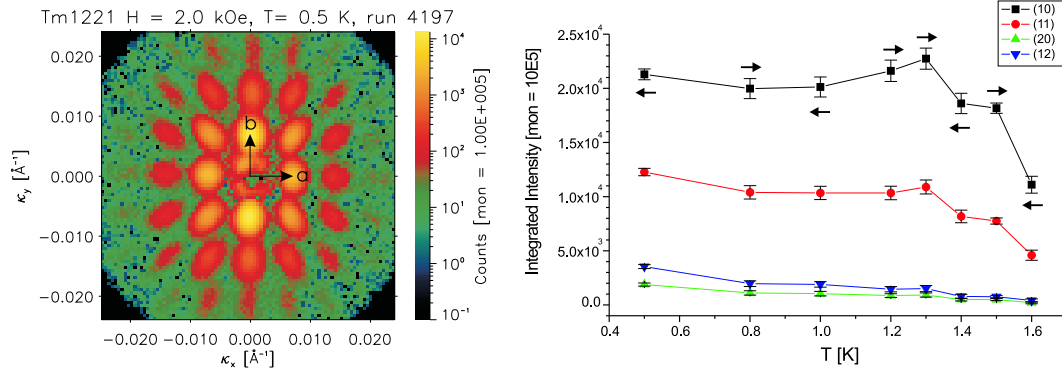

Figure 43. Left: Diffraction pattern from FLL in $TmNi_2B_2C$ obtained by cooling the sample to $T = 0.5\,K$ in an applied field $H = 2\,kOe$ and rocking it with respect to the vertical axis. The FLL unit vectors $\boldsymbol{a}$ and $\boldsymbol{b}$ are directed along the [110] and [1$\bar{1}$0] crystalline directions, whereby the lattice points can be index by $\boldsymbol{\tau} = n_a\boldsymbol{a} + n_b\boldsymbol{b}$ and $\tau = \sqrt{n_a^2 + n_b^2}\tau_{10}$. Right: Integrated intensity of the (10),(11), (12) and (20) diffraction spots normalized to a monitor count of $N_{monitor} = 10^5$ as the magnetic transition at $T_N = 1.5\,K$ is approached. The integrated intensity of the (10) reflection is decreasing by almost a factor of 2 close to the phase transition and reflections with indices higher that (11) becomes very weak. Arrows indicate the temperature history starting with the cooling. Figure 40 showing the (10) intensity was first reported by Eskildsen et. al. [7] and this figure is based on the same data set.
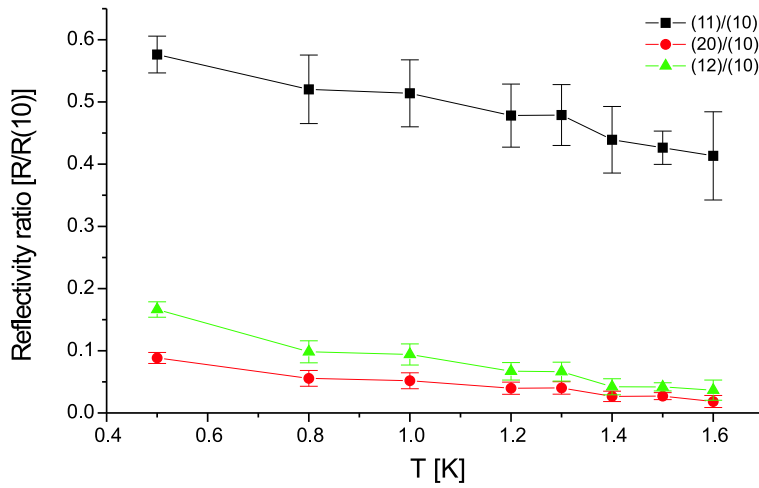
Figure 44. Reflectivity ratio between diffraction spots with index $(n_a n_b)$ and the horizontal unit vector spot with index (10). This ratio depend on the FLL form factor and comparison with the Kogan model can be performed.

surements of the Fermi surface of $TmNi_2B_2C$ are available. In lack of better it is often assumed that the Fermi surface averages are approximately the same for all the borocarbides and one can thereby try to use values obtained from band structure calculations on $LuNi_2B_2C$ as listed in (225).

Figure 45 shows the reflectivity ratio between the (11) and (10) diffraction spots determined from the Kogan model based on the non-local parameters listed in the previous section and for different values of the superconducting length scales given by the penetration depth λ and the coherence length ξ. The open circle marks the reflectivity ratio $\frac{R_{11}}{R_{10}} = 0.13$ expected from the superconducting length scales determined from magnetization measurements by Cho *et. al.* [44], but the SANS measurement gives a ratio of about 0.42 at $T = 1.6\,K$, which is hard to obtain from the model unless the superconducting length scales are changed quite a bit. The measured value can be obtained by setting the coherence length equal to zero as shown by the top curve, and the change of the measured reflectivity ratio from $\frac{R_{11}}{R_{10}} = 0.42 \rightarrow 0.57$ as the temperature is lowered should then be interpreted as an increase of the penetration depth from $\lambda \approx 780\,\AA$ to about $\lambda \approx 1550\,\AA$. However the reflectivity is inversely proportional to λ^4 and an increase of λ by a factor of two should result in a decrease of the scattered intensity by a factor $\frac{1}{2^4} = \frac{1}{16}$, which is contrary to the observed increase of the scattered intensity. The other possibility is to interpret the reflectivity ratio as a dramatic decrease of the penetration depth, which will cause an increased scattered intensity, but this limit seems quite unlikely because it suggest that the superconductor is driven all the way to the border of being a type-II superconductor with $\kappa = \frac{\lambda}{\xi} > \frac{1}{\sqrt{2}}$. This limit also means that the vortex cores are overlapping and the superconductor is not in the intermediate flux line density state, whereby the London approach of the Kogan model is breaking down.

It can be concluded that the reflectivity ratio analysis does not provide a good explanation for the data and the model interpretation resulted in contradicting trends or to a breakdown of the non-local London model.

8.6 Examination of higher order FLL reflections

Finally a SANS experiment at the Paul Scherrer Institute(PSI) was conducted in order to make a comparison between the Kogan model and the intensity of all the
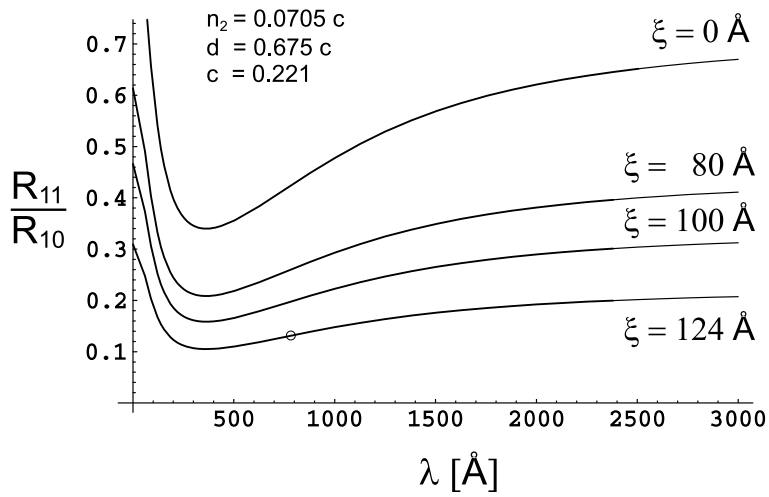
Figure 45. Reflectivity ratio between the (11) and (10) diffraction spots calculated from the Kogan model for different superconducting length scales at a field of $H = 2.0\,kOe$. The open circle indicates the superconducting length scales $\lambda = 780\,\mathring{A}$ and $\xi = 124\,\mathring{A}$ obtained from magnetization measurement by Cho et. al. [44] and the corresponding reflectivity ratio is 0.13. The constant $c_\xi = 1$ has been used in the exponential cut off of the form factor. The choice of the parameters n_2 and d are taken from the bandstructure estimates. In the limit of vanishing non-local corrections ($n_2 = d = 0$) the increase of the reflectivity ratio at high penetration depths is absent with $\frac{R_{11}}{R_{10}} \rightarrow \frac{1}{4}$ for $\lambda \rightarrow \infty$ and $\xi = 0$.

diffraction spots from the FLL observed in the paramagnetic phase at $H = 2.0\,kOe$ and $T = 1.7 - 2.3\,K$. The data was obtained on the same crystal and in the same cryostat used for the AB phase boundary study, since the Risø reactor meanwhile had been shut down permanently and the cryogenics had been moved to PSI.

The diffraction pattern of the FLL was collected at the 18 m SANS at the cold neutron beam guide "1RNR16" of the SINQ spallation neutron source and figure 22 in section 5.4 shows the summed rocking curve obtained in a counting time of about 10 hours. This relatively long counting time ensured that the (22) reflections could be seen with a statistics sufficient to evaluate the reflectivity. The reflectivity of the different diffraction spots were determined by fitting a 2D gaussian function to the diffraction spots of the summed rocking curves and calculating the volume under the peak. This procedure gave equivalent result to the method based on integration of the rocking curves as described previously. An advantage of the peak fitting method is that the position in reciprocal space is determined as well. Figure 46 show the FLL reflectivity of the different diffraction spots as function of the position in reciprocal space at different temperatures for the low temperature data obtained by Eskildsen [8] and the PSI data as well. The flux line form factor can then be calculated and figure 47 shows a comparison with the Kogan model at $T = 2.3\,K$. It should be noted that the wavelength in the Risø experiment has been corrected by 11.5 % due to a misalignment of the velocity selector with respect to the neutron beam. This explains the difference in the determined reciprocal lattice vectors of the Risø and the PSI data.

The calculated values of the Kogan model shown in figure 47 supports the previous conclusion that the superconducting length scales are unusual even in the paramagnetic phase with $\lambda = 340\,\mathring{A}$ indicating that the flux lines are more narrow than expected from magnetization measurements giving $\lambda = 780\,\mathring{A}$. Figure 48 show a comparison of the low temperature Risø data and the PSI data at
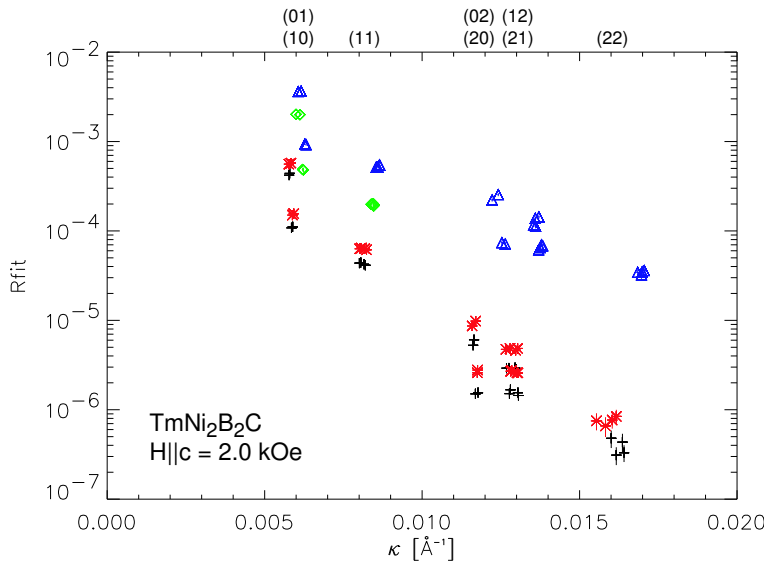
Figure 46. Reflectivity of flux line lattice diffractions spots at $H = 2.0\,kOe$ and different temperatures plotted as function of the magnitude of the reciprocal lattice vectors with the indices shown above the upper axis. The Risø data was obtained at a neutron wavelength $\lambda_n = 11.1\,\mathring{A}$ and temperatures $T = 0.5K(\triangle)$ and $T = 1.6K(\diamondsuit)$, whereas the PSI data was obtained at $\lambda_n = 5.0\,\mathring{A}$ and temperatures $T = 1.7K(\times)$ and $T = 2.3K(+)$. The difference in reflectivity of identical diffraction spots like (10) and (01) is caused be different velocity the lattice vectors are rocked through the Ewalds sphere, and the offset between the Risø and the PSI data comes from the different wavelengths used in the experiments.

$T = 2.3\,K$ in the paramagnetic phase. First of all an increase of the form factor is observed at low temperature, but the decay of the reflectivity in reciprocal space is also slower giving a penetration depth of $\lambda = 290\,\mathring{A}$.

Discussion

The above results are obtained deep down in the superconducting phase and one could question if the extrapolated length scales from the magnetization measurements are appropriate for a comparison. An estimate of the coherence length as function of temperature can be obtained directly from the upper critical field curve

$$\xi(T) = \frac{1}{\sqrt{2\pi}} \sqrt{\frac{\Phi_0}{H_{c2}(T)}} \tag{229}$$

and figure 49 shows the coherence length determined from the transport data by Naugle *et. al.* [37]. The coherence length is diverging near T_c as expected from the Ginzburg-Landau theory and saturates below $T \approx 8\,K$ at $\xi \approx 200\,\mathring{A}$ with small features of the order $\delta\xi \approx 20\,\mathring{A}$ caused by the magnetism. Thus a coherence length at $H = 2.0\,kOe$ and $T = 2.3\,K$ is probably closer to $\xi \approx 200\,\mathring{A}$ than the value from the magnetization measurement, because the superconductor is in the intermediate flux line density state where the vortex cores are not overlapping and is approximately equal to the value found at H_{c2}.

An independent estimate of the penetration depth λ is a bit more tricky and a careful measurement of the lower critical field $H_{c1} = \frac{\Phi_0}{4\pi\lambda^2} \ln\kappa$ would be valuable. However if the two fluid model [19] is assumed more or less valid then the
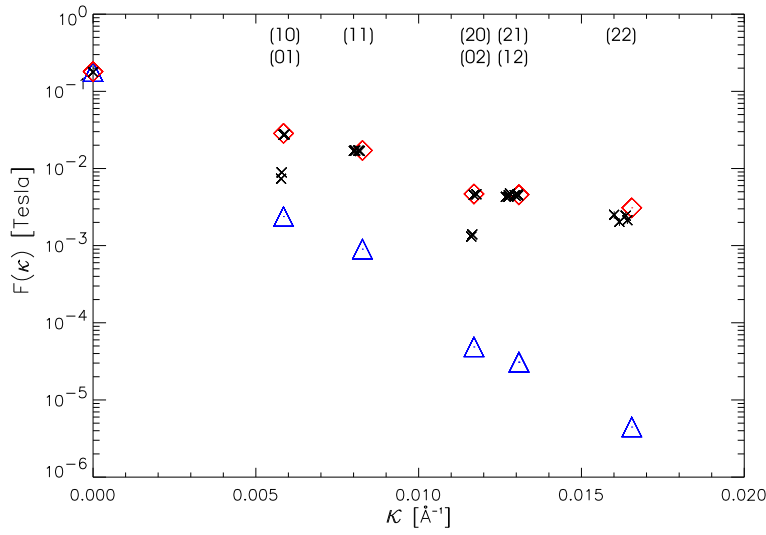
---

[19]Schrieffer [14] p. 12

Figure 47. Flux line form factor obtained from diffraction spots with index (n_a, n_b) of the $H = 2.0\,kOe$ and $T = 2.3\,K$ data from PSI $(\times)$ and corresponding values calculated from the Kogan model with superconducting length scales determined from magnetization measurements $(\triangle)$ and length scales adjusted by hand to match the data $(\lozenge)$. The parameters are $(\triangle)$: $\lambda = 780\,\mathring{A}$, $\xi = 124\,\mathring{A}$, $n_2 = 0.0705c$, $d = 0.675c$, $c = 0.363$. $(\lozenge)$: $\lambda = 340\,\mathring{A}$, $\xi = 0\,\mathring{A}$, $n_2 = 0.0705c$, $d = 0.675c$, $c = 0.221$. The form factor at $\kappa = 0\,\mathring{A}^{-1}$ is equal to the average field $\bar{B}$ in the flux line lattice unit cell, which has been calculated from the reciprocal unit vectors of the diffraction pattern, $\bar{B} = \frac{\Phi_0}{(2\pi)^2}\tau_{10}^2$.
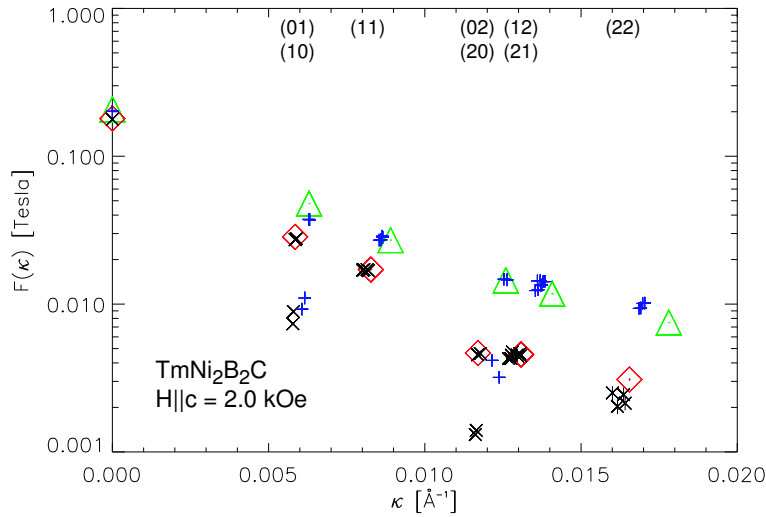
Figure 48. Comparison between experimental flux line form factor in the paramagnetic phase at $T = 2.3\,K\,(\times)$ and in the magnetic ordered phase at $T = 0.5\,K\,(+)$ both for an applied field of $H = 2.0\,kOe$. The corresponding calculated values of the Kogan model found by adjusting the parameters by hand give $(\lozenge)$: $\lambda = 340\,\mathring{A}$, $\xi = 0\,\mathring{A}$, $n_2 = 0.0705c$, $d = 0.675c$, $c = 0.221$ and $(\triangle)$: $\lambda = 290\,\mathring{A}$, $\xi = 0\,\mathring{A}$, $n_2 = d = 0$.
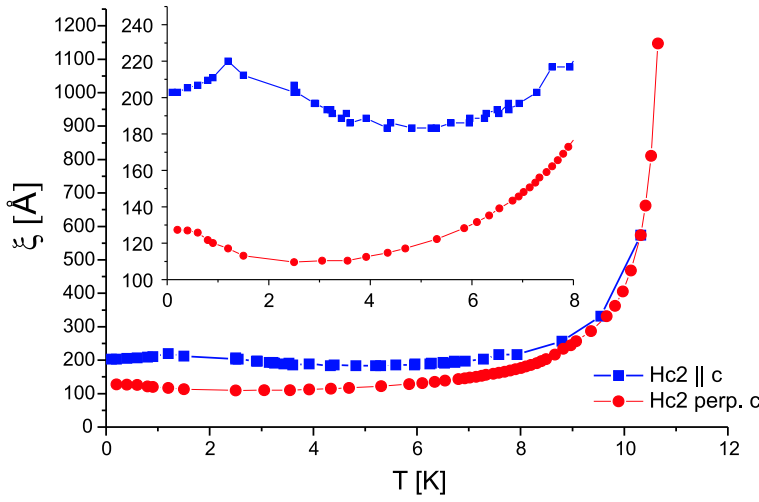
Figure 49. Coherence length $\xi(T)$ of $TmNi_2B_2C$ calculated from the upper critical field curve $H_{c2}(T) = \frac{\Phi_0}{2\pi\xi(T)^2}$ measured by Naugle et. al. [37]. The insert shows the low temperature part of the curves with a clear feature at the Néel temperature $T_N = 1.5\,K$.

temperature dependence of the penetration depth should be

$$\lambda(T) = \frac{\lambda(0)}{\sqrt{1 - \left(\frac{T}{T_c}\right)^4}} \tag{230}$$

and $\frac{\lambda(T)}{\lambda(0)} < 1.17$ for $T < 8\,K$.

A relevant question is how the penetration depth is changed by the susceptibility χ of the Tm ions and a naive answer can be obtained by re-deriving the London equation using the constitutive relation $\boldsymbol{B} = \boldsymbol{H} + 4\pi\boldsymbol{M} = (1 + 4\pi\chi)\boldsymbol{H}$. The basic London equation gives the relation between supercurrent and vector potential

$$\boldsymbol{j} = -\frac{1}{\Lambda^2}\boldsymbol{A} \tag{231}$$

By taking the curl of this and substitute the constitutive equation for $\boldsymbol{B}$ one gets

$$\nabla \times \boldsymbol{j} = -\frac{1}{\Lambda^2}\nabla \times \boldsymbol{A} = -\frac{1}{\Lambda^2}\boldsymbol{B} = -\frac{1}{\Lambda^2}(1 + 4\pi\chi)\boldsymbol{H} \tag{232}$$

From the Maxwell equation $\frac{4\pi}{c}\boldsymbol{j} = \nabla \times \boldsymbol{H}$ a differential equation expressed for the field is obtained

$$\nabla \times \nabla \times \boldsymbol{H} = \nabla(\nabla \cdot \boldsymbol{H}) - \nabla^2\boldsymbol{H} = -\frac{4\pi}{c\Lambda^2}(1 + 4\pi\chi)\boldsymbol{H} \tag{233}$$

Here the factor on the right hand side is defining a length scale

$$\lambda_e = \frac{\lambda}{\sqrt{1 + 4\pi\chi}} \tag{234}$$

which is proportional to the usual penetration depth $\lambda^2 = \frac{c\Lambda^2}{4\pi}$, but re-normalized by the susceptibility. An interpretation of the above is the that it takes less supercurrent to make a quantum of flux due to the field enhancement by the

Tm ions and the length scale of the field decay given by the penetration depth thereby becomes smaller. There is just a problem with the derivation above, because the term $\nabla(\nabla \cdot \boldsymbol{H})$ is only zero in absence of the susceptibility since $\nabla \cdot \boldsymbol{H} = \nabla \cdot \boldsymbol{B} - 4\pi\nabla \cdot \boldsymbol{M} = -4\pi\nabla \cdot \boldsymbol{M} = -4\pi\nabla \cdot \chi\boldsymbol{H}$. Thus the London equation must be replaced by a more complicated expression.

A full blown analysis of the penetration depth re-normalization in magnetic superconductors has been given by Bulaevskii et. al. by starting from microscopic equations and including both the RKKY exchange- and dipole-dipole interaction between localized moments [75]. They determine a scaling factor p which must be multiplied onto the penetration depth $\lambda_e = \lambda\sqrt{p}$ with

$$p = 1 - \frac{\Theta_{em}}{\Theta_{em} + \Theta_{ex} + \frac{\tilde{\mu}^2}{\mu^2\chi_m}} \tag{235}$$

Here Θ_{ex} is the RKKY contribution to the Néel temperature and depends on the electronic susceptibility χ_e and the magnitude of the exchange field h_0 by $\Theta_{ex} = \chi_e(0)h_0^2$. The contribution to the ordering temperature from the dipole-dipole interaction is characterized by $\Theta_{em} = 2\pi n\mu^2$, with n being the concentration of local moments (Tm-ions) and $\mu = g\mu_B <J_z>_{T=0}$ is the average size of the moments. The susceptibility is given by a Curie-Weiss form

$$\chi_m = \frac{\tilde{\mu}^2}{T - \Theta} \tag{236}$$

with the Curie constant $\tilde{\mu}^2$ and Weiss temperature Θ.

Thus when the temperature is far above the Weiss temperature $T \gg \Theta$ the penetration depth is unchanged $p \to 1$, but as the magnetic transition is approached the penetration depth will decrease. Kulic et. al. [76] has evaluated the magnetization data on $TmNi_2B_2C$ by Cho et. al. [44] and the exchange coupling is dominating with the energy scale of the coupling given by $h_0 = 60K$ and the contribution to the ordering temperature $\Theta_{ex} \approx 1K$, which is of the same order as the electromagnetic contribution $\Theta_{em} \approx 2K$. The susceptibility of $TmNi_2B_2C$ reaches the maximum at the magnetic ordering temperature $\Theta = -T_N \approx -1.5K$ and by inserting these values in the equation for p one gets

$$\sqrt{p} = \sqrt{1 - \frac{2\,K}{2\,K + 1\,K + 1.5\,K - (-1.5\,K)}} = 0.82 \tag{237}$$

In the extreme limit one could assumed that $TmNi_2B_2C$ would order ferro-magnetically whereby the susceptibility would diverge at the ordering temperature and

$$\sqrt{p} = \sqrt{1 - \frac{2\,K}{2\,K + 1\,K}} = 0.58 \tag{238}$$

Thus from the penetration depth $\lambda = 903\,\mathring{A}$ of the non-magnetic $LuNi_2B_2C$ one gets $\lambda_e = 521 - 737\,\mathring{A}$. Kulic et. al. reaches the conclusion that $\xi_0 = 250\,\mathring{A}$ and $\lambda = 500\,\mathring{A}$ by stating that the sample used by Cho et. al. was in the dirty limit with a mean free path of $l = 50\,\mathring{A}$.

It can now be concluded that a decrease of the penetration depth is expected as the magnetic transition is approached due to the presence of the Tm ions, but the measured penetration depth still seems to be too small compared to the estimates made above. Also the susceptibility should decrease considerably as soon as the antiferromagnetic ordering is building up below the Néel temperature [20]

---

[20]Yosida [77] chapter 6

and a decrease of the neutron intensity would be expected, which is not what is observed in figure 43.

All in all the number of neutrons scattered from the sample in the paramagnetic phase seems to be to large to be coming from flux lines and only one length scale somewhat larger than the core size is involved. However the periodicity of the structure giving the scattering is dictated by the square flux line lattice. In the catalog of objects able to scatter neutron there are two options left : the magnetic moments of the Tm-ions or the nucleus in the sample.

The flux line lattice result in a modulated magnetic flux density inside the sample and the magnetization of the Tm ions will follow this, but the length scale for the modulation should be the penetration depth, which is again too large to explain the observed data.

The second option that extra scattering is coming from the nucleus could in principle be explained by some magneto-elastic effect, causing the crystallographic lattice constants to change slightly at the flux line center due to a higher magnetic field compared to the average magnetic flux density in the sample. However this explanation seems a bit unrealistic, but could be checked in a high resolution synchrotron experiment.

A third explanation can be offered by considering the interaction between the RKKY coupling mechanism and superconductivity in more detail. The basic idea is that superconductivity changes the RKKY interaction between the Tm-ions and one could therefore imagine that the coupling between the ions is different inside the vortex cores compared to outside in the superconducting phase with a full orderparameter. Thus a different type of magnetism is suggested to exist inside the vortex cores and will be outlined in the following section.

8.7 Magnetism in vortex cores

Anderson and Suhl were the first to address the question of how the superconducting phase would influence the RKKY interaction in a magnetic superconductor [78]. Their conclusion was that the opening of the superconducting gap would remove the contributions to the electronic susceptibility χ_e at long wavelengths smaller than the inverse of the coherence length, $q < \frac{1}{\xi_0}$. From equation (192) of the electronic susceptibility

$$\chi(\boldsymbol{q}) = \sum_{n,m,\boldsymbol{k}} \frac{f[\epsilon_m(\boldsymbol{k})]\{1 - f[\epsilon_n(\boldsymbol{k} + \boldsymbol{q})]\}}{\epsilon_n(\boldsymbol{k} + \boldsymbol{q}) - \epsilon_m(\boldsymbol{k})} \tag{239}$$

this result can be understood qualitatively since the large contribution from states around the Fermi level comes from the denominator going towards zero, which is prevented in the superconding state by the gap. Figure 50 shows a plot of the susceptibility in the normal and superconducting state as derived by Anderson and Suhl.

This Anderson Suhl mechanism has been suggested by Kulic *et. al.* [76] to stabilize the long wavelength antiferromagnetic phase below T_N and the wavevector $q_{mI} = [0.094, 0.094, 0]a^*$ should correspond to the maximum of the electronic susceptibility in figure 50. A consequence of this assumption is that $TmNi_2B_2C$ should order ferromagnetically if superconductivity was suppressed by applying a field along the a-axis perpendicular to the Tm moment. This was however not observed and a new spin density wave with $q_A = [0.48, 0, 0]a^*$ close to an ordinary anti-ferromagnetic ordering was found for $H \| a > 1\,Tesla$ by Nørgaard *et. al.* [79] presenting the idea that a total energy balance between the RKKY magnetism and the condensation energy of the superconducting state must be considered. Buzdin has subsequently presented similar arguments suggesting that q_A is connected to

a local maximum in the susceptibility caused by Fermi surface nesting, which is suppressed by the superconducting phase [67] p. 303.
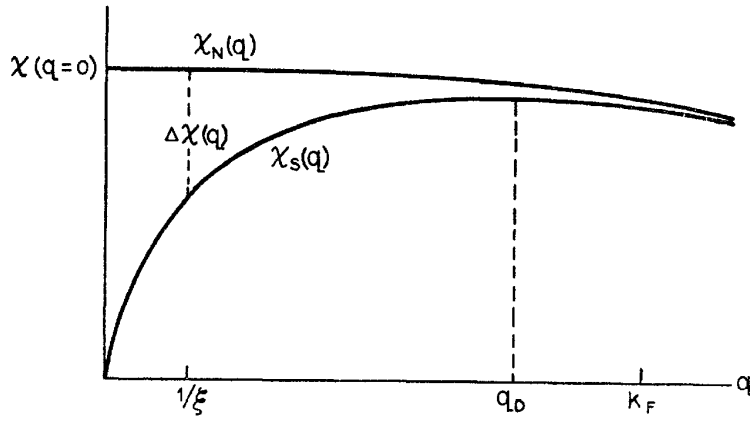

Figure 50. Difference between the electronic susceptibility of a RKKY coupled magnetic superconductor in the normal and superconducting state. The superconducting gap suppresses the susceptibility at small wavelengths $q < \frac{1}{\xi_0}$ and a spin density wave with a wavevector corresponding to the maximum of the susceptibility should appear in the superconducting phase. Taken from Anderson et. al. [78].

The Anderson Suhl calculation is based on the assumption that the system is homogeneous and the modulation due to the flux line lattice is neglected. The idea of having a different RKKY coupling represented by the normal curve of figure 50 inside the vortex cores compared to the superconducting curve outside the vortex core has been investigated theoretically in the case of $TmNi_2B_2C$ by Thorsten Hansen [80]. The main conclusion by Hansen is a suggestion that the vortex cores might expand, because the Tm ions in the cores are easier polarized by the applied field compared to Tm ions outside of the cores and a corresponding minimization of the total energy of the system results from the expanded cores.

Neutron scattering from Tm moments modulated by the FLL periodicity

In order to examine the idea of magnetism in the vortex cores the neutrons scattering cross section of such a structure will be calculated and compared with the SANS data. The first case to study is the paramagnetic superconducting phase and the scattering cross section of a paramagnet consisting of uncoupled moments can be taken from any textbook on neutron scattering. Here an expression for the elastic scattering cross section of a paramagnet in an applied field along the z-direction is adopted from Squires [25] chapter 7.6

$$
\begin{aligned}
\frac{d\sigma}{d\Omega} =\ & (\gamma r_0)^2 N \left\{ \frac{1}{2} g F(\boldsymbol{\kappa}) \right\}^2 \exp(-2W) \Bigg[(1 - \hat{\kappa}_z^2) \frac{(2\pi)^3}{v_0} < \boldsymbol{S}^z >^2 \sum_{\boldsymbol{\tau}} \delta(\boldsymbol{\kappa} - \boldsymbol{\tau}) \\
& + \hat{\kappa}_z^2 \left\{ \frac{1}{2} \boldsymbol{S}(\boldsymbol{S}+1) - \frac{3}{2} < (\boldsymbol{S}^z)^2 > + < \boldsymbol{S}^z >^2 \right\} + \frac{1}{2} \boldsymbol{S}(\boldsymbol{S}+1) + \frac{1}{2} < (\boldsymbol{S}^z)^2 > - < \boldsymbol{S}^z >^2 \Bigg]
\end{aligned}
$$

$$(240)$$

with

- $(\gamma r_0)^2$: The product of the gyromagnetic ratio $\gamma = 1.913$ and the classical electron radius $r_0 = \frac{\mu_0}{4\pi}\frac{e^2}{m_e} = 2.815 \cdot 10^{-15}\, m$ setting the magnitude of the scattering cross section $(\gamma r_0)^2 = 0.29\, barn$.

- N : The number of moment in the scattering system.

- $\left\{\frac{1}{2}gF(\boldsymbol{\kappa})\right\}^2$: The Landé splitting factor g when the ions have both spin and orbital angular momentum. $F(\boldsymbol{\kappa})$ is the magnetic form factor which is basically the Fourier transform of the density of unpaired electrons around the ion.

- $\exp(-2W)$: The Debye-Waller factor connected to the average square displacement $< u^2 >$ of the ions due to thermal fluctuations, $2W \approx \frac{1}{3} < u^2 > \kappa^2$.

- $(1 - \hat{\kappa}_z^2)$: A geometric factor depending on the unit vector along the momentum transfer $\hat{\boldsymbol{\kappa}} = (\hat{\kappa}_x, \hat{\kappa}_y, \hat{\kappa}_z)$. Thus if the momentum transfer is along the z-axis the scattering will vanish.

- v_0 : Volume of the unit cell.

- $< \boldsymbol{S}^z >$: Thermal average of the z-component of the total angular momentum operator which is given by the Brillouin-function $< \boldsymbol{S}^z >= (\boldsymbol{S} + \frac{1}{2})\coth(\boldsymbol{S} + \frac{1}{2})u - \frac{1}{2}\coth(\frac{1}{2}u)$ with $u = \frac{g\mu_B B}{k_B T}$ being the the ratio between the dipole interaction energy and the thermal energy.

- $< (\boldsymbol{S}^z)^2 >$: Thermal average of squared z-component of the total angular momentum operator.

- $\sum_{\boldsymbol{\tau}} \delta(\boldsymbol{\kappa} - \boldsymbol{\tau})$: Sum over the reciprocal lattice vectors of the crystalline unit cell of the magnetic ions.

What is learned from the above is that a magnetic field will cause the moments to precess with respect to the field direction and the thermal average $< \boldsymbol{S}^z >$ will attain a finite value if the temperature is sufficiently small. This will cause extra scattering on the crystalline Bragg reflection due to the sum over the δ-function of the reciprocal lattice vectors. The lower line of equation (240) describes scattering which is spread out in reciprocal space and will cause a diffuse background.

In the equation above it was assumed that all the moments attain the same magnitude and what is needed is an expression in which the moments can be modulated. This can be done by introducing a large unit cell defined from the flux line lattice unit cell with one flux line sitting in each corner and a lot of Tm ions inside as illustrated on figure 51. The sharp parenthesis of equation (240) must be replaced by a more general expression [21]

$$\frac{d\sigma}{d\Omega} = (\gamma r_0)^2 \left\{\frac{1}{2}gF(\boldsymbol{\kappa})\right\}^2 \exp(-2W) \sum_{\alpha\beta}(\delta_{\alpha\beta} - \hat{\kappa}_\alpha\hat{\kappa}_\beta) \sum_{\boldsymbol{ll'}} \exp(i\boldsymbol{\kappa}\cdot(\boldsymbol{l}-\boldsymbol{l'})) < S_l^\alpha >< S_{l'}^\beta >$$

(241)

where $\alpha, \beta = x, y, z$ are axis indices of the momentum transfer vector and the sum over $\boldsymbol{l}$ includes all lattice positions of the moment with $< S_l^\alpha >$. By assuming that the moments all align along the field direction z then

$$< S_l^\alpha >< S_{l'}^\beta >= \delta_{\alpha z} < S_l^z > \delta_{\beta z} < S_{l'}^z >$$

(242)

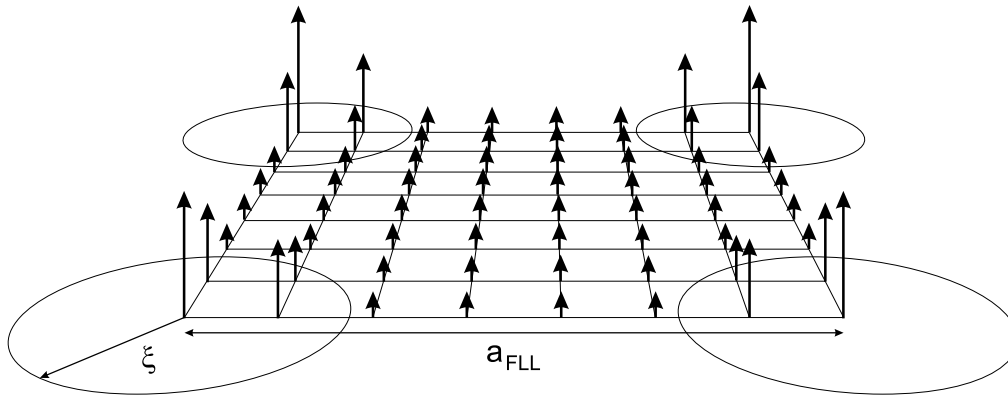and the sum over axis indices reduces to

---
[21]Squires [25] p. 153

Figure 51. Magnetic flux line lattice of $TmNi_2B_2C$ with the Tm moments illustrated by arrows, which are directed along the crystalline c-axis and the applied field. The magnitude of the moments are larger inside the vortex cores of a size given by the coherence length ξ and the area of the unit cell is identical to the area of the flux line lattice $A_u = a_{FLL}^2 = \frac{\Phi_0}{B}$. The two edges of the unit cell correspond to the crystalline (110) direction and every second Tm moment is positioned at the body center $(\frac{1}{2}\frac{1}{2}\frac{1}{2})$ of the crystalline unit cell, but for scattering vectors in the ab-plane the z coordinate has no influence on the scattering. A separation of $a_{Tm} = \frac{a}{\sqrt{2}} = 2.47\,\text{Å}$ between the Tm ions can be compared to the length scales involved : $\frac{\xi}{a_{Tm}} = \frac{200\,\text{Å}}{a_{Tm}} = 81$, $\frac{\lambda}{a_{Tm}} = \frac{600\,\text{Å}}{a_{Tm}} = 243$ and $\frac{a_{FLL}}{a_{Tm}} = \frac{1017\,\text{Å}}{a_{Tm}} = 412$. Thus a large number of Tm ions are present in the unit cell at $H = 2.0\,kOe$. The volume of the unit cell is given by the product of the flux line lattice unit cell and the height of the crystalline unit cell, $v_u = A_u c$

$$\sum_{\alpha\beta}(\delta_{\alpha\beta}-\hat{\kappa}_\alpha\hat{\kappa}_\beta)\sum_{ll'}\exp\left(i\boldsymbol{\kappa}\cdot(\boldsymbol{l}-\boldsymbol{l}')\right) <S_l^\alpha><S_{l'}^\beta> = (1-\hat{\kappa}_z^2)\sum_{ll'}\exp\left(i\boldsymbol{\kappa}\cdot(\boldsymbol{l}-\boldsymbol{l}')\right)<S_l^z><S_{l'}^z>$$

$$(243)$$

Now the sum over all the lattice positions is split up into a sum over the moments at $\boldsymbol{d}$ inside each flux line lattice unit cell and a sum over all the flux line lattice unit cells with lattice vectors $\boldsymbol{r}$ whereby $\boldsymbol{l} = \boldsymbol{r} + \boldsymbol{d}$

$$(1-\hat{\kappa}_z^2)\sum_{\substack{rr'\\dd'}}\exp\left(i\boldsymbol{\kappa}\cdot(\boldsymbol{r}+\boldsymbol{d}-\boldsymbol{r}'-\boldsymbol{d}')\right)<S_{r+d}^z><S_{r'+d'}^z>$$

$$= (1-\hat{\kappa}_z^2)\sum_{rr'}\exp\left(i\boldsymbol{\kappa}\cdot(\boldsymbol{r}-\boldsymbol{r}')\right)\sum_{dd'}<S_d^z><S_{d'}^z>\exp\left(i\boldsymbol{\kappa}\cdot(\boldsymbol{d}-\boldsymbol{d}')\right)$$

$$= (1-\hat{\kappa}_z^2)\sum_{rr'}\exp\left(i\boldsymbol{\kappa}\cdot(\boldsymbol{r}-\boldsymbol{r}')\right)\left|\sum_{d}<S_d^z>\exp\left(i\boldsymbol{\kappa}\cdot\boldsymbol{d}\right)\right|^2$$

$$= (1-\hat{\kappa}_z^2)N_u\frac{(2\pi)^3}{v_u}\sum_{\tau_u}F_{magFLL}(\boldsymbol{\kappa})^2\delta(\boldsymbol{\kappa}-\boldsymbol{\tau_u}) \qquad (244)$$

Here N_u is the number of magnetic flux line lattice unit cells with a volume given by the product of the area of the flux line lattice unit cell $A_u = \frac{\Phi_0}{B}$ and the crystalline c-axis, $v_u = A_u c$. F_{magFLL} is the magnetic structure factor of the large unit cell

$$F_{magFLL}(\boldsymbol{\kappa}) = \sum_{\boldsymbol{d}} < S^z_{\boldsymbol{d}} > \exp\left(i\boldsymbol{\kappa} \cdot \boldsymbol{d}\right) \tag{245}$$

and determines the interference of the scattering coming from each magnetic flux line unit cell at momentum transfer vectors equal to the reciprocal lattice vectors of the magnetic flux line lattice $\boldsymbol{\tau}_u$. The sum is over all moments $< S^z_{\boldsymbol{d}} >$ at the positions $\boldsymbol{d}$ in the large unit cell.

Thus the scattering cross section of the magnetic flux line lattice becomes

$$\frac{d\sigma}{d\Omega} = (\gamma r_0)^2 \left\{ \frac{1}{2} g F(\boldsymbol{\kappa}) \right\}^2 \exp\left(-2W\right)(1 - \hat{\kappa}_z^2) V \frac{(2\pi)^3}{v_u^2} \sum_{\boldsymbol{\tau}_u} F_{magFLL}(\boldsymbol{\kappa})^2 \delta(\boldsymbol{\kappa} - \boldsymbol{\tau}_u) \tag{246}$$

where the volume of the sample has been introduced $V = N_u v_u$.

Once an equation for the cross section is established the reflectivity can be calculated in a way similar to what was done for the flux line lattice as outlined in section 5.3

$$R = \frac{P}{\phi A_s}$$

$$= \frac{\lambda_n^2}{(2\pi)^2 \tau \cos\left(\eta_\tau\right)} (\gamma r_0)^2 \left\{ \frac{1}{2} g F(\boldsymbol{\kappa}) \right\}^2 \exp\left(-2W\right)(1 - \hat{\kappa}_z^2) V \frac{(2\pi)^3}{v_u^2} F_{magFLL}(\boldsymbol{\tau}_u)^2 \tag{247}$$

There are still some parameters in the equation above which remain to be defined and several can be neglected. Both the magnetic formfactor of the Tm ions $F(\kappa)$ and the Debye-Waller factors will be close to unity in the small angle range of the momentum transfer ($\kappa \ll a^*$) and for scattering vectors in the ab-plane the factor $1 - \hat{\kappa}_z^2 = 1$. The Landé splitting factor can be found from Hund's rules giving $g = \frac{7}{6}$ while the modulated moment $< S^z >$ in Bohr magnetons can be considered as a fitting parameter.

Comparison with SANS data

Figure 52 shows the square of the magnetic flux line lattice structure factor determined from the measured reflectivity of the diffraction spots from $TmNi_2B_2C$ at $H = 2.0\,kOe$ and $T = 2.3\,K$ and calculated values by assuming that the moment modulation can be described by a gaussian function positioned at each flux line

$$< S^z > (\boldsymbol{r}) = A_1 \exp\left(-\frac{(\boldsymbol{r} - \boldsymbol{r}_i)^2}{2\sigma^2}\right) + A_0 \tag{248}$$

It is only the modulation A_1 and σ which result in small angle neutron scattering, because the cross section of scattering on magnetic structures is given by the Fourier transform of the magnetic correlation function, whereas A_0 has no influence. The parameters used in the model calculations were adjusted by hand to match the data and a gaussian width $\sigma = 150\,\mathring{A}$ was found. As shown in appendix C this width correspond to a coherence length of $\xi = \sqrt{3\ln 2}\sigma = 216\,\mathring{A}$, which is in good agreement with the coherence length found from the H_{c2} curve and shown in figure 49. The magnitude of the moment modulation is found to be $A_1 = 0.11\mu_B$ and the corresponding field modulation can be calculated by $\delta B = 4\pi n\mu = 4\pi\,1.55 \cdot 10^{22}\,cm^{-3}\,0.11\mu_B = 199\,Oe$ where n is the density of Tm

ions. Thus the modulation is of about 10% of the applied field. One can calculate the magnetic flux associated with the modulation of the Tm ions by determining the volume V_g under the gaussian peak given by $V_g = 2\pi\sigma^2 A_1$. By substituting A_1 with the field modulation δB gives the magnetic flux Φ

$$\Phi = 2\pi\sigma^2\delta B = 2\pi(150\cdot10^{-10}\,m)^2 1.99\cdot10^{-2}\,T = 2.81\cdot10^{-17}\,Tm^2 = 1.36\cdot10^{-2}\Phi_0$$

(249)

which is 1.36 % of a flux quantum.
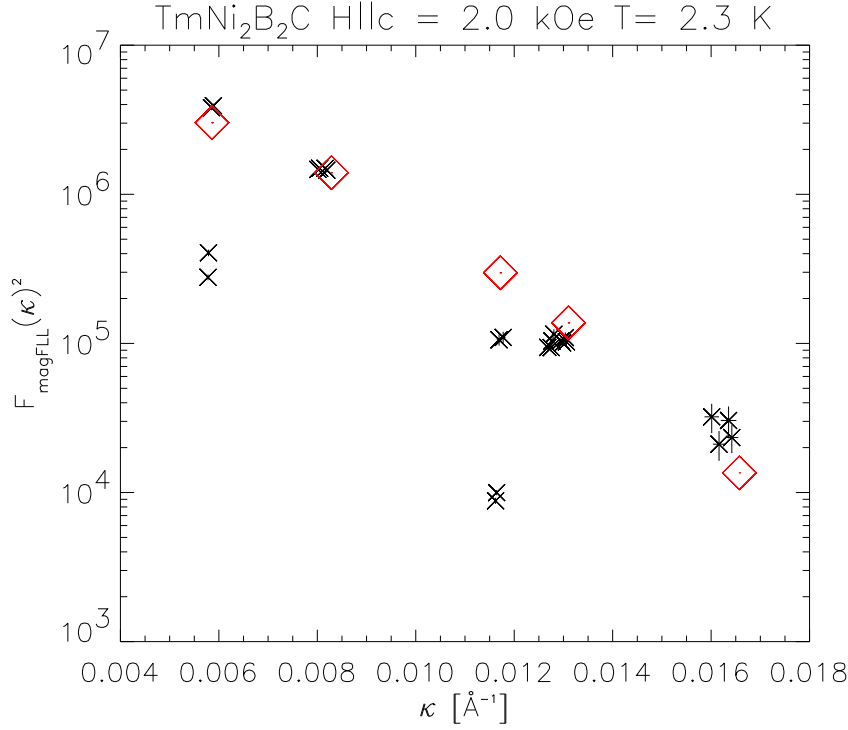
Figure 52. Comparison of structure factor of magnetic flux line lattice determined from the SANS reflectivity ($\times$) of $TmNi_2B_2C$ at $H||c = 2.0\,kOe$, $T = 2.3\,K$ and a model calculation ($\diamondsuit$) based on a gaussian description of the moment modulation $<S^z>(r) = A_1\exp\left(-\frac{r^2}{2\sigma^2}\right) + A_0$ with the parameters : $A_0 = 1.0\mu_B$, $A_1 = 0.11\mu_B$ and $\sigma = 150\,\mathring{A}$ corresponding to a coherence length $\xi = \sqrt{3\ln 2}\sigma = 216\,\mathring{A}$ as described in appendix c. It should be noted that the average magnetic flux density in the sample is $\bar{B} = 1.8\,kOe$, which is smaller than the applied field and is probably caused by the diamagnetic response of a Type-II superconductor.

Figure 53 shows the analysis of the magnetic flux line lattice structure factor at $H = 2.0\,kOe$ and $T = 0.5\,K$ in the magnetically ordered phase. The obtained estimate of the magnetic core size is $\xi = 158\,\mathring{A}$, which is somewhat expected because the upper critical field is increasing as the temperature is decreased below T_N. More than a doubling of the moment modulation is found with $A_1 = 0.23\mu_B$, but the previous picture of the moment modulation in the paramagnetic phase might not be appropriate. However one could argue that the spin density wave is also modulated by the flux line lattice and the alternating direction of the Tm moments basically gives a doubling of the modulation amplitude as illustrated on figure 54. This would offer an qualitative explanation for the increased small angle

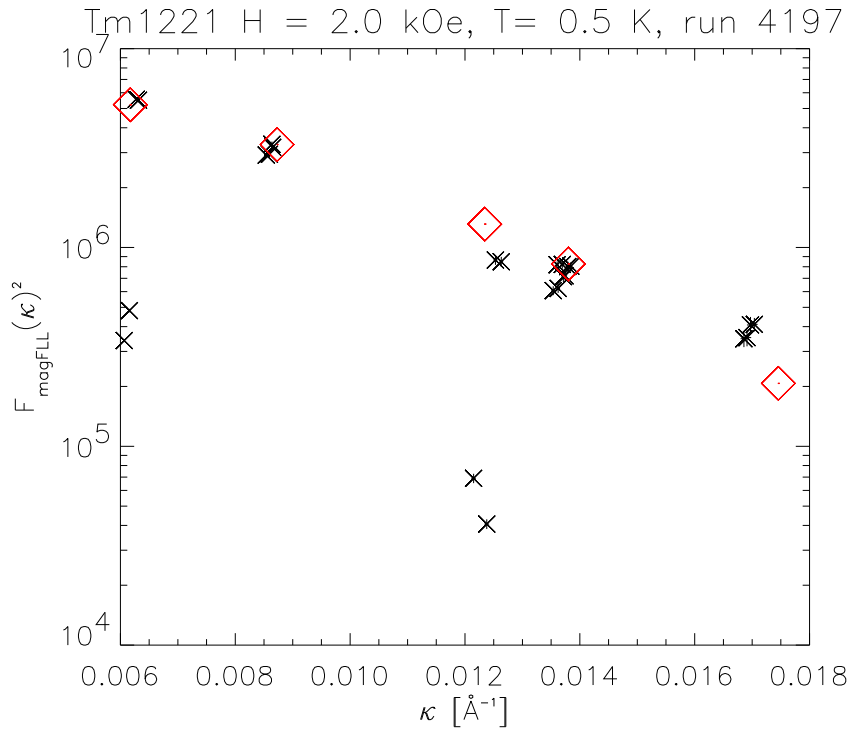scattering as the temperature is lowered below the Néel temperature as shown on figure 43.

Figure 53. Structure factor of magnetic flux line lattice determined from the SANS reflectivity ($\times$) of $TmNi_2B_2C$ at $H||c = 2.0\,kOe$ below the Néel temperature at $T = 0.5\,K$ and a the gaussian model calculation ($\diamond$) with the parameters : $A_0 = 1.0\mu_B$, $A_1 = 0.23\mu_B$ and $\sigma = 110\,\text{Å}$ corresponding to a coherence length $\xi = \sqrt{3\ln 2}\sigma = 158\,\text{Å}$.

A qualitative argument for the peak in the scattered intensity as function of field in the antiferromagnetic phase, as shown on figure 40, can be given by assuming that the core volume is constant at low and intermediate flux line densities when the temperature is constant. The scattered intensity per unit cell will then be proportional to the ratio between the area of the core and the area of the flux line lattice unit cell

$$I \sim \frac{\xi^2}{a_{FLL}^2} = \frac{\xi^2}{\Phi_0}\bar{B} \tag{250}$$

which shows that the intensity should scale linearly with the average magnetic flux density $\bar{B}$ at low applied fields. However at the crossover from the intermediate to the high flux line density phase the vortex cores start to overlap and the magnetic modulation will be suppressed causing the scattered intensity to decrease again as shown on the insert of figure 40.

This crossover from intermediate to high flux line density can also explain the fast decrease to the reflectivity at high applied field in the paramagnetic phase as shown on figure 42.

Finally is it interesting to ask how the scattering from the modulated flux line lattice should change if the magnetic field is applied in the *ab*-plane. Due to the Ising like character of the magnetic system with the easy axis of the Tm-ions being along the crystalline *c*-axis no large change of the magnetic ordering is expected in
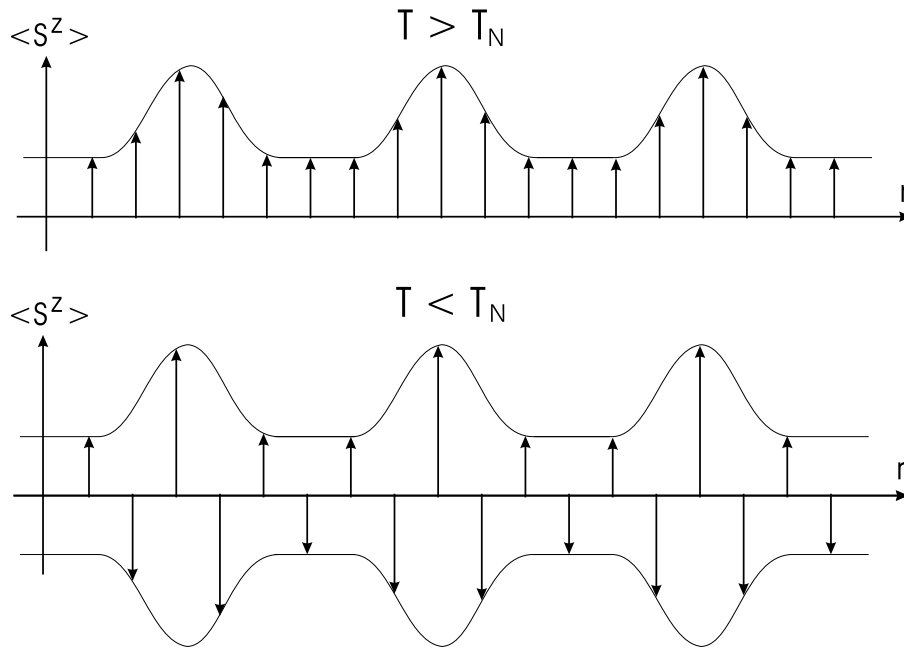
Figure 54. Qualitative picture of the paramagnetic phase ($T > T_N$) and the spin density wave ($T < T_N$) modulated by the flux line lattice due to the difference in the RKKY interaction inside and outside the vortex core.

this geometry. Indeed this is also what has been observed by Nørgaard *et. al.* [79] where the field induced magnetic phase with ordering vector $q_A = [0.48, 0, 0]a^*$ still have the moment along the crystalline *c*-axis. The geometric factor $1 - \hat{\kappa}_z^2$ can now become zero if the momentum transfer vector is parallel with the direction of the moments and the scattering should vanish for certain reflections. In the following section an experiment with the applied field in the *ab*-plane is described.

8.8 Flux line lattice for $H\|[110]$

A study of the flux line lattice induced by an applied field along the crystalline (110) direction was conducted at Risø in order to study the interaction of the field induced magnetic q_A phase observed by Nørgaard *et. al.* [79]. At the time of the experiment many of the observations were hard to understand, but a reinterpretation in the light of the idea of magnetism in the vortex cores is appropriate.

Figure 55 show the composite sample consisting of 6 bars cut from the same $TmNi_2B_2C$ single crystal and mounted on a cadmium plate with the crystalline *c*-axis perpendicular to the incoming neutron beam and in the horizontal plane of the SANS camera. The reason for mounting several crystals was to get a higher signal, but this excludes the possibility to obtain the reflectivity on an absolute scale because some of the direct beam is passing through the pinhole without hitting the sample bars.

The sample was cooled to temperatures between $T = 1.7 - 4\,K$ in applied fields between $H = 2 - 15\,kOe$ along the crystalline (110) direction and along the neutron beam of the SANS camera in the cold neutron guide hall of the Risø DR3 reactor. The settings of the SANS were : $\lambda_n = 6.75\,\mathring{A}$, $\frac{\Delta\lambda}{\lambda} = 0.18$, pinhole1 = 2.5 cm diameter, pinhole2 = 8 mm × 5.0 mm, collimation L = 6 m and detector distance l = 6 m.

A large number of difficulties were encountered during this experiment and the first was to find the flux line lattice by rocking the sample around the vertical
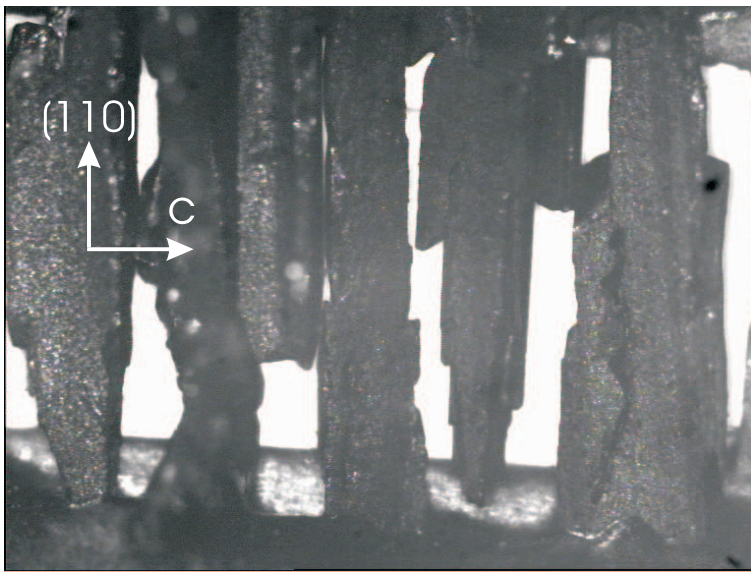
Figure 55. Composite $TmNi_2B_2C$ *sample consisting of 6 bars mounted with the crystalline c-axis perpendicular to the neutron beam and in the horizontal plane of the SANS camera. An x-ray Laue camera was used to align the crystallographic axis of the different bars within* 1°. *The pinhole of the cadmium plate behind the bars is approximately 5mm x 8mm.*

axis. Two strong reflections on the vertical axis were easily seen, but the remaining reflections had very broad and ill defined rocking curves. A hexagonal flux line lattice was found by rotating the cryostat approximately 3.5^o away from the neutron beam. Due to this large off-set it was decided to make the rocking curves by tilting the cryostat and figure 56 shows the observed flux line lattice. Again the two diffraction spots on the vertical axis were strong with well defined rocking curves even though the reciprocal lattice was rocked around the horizontal axis.
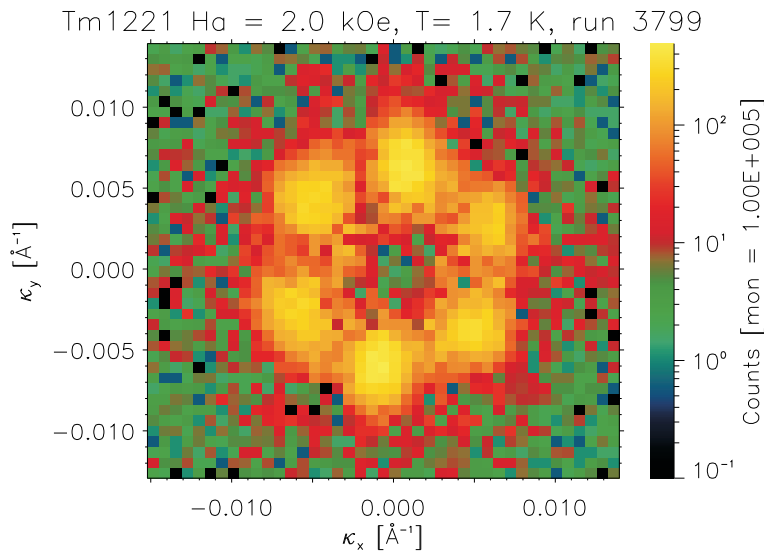
Figure 56. Hexagonal flux line lattice found in composite $TmNi_2B_2C$ *sample induced by an applied field along the crystalline (110) direction* $H\|(110) = 2.0\,kOe$ *and at* $T = 1.7\,K$

A hexagonal flux line lattice was observed in all of the examined phase space and figure 57 shows a plot of the logarithm of the squared form factor of the diffraction spots on the vertical axis determined by integrating the tilt rocking curves. Note that the scale is arbitrary. At low temperatures close to the magnetic phase transition at $T_N = 1.5\,K$ the curves show a trend similar to what was observed when $H\|c$. At low fields the curves are almost constant and then the intensity is decreasing fast for applied fields larger than $H \approx 1\,T$. For temperatures above $T = 3\,K$ the curves become somewhat more linear as expected from a normal flux line lattice.
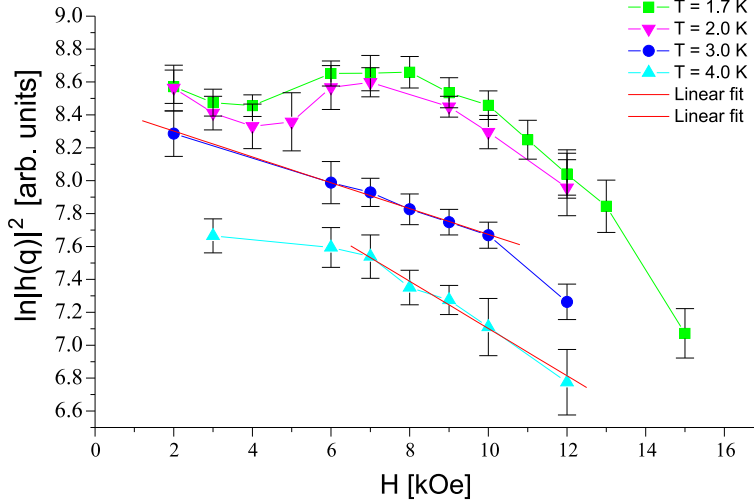
Figure 57. Logarithm of the flux line lattice reflectivity of the vertical strong diffraction spots induced by an applied field along the crystalline (110) direction of TmNi$_2$B$_2$C. *The bump in the reflectivity at low temperature is quite similar to what was observed when the field was applied along the crystalline c-axis and it is probably also connected to a modulation of the Tm ions by the flux line lattice.*

It is interesting to note that the intensity of the diffraction spots on the vertical axis are stronger than the rest of the diffraction spots at $H = 8.0\,kOe$ and $T = 1.5\,K$ as shown on figure 58, which corresponds to the peak in figure 57.

Discussion

From the experimental estimate of the coherence length shown on figure 49 one can calculate the expected transition from intermediate to high flux line density with the applied field in the ab-plane

$$H_{IH} = \frac{\Phi_0}{(c_{IH}\xi)^2} = \frac{2.07 \cdot 10^{-15}\,Tm^2}{(3.9 \cdot 110 \cdot 10^{-10}\,m)^2} = 1.1T \qquad (251)$$

which is in some agrement with the fast decay of the form factor shown on figure 57.

The origin of the bump in the logarithm of the squared form factor is probably also coming from the Tm ions which are modulated by the flux line lattice as described for $H\|c$ in the previous sections. However there will be a difference between a paramagnetic modulated structure, which should cause diffraction spots of equal intensity and a modulated spin density wave with the moment directed along the crystalline c-axis, which would cause the scattering to vanish when the lattice vector is along the moment direction due to the geometric factor $1 - k_z^2$.
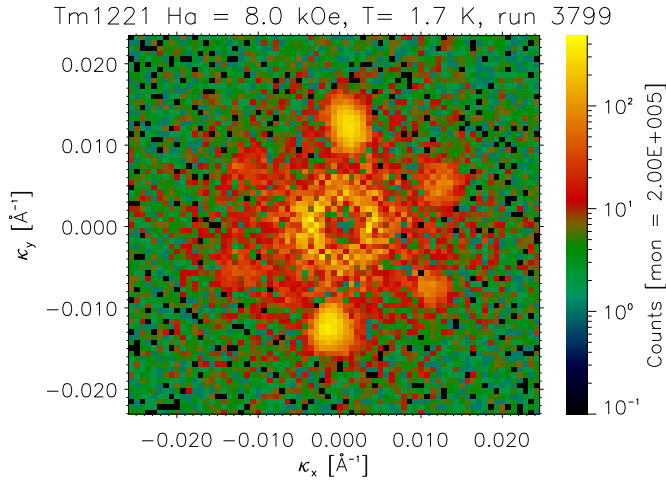
Figure 58. Diffraction pattern of $\mathrm{TmNi_2B_2C}$ *at* $H\|(110) = 8.0\,kOe$ *and* $T = 1.5K$ *showing strong peaks on the vertical axis, while the remaining peaks are weak even though the rocking curve is made by rotating around the horizontal axis.*

Figure 58 shows that the diffraction spots perpendicular to the moment direction and along the vertical axis does become stronger than the remaining spots. However the ratio between the intensity of the different diffraction spots caused by the geometric factor $1 - k_z^2$ should be field independent, which is not the case. Caution should also be take, because only the rocking curves of the vertical spots are well defined whereby a complete integration of the remaining spots is questionable.

It is recommended that this experiment is repeated with only one sample bar placed on a cadmium plate screening out the direct beam, whereby the intensity can be determined on an absolute scale. By doing the experiment in a dilution refrigerator it would also be possible to follow the intensity of the q_{mI} spin density wave.

9 Conclusion

The aspects of symmetry and intensity of the small angle neutron scattering diffraction patterns observed from the flux line lattice in $TmNi_2B_2C$ have been analyzed in detail, since both are deviating from the general picture found for the non-magnetic borocarbide superconductors.

A study of the symmetry changes of the flux line lattice in the paramagnetic phase with the applied field along the crystallographic c-axis resulted in an identification of three different phase : A low field hexagonal lattice, which smoothly changes into a square lattice around $H = 2.0\,kOe$ and this is changing back into a rhombic lattice as the applied field is further increased. The two transitions are suggested to be connected to two different length scales given by the non-locality radius of the non-local electrodynamics of the Kogan model and the crossover from intermediate to high flux line density, when the vortex cores start to overlap resulting in a reduction of the superconducting order parameter in between the flux lines. This leads to the conclusion that the flux line phases in the paramagnetic state are only indirectly connected to the magnetism, which only defines the temperature dependence of the coherence length $\xi(T)$. Following these arguments it

also seems plausibly that the crossover from intermediate to high flux line density is driving the magnetic phase transition between the two spin density waves q_{mI} and q_{mII} at low temperatures. The first order transition into the hexagonal flux line lattice phase at low temperature and high fields is however still unexplained.

The intensity of the diffraction spots from the flux line lattice in $TmNi_2B_2C$ with $H\|c$ are not in accordance with the expected behavior and it has been analyzed in several ways in this thesis. Previous analysis methods has been based on the change of the flux line form factor as the diffraction spot is moved in reciprocal space by changing the applied magnetic field. However this method is not applicable for $TmNi_2B_2C$, because the superconducting length scales are changing more dramatically with the applied field and temperature. A method where the ratio between the intensity of higher order diffraction spots are compared was introduced, but this did lead to conflicting conclusions. A second method where all diffraction spots were compared to a model for the flux line form factor on an absolute scale was introduced, but this also resulted in conclusions which indicated that the penetration depth was much smaller than expected from estimates based on magnetization and transport measurements. Finally a new interpretation of the diffraction pattern as being caused by scattering from the moments of the Tm-ions, which are modulated by the periodicity of the flux line lattice was introduced. The argument for this modulation is that the Tm moments are interacting indirectly by the RKKY coupling, which is changed by the presence of the superconducting gap, whereby the interaction is difference inside a vortex core and outside in the superconducting phase. A model calculation of the small angle neutron scattering cross section of this magnetic flux line lattice was performed and compared to the measured data. Finally an experiment with the field in the ab-plane have shown similar trends in the scattered intensity as in the case with $H\|c$ and the diffraction pattern might indicate that the diffraction spots coming from reciprocal lattice vectors which are perpendicular to the magnetic moment are stronger than the rest, but a disordering phenomena can not be rules out since the rocking curves are quite il defined. It is recommended to repeat the experiment with the field in the ab-plane in a dilution refrigerator on only one sample piece, where by the correlation to the spin density wave can be established. Also a low temperature study of the lower critical field and thereby a determination of the penetration depth would be valuable for a consistency check of the length scales obtained from the SANS measurements.

Acknowledgements

valuable theoretical insight from varies discussion during several APS meetings.

```
You could say I lost my faith in science and progress
You could say I lost my belief in the holy church
You could say I lost my sense of direction
You could say all of this and worse, but
If I ever lose my faith in you
There'd be nothing left for me to do
```

Appendix A: Resolution function

In the following an approximation for the resolution function of the SANS camera is obtained by assuming that the triangular wavelength and the trapeziodal beam divergence distributions can be described by gaussian distributions. Here the beam divergence will be assumed isotropic whereby the resolution function can be treated separately in the scattering plane and perpendicular to this. Furthermore the expression is only valid for scattering of neutrons without any energy transfer to the sample. The derivation is based on J.S. Pedersen et. al. [28], but extended to obtain the 3-dimensional resolution function.

Resolution function in the scattering plane

The momentum transfer $\boldsymbol{\kappa}$ of a neutron is given by the change of the wavevector $\mathbf{k}$ from the initial(i) to the final(f) state during a scattering process and it can be written in a complex form for the scattering plane shown on figure 59

$$
\begin{aligned}
\boldsymbol{\kappa} &= \mathbf{k_f} - \mathbf{k_i} \\
&= \frac{2\pi}{\lambda} \left(e^{i\theta_f} - e^{i\theta_i} \right) \tag{252}
\end{aligned}
$$

where λ is the neutron wavelength related to the wavevector by $|k| = \frac{2\pi}{\lambda}$ and the real and imaginary part of $\boldsymbol{\kappa}$ is along the z axis and in the detector plane respectively. The assumption of scattering without energy transfer to the sample result in the condition $|k_i| = |k_f|$.

In the following the resolution function is formulated as the number of available neutrons at different momentum transfer vectors, which can be scattered into the same detector pixel specified by the angle θ_f as illustrated on figure 59.

The incoming beam is approximated by a gaussian distribution of the form

$$
I(\lambda, \theta_i) \in N(\lambda_0, \theta_{i0}, \sigma_\lambda{}^2, \sigma_{\theta_i}{}^2) \tag{253}
$$

which is centered around the wavelength λ_0 of the velocity selector setting and the direction $\theta_i = 0$ of the z-axis of the camera. These values correspond to the nominal momentum transfer $< \boldsymbol{\kappa} >$ as marked by the black dots on figure 59.

Now we allow the incoming and scattered neutron direction to deviate from the nominal values $< \theta_i >= 0$ and $< \theta_f >= \theta_{f0}$ and want to find the corresponding momentum transfer vector $\boldsymbol{\kappa}$ and the number of neutrons at that $\boldsymbol{\kappa}$.

From the scattering angle $\theta = \frac{\theta_f - \theta_i}{2}$ the direction of the momentum transfer θ_κ is

$$
\begin{aligned}
\theta_\kappa &= \theta_i + \theta + \frac{\pi}{2} \\
&= \frac{\theta_f + \theta_i}{2} + \frac{\pi}{2} \tag{254}
\end{aligned}
$$

and the nominal direction is $< \theta_\kappa >= \frac{\theta_{f0}}{2} + \frac{\pi}{2}$. Thus a more convenient description of κ can be obtained by rotating the laboratory system into a coordinate system with the imaginary and real axis respectively along and perpendicular to the nominal $< \boldsymbol{\kappa} >$.

$$
\begin{aligned}
\boldsymbol{\kappa}_q &= \boldsymbol{\kappa} \cdot e^{-i\frac{\theta_{f0}}{2}} \\
&= \frac{2\pi}{\lambda} \left(e^{i(\theta_f - \frac{\theta_{f0}}{2})} - e^{i(\theta_i - \frac{\theta_{f0}}{2})} \right) \tag{255}
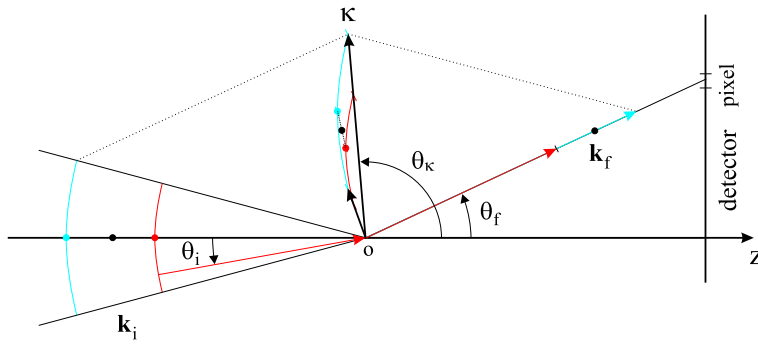\end{aligned}
$$

Figure 59. Neutrons with different incoming angles θ_i and wavevector size $|k| = \frac{2\pi}{\lambda}$ can be scattered into the same detector pixel at r_0 by different momentum transfer vectors $\boldsymbol{\kappa} = \boldsymbol{k}_f - \boldsymbol{k}_i$. Blue and red arcs indicate changes of the direction of the incoming neutron at a short and long wavelength and the dots show the momentum transfer when the beam divergence is absent $\theta_i = 0$. The scattering plane is spanned by the z axis and a radial detector direction given by ϕ in figure 20. θ_f and θ_κ are the angles of the scattered neutron and the momentum transfer vector $\boldsymbol{\kappa}$.

We now have a transformation from a given wavelength and incoming neutron direction to the corresponding $\boldsymbol{\kappa}_q$ vector which can cause scattering into the detector position determined by θ_f. The number of neutrons at $\boldsymbol{\kappa}_q = f(\lambda, \theta_i, \theta_f)$ is given by the two dimensional gaussian intensity distribution as function of the wavelength λ and the angles θ_i and θ_f. However we seek the neutron distribution as function of $\boldsymbol{\kappa}_q$ and an approximation for this can be obtained by making a Taylor expansion of (255).

Taylor expansion of momentum transfer

The momentum transfer vector $\boldsymbol{\kappa}_q$ can be written as a first order Tailor expansion around the nominal $< \boldsymbol{\kappa}_q >$ with respect to the neutron wavelength deviation and the angle deviation of the incoming and scattered neutron wavevector giving

$$
\kappa_q \approx \ <\kappa_q> + \left.\frac{\partial \kappa_q}{\partial \lambda}\right|_0 (\lambda - \lambda_0) + \left.\frac{\partial \kappa_q}{\partial \theta_i}\right|_0 (\theta_i - \theta_{i0}) + \left.\frac{\partial \kappa_q}{\partial \theta_f}\right|_0 (\theta_f - \theta_{f0}) \Rightarrow
$$

$$
\begin{aligned}
\kappa_q - <\kappa_q> \ \approx \ & -\frac{2\pi}{\lambda_0^2}\left(e^{i\frac{\theta_{f0}}{2}} - e^{-i\frac{\theta_{f0}}{2}}\right)(\lambda - \lambda_0) \\
& -i\frac{2\pi}{\lambda_0}e^{-i\frac{\theta_{f0}}{2}}(\theta_i - \theta_{i0}) \\
& +i\frac{2\pi}{\lambda_0}e^{i\frac{\theta_{f0}}{2}}(\theta_f - \theta_{f0}) \\
\approx \ & ik_0\left[-\frac{<\kappa_q>}{2\pi}(\lambda - \lambda_0) + \cos\left(\frac{\theta_{f0}}{2}\right)\{(\theta_f - \theta_{f0}) - (\theta_i - \theta_{i0})\}\right] \\
& -\frac{<\kappa_q>}{2}\{(\theta_f - \theta_{f0}) + (\theta_i - \theta_{i0})\}
\end{aligned} \tag{256}
$$

where $k_0 = \frac{2\pi}{\lambda_0}$. The advantage of the Tailor expansion is that the approximate momentum transfer vector is given by a sum of normal distributed variables, whereby the distribution of κ_q also will be normal distributed according to the convolution theorem : If a stochastic variable is given by $Z = \sum_i a_i X_i$ with $X_i \in N(\mu_i, \sigma_i^2)$ being independent and normal distributed having a mean μ_i and variance σ_i^2 then

$$Z \in N \left(\sum_i (a_i \mu_i), \sum_i (a_i \sigma_i)^2 \right) \tag{257}$$

Thus we can immediately write down the variance of the momentum transfer distribution from (256)

$$\sigma_{||}^2 \;\; = \;\; k_0^2 \left\{ \left(\frac{< \kappa_q >}{2\pi} \sigma_\lambda \right)^2 + \cos^2 \left(\frac{\theta_{f0}}{2} \right) \left(\sigma_{\theta_f}^2 + \sigma_{\theta_i}^2 \right) \right\}$$

$$\sigma_\perp^2 \;\; = \;\; \frac{< \kappa_q >^2}{4} \left(\sigma_{\theta_f}^2 + \sigma_{\theta_i}^2 \right) \tag{258}$$

and the distribution is given by

$$R(\kappa_q, < \kappa_q >) = \frac{1}{\sqrt{2\pi}\sigma_{||}\sigma_\perp} \exp \left\{ -\frac{1}{2} \left(\frac{(\kappa_{q||} - < \kappa_{q||} >)^2}{\sigma_{||}^2} + \frac{\kappa_{q\perp}^2}{\sigma_\perp^2} \right) \right\} \tag{259}$$

where the pre-factor ensured the area of the resolution function to be normalized.

What we learn from the distribution above is how the instrumental settings of the SANS camera will influence the number of available neutron at κ_q causing scattering into $< \kappa_q >$. The three contributions to the width $\sigma_{||}^2$ along the momentum transfer is determined by the wavelength spread σ_λ of the velocity selector, the beam divergence σ_{θ_i} controlled by the collimation section, and the detector resolution σ_{θ_f} related to the pixel size of the detector. For the width perpendicular to the momentum transfer $\sigma_\perp^2$ the beam divergence term and detector resolution are found again, but the dependence on the wavelength spread does not appear. This is because a change in λ will only cause a change in the length of κ_q, but no rotation since all derivatives with respect to λ have no real part, $Re \left(\frac{\partial^n \kappa_q}{\partial \lambda^n} \right) = 0$. Thus the effect of the wavelength spread only enters in the cross terms of the Tailor expansion

$$\left. \frac{\partial^2 \kappa_q}{\partial \lambda \partial \theta_i} \right|_0 (\lambda - \lambda_0)(\theta_i - \theta_{i0}) \;\; = \;\; i k_0 \cos \left(\frac{\theta_{f0}}{2} \right)(\theta_i - \theta_{i0}) \frac{(\lambda - \lambda_0)}{\lambda_0} \tag{260}$$

$$+ \frac{< \kappa >}{2}(\theta_i - \theta_{i0}) \frac{(\lambda - \lambda_0)}{\lambda_0} \tag{261}$$

These cross terms are not easy to include in the widths, since the convolution theorem is only valid for independent variables. An estimate of the effect of these terms can be made if the wavelength spread $\frac{(\lambda - \lambda_0)}{\lambda_0}$ is assumed to be a constant, whereby it is seen that an extra term similar to the beam divergence must be added to $\sigma_\perp^2$

$$\sigma_\perp^2 = < \kappa >^2 \left(\frac{\sigma_i}{2} \right)^2 \left(1 + \frac{(\lambda - \lambda_0)}{\lambda_0} \right)^2 \tag{262}$$

However the $\sigma_\perp^2$ will be dominated by the beam divergence since $\frac{(\lambda - \lambda_0)}{\lambda_0} = 0.1 - 0.2$ in most cases.

Detector resolution

The detector consists of pixels of a finite size Δr and neutrons scattered in a small angular range around θ_f will be detected in the same pixel at r_0 as shown on figure

59. By representing the pixel as a gaussian distribution centered at r_0 and with a width

$$\sigma_r = \frac{1}{2\sqrt{2ln2}}\Delta r \tag{263}$$

the corresponding width of the angle θ_f is found by Taylor expanding $\theta_f = \arctan\left(\frac{r}{z}\right)$. In the small angle limit $r << z$ one gets

$$\sigma_{\theta_f} = \frac{\sigma_r}{z} \tag{264}$$

The relation between standard deviation σ and Full Width Half Maximum Δ_{FWHM} of a gaussian has been used above

$$\Delta_{FWHM} = 2\sqrt{2ln2}\sigma \tag{265}$$

Resolution function perpendicular to the scattering plane

In order to include the resolution perpendicular to the scattering plane we need a 3 dimensional transformation from wavelength, in- and out of plane beam divergence into the momentum transfer. Figure (60) show the projection of the incoming and scattered neutron onto the scattering plane spanned by the z axis and the radial direction $\mathbf{e}_R$ of the detector plane. When the nominal values of the angles are inserted the nominal momentum transfer plane is obtained.

$$\begin{aligned}
&< \theta_i >= 0 \qquad < \phi_i >= 0 \\
&< \theta_f >= \theta_{f0} \quad < \phi_f >= 0
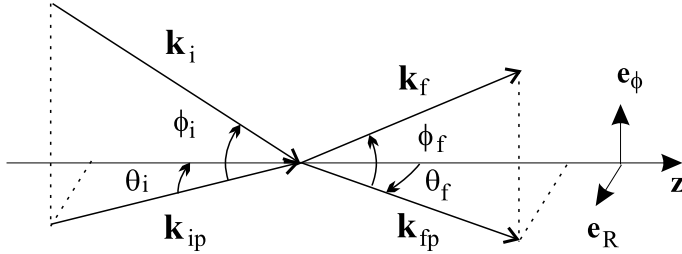\end{aligned} \tag{266}$$

Figure 60. The momentum transfer can be decomposed into components in the scattering plane described by $(\mathbf{k}_{ip}, \mathbf{k}_{fp})$ and an out-of-plane component depending on the angles (ϕ_i, ϕ_f) that the incoming and scattered neutron are tilted with respect to the scattering plane.

The 3-dimensional momentum transfer is decomposed into the scattering plane and a direction $\mathbf{e}_\phi$ perpendicular to the scattering plane

$$\begin{aligned}
\kappa \;=\;& \kappa_{\mathbf{p}} + \kappa_\phi \mathbf{e}_\phi \\
=\;& \mathbf{k}_{fp} - \mathbf{k}_{ip} + (k_{f\phi} - k_{i\phi})\mathbf{e}_\phi \\
=\;& |k_f| \cos(\phi_f) e^{i\theta_f} - |k_i| \cos(\phi_i) e^{i\theta_i} \\
&+ \;\{|k_f| \sin(\phi_f) - |k_i| \sin(\phi_i)\} \, \mathbf{e}_\phi \\
=\;& \frac{2\pi}{\lambda} \left\{\cos(\phi_f) e^{i\theta_f} - \cos(\phi_i) e^{i\theta_i}\right\} \\
&+ \;\frac{2\pi}{\lambda} \left\{\sin(\phi_f) - \sin(\phi_i)\right\} \mathbf{e}_\phi
\end{aligned} \tag{267}$$

The in-plane component has been written in the complex notation used in the previous section and the rotation from the laboratory coordinate system into a system following the nominal momentum transfer can be done again.

$$
\begin{aligned}
\kappa_q &= \kappa e^{-i\frac{\theta_{f0}}{2}} \\
&= \frac{2\pi}{\lambda}\left\{\cos(\phi_f)e^{i(\theta_f - \frac{\theta_{f0}}{2})} - \cos(\phi_i)e^{i(\theta_i - \frac{\theta_{f0}}{2})}\right\} \\
&+ \frac{2\pi}{\lambda}\left\{\sin(\phi_f) - \sin(\phi_i)\right\}\mathbf{e}_\phi
\end{aligned}
\tag{268}
$$

Once again the Tailor expansion can be made to obtain an approximation for the κ_q distribution, but it is easily seen that the out-of-plane angles are decoupled from the in-plane momentum transfer whereby the in-plane distribution of the previous section is found again. The out-of-plane component however gives

$$
\begin{aligned}
\kappa_\phi &\approx \; <\kappa_\phi> + \left.\frac{\partial\kappa_\phi}{\partial\lambda}\right|_0 (\lambda - \lambda_0) + \left.\frac{\partial\kappa_\phi}{\partial\phi_i}\right|_0 (\phi_i - \phi_{i0}) + \left.\frac{\partial\kappa_\phi}{\partial\phi_f}\right|_0 (\phi_f - \phi_{f0}) \\
&\approx \; \frac{2\pi}{\lambda_0}((\phi_f - \phi_{f0}) - (\phi_i - \phi_{i0}))
\end{aligned}
\tag{269}
$$

and the out-of-plane width σ_ϕ^2 is

$$
\sigma_\phi^2 = k_0{}^2(\sigma_{\phi_f}^2 + \sigma_{\phi_i}^2)
\tag{270}
$$

where the two terms show the influence of the out-of-plane beam divergence and the out-of-plane detector resolution respectively.

Combined resolution function

The combined resolution function is then given by

$$
R(\kappa_q, <\kappa_q>) = \frac{1}{\sqrt{2\pi}\sigma_{||}\sigma_\perp\sigma_\phi}\exp\left\{-\frac{1}{2}\left(\frac{(\kappa_{q||} - <\kappa_q>)^2}{\sigma_{||}^2} + \frac{(\kappa_{q\perp})^2}{\sigma_\perp^2} + \frac{(\kappa_{q\phi})^2}{\sigma_\phi^2}\right)\right\}
\tag{271}
$$

where the width $\sigma_{||}$ along the momentum transfer vector is denoted the longitudinal resolution, $\sigma_\perp$ in the plane is called the transverse resolution and the out-of plane width σ_ϕ is denoted the azimuthal resolution related to the azimuthal angle ϕ.

$$
\begin{aligned}
\sigma_{||}^2 &= k_0^2\left\{\left(\frac{<\kappa_q>}{2\pi}\sigma_\lambda\right)^2 + \cos^2\left(\frac{\theta_{f0}}{2}\right)\left(\sigma_{\theta_f}^2 + \sigma_{\theta_i}^2\right)\right\} \tag{272} \\
\sigma_\perp^2 &= \frac{<\kappa_q>^2}{4}\left(\sigma_{\theta_f}^2 + \sigma_{\theta_i}^2\right) \tag{273} \\
\sigma_\phi^2 &= k_0{}^2(\sigma_{\phi_f}^2 + \sigma_{\phi_i}^2) \tag{274}
\end{aligned}
$$

The widths may now be expressed from the instrument settings derived in section 4 and 264

$$\sigma_\lambda \quad = \quad \frac{\lambda_0}{2\sqrt{2ln2}} \frac{\Delta\lambda}{\lambda_0} \tag{275}$$

$$\sigma_{\theta_i} \quad = \quad \frac{1}{2\sqrt{2ln2}} \Delta\theta_i \tag{276}$$

$$\sigma_{\theta_f} \quad = \quad \frac{1}{2\sqrt{2ln2}} \frac{\Delta r}{z} \tag{277}$$

Figure (61) show the combined resolution function for scattering into a detector pixel corresponding to the nominel $< \kappa >$ at the center of the cigar shaped gaussian distribution. Thus the resolution function gives the intensity scattered into the pixel as a reciprocal lattice vector τ is moved around in space by changing the angle ω.
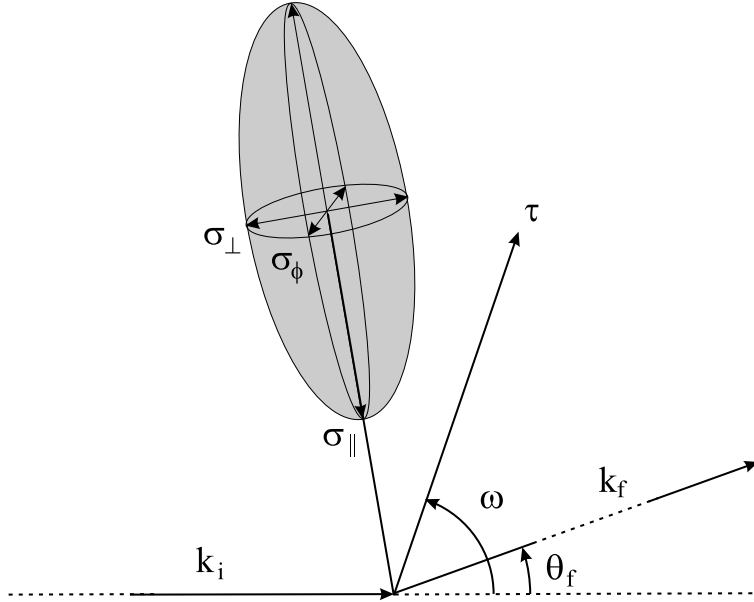

Figure 61. Gaussian resolution function for scattering into the detector pixel corresponding to the nominal momentum transfer $< \kappa >$ at the center of the distribution. The shape of the distribution is given by the longitudinal width $\sigma_{||}$, the transverse width $\sigma_\perp$ and the azimuthal width σ_ϕ.

Appendix B: Definition of mathematical functions

Fourier Transform

The definition of the Fourier transform used is

$$\mathcal{F}\{f(\boldsymbol{r})\} = F(\boldsymbol{k}) = \int f(\boldsymbol{r})\exp\left(-i\boldsymbol{k}\cdot\boldsymbol{r}\right)d\boldsymbol{r} \tag{278}$$

and the inverse transformation is

$$f(\boldsymbol{r}) = \frac{1}{(2\pi)^3}\int F(\boldsymbol{k})\exp\left(i\boldsymbol{k}\cdot\boldsymbol{r}\right)d\boldsymbol{k} \tag{279}$$

Fourier convolution theorem

The Fourier convolution theorem states that the Fourier transform of the convolution of two functions f and g is identical to the product of the Fourier transform of each of the two function

$$\mathcal{F}\{f * g\} = \mathcal{F}\{f\}\mathcal{F}\{g\} \tag{280}$$

Proof

First the convolution f*g is rewritten by expressing the two functions from their transforms F and G

$$
\begin{aligned}
f * g(\boldsymbol{r}) &= \int_{\boldsymbol{u}} f(\boldsymbol{u})g(\boldsymbol{r}-\boldsymbol{u})d\boldsymbol{u} \\
&= \frac{1}{(2\pi)^6}\int_{\boldsymbol{u}}\int F(\boldsymbol{k})\exp\left(i\boldsymbol{k}\cdot\boldsymbol{u}\right)d\boldsymbol{k}\int G(\boldsymbol{k}')\exp\left(i\boldsymbol{k}'\cdot(\boldsymbol{r}-\boldsymbol{u})\right)d\boldsymbol{k}'d\boldsymbol{u} \\
&= \frac{1}{(2\pi)^6}\int\int F(\boldsymbol{k})G(\boldsymbol{k}')\exp\left(i\boldsymbol{k}'\cdot\boldsymbol{r}\right)\int_{\boldsymbol{u}}\exp\left(i(\boldsymbol{k}-\boldsymbol{k}')\cdot\boldsymbol{u}\right)d\boldsymbol{u}d\boldsymbol{k}'d\boldsymbol{k} \\
&= \frac{1}{(2\pi)^6}\int\int F(\boldsymbol{k})G(\boldsymbol{k}')\exp\left(i\boldsymbol{k}'\cdot\boldsymbol{r}\right)(2\pi)^3\delta(\boldsymbol{k}-\boldsymbol{k}')d\boldsymbol{k}'d\boldsymbol{k} \\
&= \frac{1}{(2\pi)^3}\int F(\boldsymbol{k})G(\boldsymbol{k})\exp\left(i\boldsymbol{k}\cdot\boldsymbol{r}\right)d\boldsymbol{k} \tag{281}
\end{aligned}
$$

and the Fourier transform of this is

$$
\begin{aligned}
\mathcal{F}\{f * g\} &= \int f * g\exp\left(-i\boldsymbol{k}'\cdot\boldsymbol{r}\right)d\boldsymbol{r} \\
&= \int\frac{1}{(2\pi)^3}\int F(\boldsymbol{k})G(\boldsymbol{k})\exp\left(i\boldsymbol{k}\cdot\boldsymbol{r}\right)d\boldsymbol{k}\exp\left(-i\boldsymbol{k}'\cdot\boldsymbol{r}\right)d\boldsymbol{r} \\
&= \frac{1}{(2\pi)^3}\int F(\boldsymbol{k})G(\boldsymbol{k})\int\exp\left(i(\boldsymbol{k}-\boldsymbol{k}')\cdot\boldsymbol{r}\right)d\boldsymbol{r}d\boldsymbol{k} \\
&= \frac{1}{(2\pi)^3}\int F(\boldsymbol{k})G(\boldsymbol{k})(2\pi)^3\delta(\boldsymbol{k}-\boldsymbol{k}')d\boldsymbol{k} \\
&= F(\boldsymbol{k})G(\boldsymbol{k}) \\
&= \mathcal{F}\{f\}\mathcal{F}\{g\} \tag{282}
\end{aligned}
$$

It should be noted that if the convolution is defined by

$$f \tilde{*} g(\boldsymbol{r}) \;\; = \;\; \int_{\boldsymbol{u}} f(\boldsymbol{u}) g(\boldsymbol{u} - \boldsymbol{r}) d\boldsymbol{u} \tag{283}$$

then the convolution theorem is slightly change

$$\begin{aligned}
\mathcal{F}\{f \tilde{*} g\} &= \int f * g \exp\left(-i\boldsymbol{k}' \cdot \boldsymbol{r}\right) d\boldsymbol{r} \\
&= F(\boldsymbol{k}) G(-\boldsymbol{k}) \\
&= F(\boldsymbol{k}) G(\boldsymbol{k})^{\dagger} \tag{284}
\end{aligned}$$

The last step is valid when the function G is real, $G = G^{\dagger}$.

Representation of a periodic function

A periodic function can be represented as a Fourier series

$$f(\boldsymbol{r}) = \sum_{\boldsymbol{\tau}} F(\boldsymbol{\tau}) \exp\left(i\boldsymbol{\tau} \cdot \boldsymbol{r}\right) \tag{285}$$

where the vectors $\boldsymbol{\tau}$ are the lattice points in reciprocal space defined from the real space unit cell of the periodic function. The coefficients in the series are found by multiplying $f(\boldsymbol{r})$ with $\exp\left(-i\boldsymbol{k} \cdot \boldsymbol{r}\right)$ and integrating over the real space unit cell of volume v_0

$$\begin{aligned}
\int_{cell} f(\boldsymbol{r}) \exp\left(-i\boldsymbol{k} \cdot \boldsymbol{r}\right) d\boldsymbol{r} &= \int_{cell} \sum_{\boldsymbol{\tau}} F(\boldsymbol{\tau}) \exp\left(i(\boldsymbol{\tau} - \boldsymbol{k}) \cdot \boldsymbol{r}\right) d\boldsymbol{r} \\
&= \sum_{\boldsymbol{\tau}} F(\boldsymbol{\tau}) v_0 \delta(\boldsymbol{\tau} - \boldsymbol{k}) \\
&= v_0 F(\boldsymbol{\tau}) \tag{286}
\end{aligned}$$

Thus

$$F(\boldsymbol{\tau}) = \frac{1}{v_0} \int_{cell} f(\boldsymbol{r}) \exp\left(-i\boldsymbol{k} \cdot \boldsymbol{r}\right) d\boldsymbol{r} \tag{287}$$

δ function representation

The $Sinc^2$ function

$$\frac{\sin^2\left(\frac{\kappa}{2}L\right)}{\left(\frac{\kappa}{2}\right)^2} = c\delta(\kappa) \tag{288}$$

can be represented as a δ-function since it is highly peaked at $\kappa = 0$ and the normalization constant c is found by integrating the above equation over all κ.

$$\int_{\kappa=-\infty}^{\infty} \frac{\sin^2\left(\frac{\kappa}{2}L\right)}{\left(\frac{\kappa}{2}\right)^2} d\kappa = 8 \int_{\kappa=0}^{\infty} \frac{\sin^2\left(\frac{\kappa}{2}L\right)}{\kappa^2} d\kappa = 8\frac{\pi}{2}\frac{L}{2} = c \quad \Rightarrow$$

$$c = 2\pi L \tag{289}$$

Appendix C: Vortex core size of the Ginzburg-Landau model

In this appendix the description of the core of a flux line in the Ginzburg-Landau(GL) model is examined in more detail in order to determine the Half Width Half Maximum(HWHM) core size which can be compared to other models such as the gaussian description of the moment distribution of the magnetic flux line lattice.

The best description of an isolated flux line in the high-κ limit has been obtained by Clem *et. al.* from a variation minimization of the free energy of the GL equations [19]. In this model the order parameter of the core is described by

$$f(r) = \frac{r}{\sqrt{r^2 + 2\xi^2}} \tag{290}$$

where r is the radial distance from the flux line center and ξ is the GL coherence length connected to the upper critical field $H_{c2} = \frac{\Phi_0}{2\pi\xi^2}$. The HWHM width of the core is found by solving

$$f(r_{\frac{1}{2}}) = \frac{1}{2} \Rightarrow$$

$$r_{\frac{1}{2}} = \sqrt{\frac{2}{3}}\xi = 0.82\,\xi \tag{291}$$

The corresponding gaussian description of the core is given by

$$g(r) = 1 - \exp\left(-\frac{r^2}{2\sigma^2}\right) \tag{292}$$

and the HWHM is found by solving

$$g(r_{\frac{1}{2}}) = \frac{1}{2} \Rightarrow$$

$$r_{\frac{1}{2}} = \sqrt{2\ln 2}\,\sigma \tag{293}$$

By equating the HWHM of the two models a relation between the gaussian width and the GL coherence length is established

$$\sqrt{\frac{2}{3}}\xi = \sqrt{2\ln 2}\,\sigma \Rightarrow$$

$$\xi = \sqrt{3\ln 2}\,\sigma \tag{294}$$

Figure 62 show the shape of the superconducting order parameter at the vortex cores as described by the Clem solution, which is identical to the Tinkham solution given by equation (51) with $\nu = \frac{1}{\sqrt{2}}$ close to the core. The gaussian approximation with a HWHM identical to the Clem solution is also shown in the figure.

References

[1] P.C. Canfield *et. al.* New magnetic superconductors : A toy box for solid-state physicist. *Physics Today*, October:40–46, 1998.
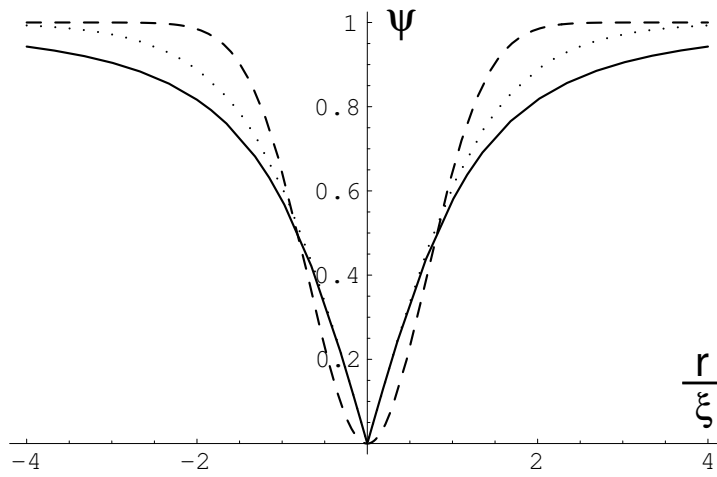
Figure 62. Plot of the normalized superconducting order parameter $\Psi(r)$ near the vortex core described by the Clem model(solid) $\Psi(r) = \frac{r}{\sqrt{r^2+2\xi^2}}$, the Tinkham model(dotted) $\Psi(r) = \tanh\left(\frac{r}{\sqrt{2}\xi}\right)$ and a gaussian approximation(dashed) $\Psi(r) = 1 - \exp\left(-\frac{r^2}{2\sigma^2}\right)$. The Half Width Half Maximum(HWHM) of the gaussian model has been matched to the HWHM of the Clem model by the relation $\xi = \sqrt{3\ln 2}\sigma$.

[2] R.J. Cava *et. al.* Superconductivity in the quaternary intermetallic compounds LnNi$_2$B$_2$C. *Nature*, 367:252–253, 1994.

[3] T. Siegrist *et. al.* The crystal structure of superconducting LuNi$_2$B$_2$C and the related phase LuNiBC. *Nature*, 367:254–256, 1994.

[4] Ø . Fischer and M.B. Mable. *Superconductivity in ternary compounds I + II.* Springer, 1982. ISBN 3-540-11814-4.

[5] J.W. Lynn *et. al.* Magnetic order and crystal structure in the superconducting RNi$_2$B$_2$C materials. *Phys. Rev. B*, 55:6584–6598, 1997.

[6] U. Yaron *et. al.* Microscopic coexistence of magnetism and superconductivity in ErNi$_2$B$_2$C. *Nature*, 382:236–238, 1996.

[7] M.R. Eskildsen, K. Harada, P.L. Gammel, A.B. Abrahamsen, N.H. Andersen, G. Ernst, A.P. Ramirez, D.J. Bishop, K. Mortensen, D.G. Naugle, K.D.D. Rathnayaka, and P.C. Canfield. Intertwined symmetry of the magnetic modulation and the flux-line lattice in the superconducting state of TmNi$_2$B$_2$C. *Nature*, 393:242–245, 1998.

[8] M.R. Eskildsen. *Small angle neutron scattering studies of the flux line lattices in the borocarbide superconductors.* PhD thesis, Risø National Laboratory, Denmark, 1998. ISBN 87-550-2472-6.

[9] V.L. Ginzburg and L.D. Landau. *Zh. Eksperim. i. Teor. Fiz.*, 20:1064, 1950.

[10] J. Bardeen, L.N. Cooper, and J.R. Schrieffer. Microscopic theory of superconductivity. *Phys. Rev.*, 106(1):162–164, 1957.

[11] J. Bardeen, L.N. Cooper, and J.R. Schrieffer. Theory of superconductivity. *Phys. Rev.*, 108(5):1175–1204, 1957.

[12] J.A. Bednorz and K.A. Müller. Possible high-tc superconductivity in the $Ba - La - Cu - O$ system. *Zeit. phys. B cond. Mat.*, 64(2):189–193, 1986.

[13] H. Frölich. Theory of superconducting state. i. the ground state at the absolute zero of temperature. *Phys. Rev.*, 79:845, 1950.

[14] J.R. Schrieffer. *Theory of superconductivity*. Perseus Books, 1964(1999). ISBN 0-7382-0120-0.

[15] P.G. de Gennes. *Superconductivity of metals and alloys*. Perseus Books Publishing, 1966(1999). ISBN 0-7382-0101-4.

[16] Michael Tinkham. *Introduction to superconductivity*. McGraw-Hill, 1996. ISBN 0-07-064878-6.

[17] E.M. Lifshitz and L.P. Pitaevskii. *Statistical physics, Landau and Lifshitz course of theoretical physics*, volume 9. Butterworth-Heinemann, 1980. ISBN 0-7506-2636-4.

[18] M.R. Spiegel. *Mathematical handbook of formulas and tables*. Shaum's outline series. McGraw-Hill, 1992. ISBN : 0-07-060224-7.

[19] J.R. Clem *et. al.* Simple model for the vortex core in a type ii superconductor. *J. Low Temp. Phys.*, 18:427, 1975.

[20] A. Yaouanc *et. al.* Effect of the vortex core on the magnetic field in hard superconductors. *Phys. Rev. B*, 55:11107, 1997.

[21] E.H. Brandt. The flux line lattice in superconductors. *Rep. Prog. Phys.*, 58:1465–1594, 1995.

[22] V.G. Kogan *et. al.* Vortex lattice transitions in borocarbides. *Phys. Rev. B.*, 55:R8693, 1997.

[23] A. I. Larkin and Y. V. Ovchinnikov. Pinning in type-ii superconductors. *J. Low. Temp. Phys.*, 34(3-4):409–428, 1979.

[24] J. Kierfeld *et. al.* Dislocations and the critical endpoint of the melting line of vortex line lattices. *Phys. Rev. B*, 61:R14928, 2000.

[25] G.L. Squires. *Introduction to the theory of thermal neutron scattering*. Cambridge University press, 1978. ISBN 0-486-69447-x.

[26] H. Suhl. Inertial mass of moving fluxiod. *Phys. Rev. Lett.*, 14(7):226–229, 1965.

[27] M.P. Maley L.N. Bulaevskii and I.F. Schegolev. Vortex fluctuations in josephson-coupled superconductors. *Physica B*, 197:506–513, 1997.

[28] J.S. Pedersen, D. Posselt, and K. Mortensen. Analytical treatment of the resolution function for small-angle scattering. *J. Appl. Cryst.*, 23:321–333, 1990.

[29] P. Harris. *Neutron and X-ray diffraction from modulated structure*. PhD thesis, Ris øNational Laboratory, Denmark, 1994. ISBN 87-550-1975-7.

[30] G. Shirane, S.M. Shapiro, and J.M. Tranquada. *Neutron scattering with a triple-axis spectrometer - Basic techniques*. Cambridge University press, 2002. ISBN 0-521-41126-2.

[31] L.F. Mattheiss. Electronic properties of superconducting $LuNi_2B_2C$ and related boride carbide phases. *Phys. Rev. B*, 49:13279, 1994.

[32] W.E. Pickett *et. al.* $LuNi_2B_2C$: A novel ni-based strong coupling superconductor. *Phys. Rev. lett.*, 72:3702, 1994.

[33] S.B. Dugdale *et. al.* Nesting properties and anisotropy of the fermi surface of $LuNi_2B_2C$. *Phys. Rev. lett.*, 83:4824, 1999.

[34] I.R. Fisher *et. al.* Anisotropic resistivity and normal-state magnetoresistance of RNi_2B_2C $(R = Y, Lu, Er, Ho)$. *Phys. Rev. B*, 56:10820, 1997.

[35] K.D.D. Rathnayaka *et. al.* Transport and superconducting properties of RNi_2B_2C $(R = Y, Lu)$ single crystals. *Phys. Rev. B*, 55:8506, 1997.

[36] G.M. Schmiedeshoff *et. al.* Critical fields and specific heat of $LuNi_2B_2C$. *Phys. Rev. B*, 63:134519, 2001.

[37] D.G. Naugle *et. al.* Critical field and magnetoresistance of single crystal $TmNi_2B_2C$. *Int. J. Mod. Phys. B*, 13(29-31):3715, 1999.

[38] B.K. Cho *et. al.* Magnetism and superconductivity in single-crystal $ErNi_2B_2C$. *Phys. Rev. B*, 52:3684, 1995.

[39] K.D.D. Rathnayaka *et. al.* Anisotropic magnetoresistance of single-crystal $HoNi_2B_2C$ and the interplay of magnetic and superconducting order. *Phys. Rev. B*, 53:5688, 1996.

[40] C.V. Tomy *et. al.* Superconductivity and magnetism in $DyNi_2B_2C$ single-crystals. *Phys. Rev. B*, 52:9186, 1995.

[41] H. Michor *et. al.* Specific-heat analysis of rare-earth transition-metal boro-carbides: An estimation of the electron-phonon coupling strength. *Phys. Rev. B*, 52:16165, 1995.

[42] A. Andreone *et. al.* Transport and tunneling measurements in superconducting YNi_2B_2C. *Physica C*, 251:379, 1995.

[43] H. Sakata *et. al.* Imaging of a vortex lattice transition in YNi_2B_2C by scanning tunneling spectroscopy. *Phys. Rev. Lett.*, 84:1583, 2000.

[44] B.K. Cho *et. al.* Magnetism and superconducting properties of single-crystal $TmNi_2B_2C$. *Phys. Rev. B*, 52:3676, 1995.

[45] A.I. Goldman *et. al.* Magnetic pair breaking in $HoNi_2B_2C$. *Phys. Rev. B*, 50:9668, 1994.

[46] C. Detlefs *et. al.* Ordering wave vectors of metamagnetic states in $HoNi_2B_2C$: One dimension is not enough. *Phys. Rev. B*, 61:1, 2000.

[47] B.K. Cho *et. al.* Onset of superconductivity in the antiferromagnetically ordered state of single-crystal $DyNi_2B_2C$. *Phys. Rev. B*, 52:R3844, 1995.

[48] H. Michor *et. al.* The interplay of the superconducting and antiferromagnetic state in $DyNi_2B_2C$. *Physica B*, 259-261:604, 1999.

[49] N.W. Ashcroft and N.D. Mermin. *Solid State Physics*. Harcourt Brace College Publishers, 1976. ISBN 0-03-049346-3.

[50] J. Jensen and A.R. Mackintosh. *Rare earth magnetism*. Clarendon Press, 1991. ISBN 0-19-852027-1.

[51] J.Y. Rhee *et. al.* Generalized susceptibility and magnetic ordering in the rare-earth nickel boride carbides. *Phys. Rev. B.*, 51:15585, 1995.

[52] A.M. Clogston. Upper limit for the critical field in hard superconductors. *Phys. Rev. Lett.*, 9(6):266, 1962.

[53] P.C. Canfield *et. al.* Breakdown of de gennes scaling in $(R_{1-x}R'_x)Ni_2B_2C$ compounds. *Phys. Rev. Lett.*, 77:163–166, 1996.

[54] M.R. Eskildsen *et. al.* Observation of a field-driven structural phase transition in the flux line lattice in $ErNi_2B_2C$. *Phys. Rev. Lett.*, 78(10):1968–1971, 1997.

[55] M.R. Eskildsen *et. al.* Square to hexagonal symmetry transition of the flux line lattice in YNi_2B_2C for different field orientations. *Physica B*, 241:811–813, 1997.

[56] P.L. Gammel *et. al.* Systematic studies of the square-hexagonal flux line lattice transition in $Lu(Ni_{1-x}Co_x)_2B_2C$: The role of nonlocality. *Phys. Rev. Lett.*, 82:4082–4085, 1999.

[57] Y. DeWilde *et. al.* Scanning tunneling microscopy observation of a square abrikosov lattice in $LuNi_2B_2C$. *Phys. Rev. Lett.*, 78:4273, 1997.

[58] V.G. Kogan *et. al.* Nonlocal electrodynamics and low-temperature magnetization of clean high-κ superonductors. *Phys. Rev. B.*, 54:12386, 1996.

[59] Paul D. McK. *et. al.* Nonlocal effect and vortex lattice transition in YNi_2B_2C. *Phys. Rev. Lett.*, 80:1517–1519, 1998.

[60] L.Y. Vinnikov *et. al.* Low field reorientation transition and asisotropic orientational order of the vortex lattices in $LuNi_2B_2C$. *Phys. Rev. B*, 64:220508, 2001.

[61] M.R. Eskildsen, A.B. Abrahamsen, D. Lopez, P.L. Gammel, D.J. Bishop, N.H. Andersen, K. Mortensen, and P.C. Canfield. Flux line lattice reorientation in the borocarbide superconductors with h parallel to a. *Phys. Rev. Lett.*, 86:320–323, 2001.

[62] A. Knigavko and B. Rosenstein. 90° reorientation in the vortex lattice of borocarbide superconductors. *Phys. Rev. B*, 62:15151, 2000.

[63] M.R. Eskildsen, A.B. Abrahamsen, V.G. Kogan, P.L. Gammel, K. Mortensen, N.H. Andersen, and P.C. Canfield. Temperature dependence of the flux line lattice transition into square symmetry in superconducting $LuNi_2B_2C$. *Phys. Rev. Lett.*, 86:5148–5151, 2001.

[64] A. Gurevich and V.G. Kogan. Effect of fluctuations on vortex lattice structural transitions in superconductors. *Phys. Rev. Lett.*, 87:177009, 2001.

[65] U. Gasser *et. al.* Neutron crytal-field spectroscopy of $RNi_2^{11}B_2C$ (R = Ho, Er, Tm). *Z. Phys. B*, 101:345–352, 1996.

[66] M.R. Eskildsen *et. al.* Hysteresis in the field-induced magnetic structure in $TmNi_2B_2C$. *Physica B*, 261:582–583, 1999.

[67] K. H. Müller and V. Narozhnyi. *Rare earth transition metal borocarbides (nitrides): Superconducting, magnetic and normal state properties.* Nato science series. Kluwer Academic Publishers, 2001. ISBN 0-7923-6878-9.

[68] H. Ullmaier J. Schelten and W. Schmatz. Neutron diffraction by vortex latticies in in superconducting nb and $Nb_{0.73}Ta_{0.27}$. *Phys. Stat. Sol. (b)*, 48:619–628, 1971.

[69] H. Ullmaier J. Schelten and G. Lippmann. Local magnetic field distributions in superconducting niobium at 4.2 k by neutron diffraction. *Z. Physik*, 253:219–231, 1972.

[70] J. R. Clem. *Phenomenological theory of the local magnetic field in Type-II superconductors*, volume 2 of *Proceedings of the 14'th international conference on low temperature physics, Otaniemi, Finland*, pages 285–288. North-Holland publishing Company, 1975. ISBN 0-7204-9303-X.

[71] R.P. Huebener. *Magnetic flux structures in superconductors*. Springer, 1978. ISBN 3-540-09213-7.

[72] E. M. Forgan. *Neutron scattering in layered copper-oxide superconductors*, volume 20 of *Physics and chemistry of materials with low-dimensional structures*, pages 375–403. Kluwer Academic Publishers, a. furrer edition, 1998. ISBN 0-7923-5226-2.

[73] M.R. Eskildsen *et. al.* Structural stability of the square flux line lattice in YNi_2B_2C and $LuNi_2B_2C$ studied with small angle neutron scattering. *Phys. Rev. Lett.*, 79(3):487–490, 1997.

[74] P.L. Gammel *et. al.* Effect of magnetic order on the superconducting length scales and critical fields in single crystal $ErNi_2B_2C$. *Phys. Rev. Lett.*, 82(8):1756–1759, 1999.

[75] M.L. Kulic L.N. Bulaevskii, A. I. Buzdin and S.V. Panjukov. Coexistence of superconductivity and magnetism. theoretical predictions and experimental results. *Adv. In Phys.*, 34:175–261, 1985.

[76] M.L. Kulic, A.I. Buzdin, and L.N. Bulaevskii. Magnetism and superconductivity in $(Re)Ni_2B_2C$: The case of $TmNi_2B_2C$. *Phys. Lett. A.*, 235:285–290, 1997.

[77] K. Yosida. *Theory of magnetism*. Springer, 1996. ISBN 3-540-60651-3.

[78] P.W. Anderson and H. Suhl. Spin alignment in the superconducting state. *Phys. Rev.*, 116(4):898–900, 1959.

[79] K. Nørgaard *et. al.* Interdependence of magnetism and superconductivity in the borocarbide $TmNi_2B_2C$. *Phys. Rev. Lett.*, 84(21):4982–4985, 2000.

[80] T. Hansen. Magnetic vortex cores in superconducting $TmNi_2B_2C$. Master thesis, Niels Bohr Institute for Physics, Astronomy and Geophysics, University of Copenhagen, 2001.

[81] Sting. If i ever lose my faith in you. *Ten summoner's Tales*, 1993.

Abstract (Max. 2000 char.)

The compound $TmNi_2B_2C$ has previously been studied by Small Angle Neutron Scattering(SANS) with the applied field along the crystalline c-axis and a very rich phase diagram in terms of flux line lattices(FLL) with different symmetries have been observed. One of the FLL transitions is coincident with a magnetic phase transition between two spin density waves.

In this thesis additional SANS studies of the FLL phases in $TmNi_2B_2C$ are reported and an interpretation of the phase diagram in the paramagnetic region is presented. It is suggested that the square FLL observed is stable in between two transition lines determined by two different length scales. The lower transition field is reached when the distance between the flux lines becomes comparable to the non-locality radius resulting from non-local electrodynamics, whereas the upper transition field is determined from the crossover from intermediate to high flux line density where the vortex cores start to overlap and the superconducting order parameter is suppressed in between the flux lines.

A detailed examination of the intensity of the neutron diffraction spots caused by scattering on the flux line lattice in $TmNi_2B_2C$ is presented and analyzed on the basis of the form factor of an isolated flux line. This analysis can not provide a good explanation for the observed scattering and it is suggested that the scattering from the Tm ions must be considered. One can argue that the moments of the Tm ions are modulated by the flux line lattice, because the Ruderman-Kittel-Kasuya-Yosida(RKKY) interaction between the Tm ions might be different inside the vortex cores than outside in the superconducting phase. A calculation of the neutron scattering cross section of such a magnetic flux line lattice has been performed and compared to the SANS data. This offers a qualitative explanation of some of the observations, but future work is needed to perform a more quantitative comparison.